

RECYCLED MATERIALS AS BACKFILL FOR MECHANICALLY STABILIZED EARTH WALLS

by

Ali Soleimanbeigi, Ph.D., P.E., Research Associate
University of Wisconsin-Madison
soleimanbeig@wisc.edu; (608) 444-3460

William J. Likos, Ph.D., Professor (Principal Investigator)
University of Wisconsin-Madison
likos@wisc.edu; (608) 890-2662

Burak F. Tanyu, Ph.D., Assistant Professor
George Mason University
btanyu@gmu.edu (703) 993-5621

Ahmet H. Aydilek, Ph.D., Professor
University of Maryland-College Park
aydilek@umd.edu; (301) 405-2692

Graduate Student

Paulo Florio, M.Sc. Candidate
University of Wisconsin-Madison

April 2016

Recycled Materials Resource Center
University of Wisconsin-Madison
Madison, WI 53706 USA

Table of Contents

PREFACE	1
1. RECYCLED MATERIALS	2
1.1. Common Types of Recycled Materials.....	2
1.1.1. Production Rates.....	3
1.1.2. Applications.....	4
1.1.3. Engineering Properties.....	4
1.1.4. Variability of Engineering Properties.....	7
1.2. Mechanically Stabilized Earth (MSE) Walls.....	8
1.2.1. MSE Wall Applications.....	9
1.2.2. MSE Wall Components.....	11
1.2.2.1. Selected Backfill.....	11
1.2.2.2. Reinforcements.....	12
1.2.2.3. Load Transfer Mechanism.....	14
1.2.2.4. Soil-Reinforcement Interface Properties.....	14
1.2.3. Design Specifications and Criteria.....	17
1.2.3.1 Stability Criteria.....	17
1.2.3.2. Geosynthetic Specifications.....	22
1.2.3.2. Selected Backfill Specifications.....	24
1.2.4. MSE Wall Design Procedure.....	26
1.2.4.1 Project Parameters.....	26
1.2.4.2. Wall Embedment and Reinforcement Length.....	26
1.2.4.3. Defining Nominal Loads, Load Combinations and Load Factors.....	27
1.2.4.4. Evaluating Sliding, Limiting Eccentricity, and Bearing Capacity.....	27
1.2.4.5. Evaluating Settlement.....	27
1.2.4.6. Selection of Reinforcement.....	28
1.2.4.7. Defining Critical Slip Surface.....	28
1.2.4.8. Defining Unfactored Loads.....	28
1.2.4.9. Vertical Layout of Reinforcements.....	28
1.2.4.10. Calculation of Factored Tensile Forces in the Reinforced Layers.....	28
1.2.4.11. Calculation of Soil Reinforcement Resistance.....	29
1.2.4.13. Selection of the Number of Soil Reinforcement Elements at Each Level.....	29

1.2.4.14. Internal Stability with Respect to Pull-out Failure	29
1.2.5. MSE Walls and Recycled Materials	30
1.2.5.1. Selection of Recycled Material for Backfill	30
1.2.5.2. Selection of Geosynthetic Reinforcements	32
2. BENEFICIAL USE FRAMEWORK	33
2.1. Beneficial Use of Recycled Materials as MSE Wall Backfill.....	33
2.2. Limitations of Recycled Materials as Backfill Aggregates.....	33
2.3. Geosynthetically Reinforced MSE Walls: Failure Modes and Case Histories	34
2.3.1. Failure Modes	34
2.3.2. Case Histories	35
2.3.2.1. Snailback Geotextile Shotcrete Wrapped Face Wall, Siskiyou National Forest, Oregon, 1974.....	35
2.3.2.2. Propped Panel Geogrid Wall, London, Ontario, 1989.....	36
2.3.2.3. Devils Punch Bowl Wrapped Face Geogrid Wall, Devils Punch Bowl State Park, Oregon, 1982.....	37
2.3.2.4. Tanque Verde Geogrid Concrete Panel Wall, Tucson, Arizona, 1984.....	38
2.3.2.5. Tower Oaks Residential MSE wall failure, Rockville, Maryland, 2003 (Mahmood 2009)	39
2.3.2.6. Segmental Block MSE Wall Failure, Southwestern Virginia, 2001 (Scarborough 2005)	40
2.3.2.7. Segmental Block MSE Wall Deformation, Eastern Tennessee, 2001 (Scarborough 2005)	42
3. MATERIALS AND METHODS	43
3.1. Recycled Aggregates and Geosynthetic Reinforcements.....	43
3.1.1. Index Properties.....	43
3.1.1.1. Recycled Concrete Aggregate.....	43
3.1.1.2. Recycled Asphalt Pavement	44
3.1.2. Geosynthetic Reinforcements.....	46
3.2. Laboratory Tests.....	50
3.2.1. Large-Scale Triaxial Tests.....	50
3.2.2. Large-Scale Interface Direct Shear Tests	51
3.2.3. Pull-out Tests.....	52
3.2.4. Temperature-Controlled Creep Tests	54
3.2.5. Long-Term Filtration and Associated Pore Size Evaluation Tests.....	57

4. RESULTS	60
4.1. Index Properties.....	60
4.1.1. Grain Size Distribution and Gradation Indices.....	60
4.1.2. Specific Gravity and Absorption	61
4.1.3. Compaction Characteristics	61
4.2. Large Scale Triaxial Test Results.....	63
4.2.1. RCA	63
4.2.2. RAP	65
4.3. Large Scale Interface Direct Shear Test Results	67
4.3.1. RCA	67
4.3.2. RAP	72
4.4. Pull-out Test Results	76
4.4.1. RCA	76
4.4.2. RAP	77
4.5. Creep Response of RAP.....	79
4.5.1. Triaxial Compression	79
4.5.2. Creep Response at Non-Elevated Temperature.....	83
4.5.3. Creep Response at Elevated Temperature	85
4.5.4. Coefficients of Thermal Creep	88
4.6. Drainage Performance of RCA/Geotextile Systems	89
4.6.1. Analyses of Clogging Behavior	90
4.6.2. Effect of Hydraulic Gradient on Clogging.....	95
4.6.3. Analyses of Retention Behavior.....	96
5. Conclusions and Recommendations	104
REFERENCES.....	106

List of Tables

Table 1.1. Index and Engineering Properties of Recycled Materials.....	6
Table 1.2. MSE wall applications, urban (after Elias et al. 2001)	10
Table 1.3. Values of soil friction angle, interface friction angle, friction efficiency and interaction coefficient reported in the literature.....	16
Table 1.4. Installation Damage Reduction Factors (after Berg et al. 2009).....	18
Table 1.5. Creep Reduction Factors (after Berg et al. 2009).	18
Table 1.6. Durability Reduction Factors (after Berg et al. 2009).....	18
Table 1.7. Resistance Factors for Tensile and Pull-out Resistance for MSE Walls (after Berg et al. 2009; AASHTO 2010).	19
Table 1.8. Values of Load Factors and Load Combinations (after WisDOT 2015).	21
Table 1.9. External Stability Resistance Factors for MSE Walls (after Berg et al. 2009; AASHTO 2010).	21
Table 1.10. Geotextile Strength Property Requirements AASHTO M288-06 (after Koerner 2005).	22
Table 1.11. Geogrid Property Recommendations for Reinforcement Applications (after Koerner 2009).	23
Table 1.12. MSE Wall Selected Granular Reinforced Fill Requirements (after Berg et al. 2009; AASHTO 2010).	24
Table 1.13. Recommended Soil Backfill Gradation for Geotextile and Geogrid Reinforcement Applications (Walls and Slopes) (After Koerner 2005).	25
Table 1.14. Electrochemical Property Criteria for Reinforced Fill in MSE Walls (WisDOT 2015).	25
Table 1.15. Minimum Wall Embedment Lengths (after Berg et al. 2009).	26
Table 1.16. Minimum Preliminary Length of Reinforcements (after Berg et al. 2009).	27
Table 1.17. Summary of MSE Wall backfill Specifications and Engineering Properties of Recycled Materials (after Berg et al. 2009; AASHTO 2010 and WisDOT 2015).	31
Table 2.1. Regulatory Limits for Cadmium, Chromium, Selenium and Silver as defined by Sections 538 and 140 of Wisconsin Administrative Code (after Edil et al. 2005a)	34
Table 3.1. Index Properties if RCA and RAP acquired in this study compared to values observed in the literature.	45
Table 3.2. Minimum Average Roll Values (MARV) for Several Index and Mechanical/Structural Properties of Selected Geosynthetics.	48
Table 3.3. Physical and Hydraulic Properties of the Geotextiles Used In This Study.	50
Table 3.4. Summary of Triaxial Compression and Deviatoric Creep Tests.	56
Table 4.1. Soil Classification and Gradation Indices for RCA and RAP.....	61
Table 4.2. Index Properties of RCA and RAP Compared to Values Observed in the Literature. 62	

Table 4.3. Friction Angles of Different Natural and Recycled Backfill Aggregates Reported in the Literature.....	67
Table 4.4. Interface Friction Angles and Efficiency Factors for Different Interface Materials...	70
Table 4.5. Interface Friction Angles, and Efficiency Factors between RAP and Selected Geosynthetic Reinforcements at Different Temperatures.....	74
Table 4.6. RCA Coefficient of Interaction from Pull-out Tests.....	77
Table 4.7. RAP Coefficients of Interaction from Pull-out Tests.....	78
Table 4.8. Coefficients of Interaction Between Several Soils and Geosynthetics Reported in the Literature.....	79
Table 4.9. Summary of Triaxial Compression and Deviatoric Creep Tests.....	80
Table 4.10. Stabilized permeability ratio and system hydraulic conductivity values of the RCA-geotextile systems at the end of each hydraulic gradient.....	90

List of Figures

Figure 1.1. Schematic view of a MSE wall cross-section (FHWA 2009).	8
Figure 1.2. Cost projection of retaining structures versus height (Koerner 2000).....	9
Figure 1.3. Geosynthetic reinforcement samples: (a) nonwoven geotextile, (b) woven geotextile, (c) biaxial geogrid, and (d) uniaxial geogrid.	13
Figure 1.4. Schematic view of soil-reinforcement interaction (FHWA 2009)	14
Figure 1.5. Schematic of internal stability failures in MSE walls (WisDOT 2015).....	17
Figure 1.6. Schematic of external stability failures in MSE walls (Berg et al. 2009).	20
Figure 2.1. Basic failure mechanism (after Koerner and Koerner 2012).....	35
Figure 2.2. Cross-section for the Snailback MSE wall in the Siskyou National Forest, Oregon (Allen et al. 2001).	36
Figure 2.3. Cross-section for the Geogrid reinforced MSE wall in London, Ontario (Allen et al. 2001).	37
Figure 2.4. Cross-section for the wrapped face geogrid MSE wall in Devils Punch Bowl State Park, Oregon (Allen et al. 2001).....	38
Figure 2.5. Cross-section for the precast concrete, geogrid reinforced MSE wall in Tucson, Arizona (Allen et al. 2001).	39
Figure 2.6. Scarps located at the top of the wall (Mahmood 2009).....	40
Figure 2.7. Visible bulging and separation between facing blocks (Mahmood 2009).	40
Figure 2.8. Cross section of the MSE in Southwestern Virginia (Scarborough 2005).	41
Figure 2.9. Failure of the MSE wall in Southwestern Virginia, shows the relative shallow failure surface just behind the wall facing (Scarborough 2005).	41
Figure 2.10. Cross section of the MSE in eastern Tennessee (Scarborough 2005).	42
Figure 3.1. RCA sample from Mandt Sandfill, Fitchburg, WI (a) and impurities found in RCA sample include broken glass, wood, chips and tile pieces (b).	44
Figure 3.2. RAP Sample from Payne and Dolan, Fitchburg, WI.....	45
Figure 3.3. (a) Uniaxial geogrid TensarUX-1500MSE, (b) Biaxial geogrid Tensar BX-4200, (c) Woven geotextile Thrace-LINQ GTF570, (d) Non-woven geotextile Thrace-LINQ 160EX.	47
Figure 3.4. (a) RCA sample enveloped by a rubber membrane during triaxial test setup. (b) Sample under confined pressure and vertical load during test.	51

Figure 3.5. Schematic figure of large scale interface direct shear apparatus (adapted from Goodhue et al. 2001).....	51
Figure 3.6. Schematic figures of the pull-out box apparatus. Top view (upper figure) and side view (lower figure) (adopted from Tatlisoz et al. 1998).....	54
Figure 3.7. Schematic of temperature-controlled triaxial creep system	55
Figure 3.8. Schematic setup of gradient ratio test chamber (modified after Fischer et al., 1999)	58
Figure 4.1. Grain size distribution of RCA and RAP	60
Figure 4.2. Compaction curve of RCA (a) and RAP (b).....	62
Figure 4.3. Stress-strain curves for RCA specimens from CD triaxial compression tests	63
Figure 4.4. RCA Mohr-Coulomb failure envelope	64
Figure 4.5. Failure plane for RCA specimens.....	64
Figure 4.6. RAP drained large-scale triaxial test curves at different confining pressures.....	65
Figure 4.7. RAP Mohr-Coulomb failure envelope.	66
Figure 4.8. Axial bulging deformation in RAP specimen.....	66
Figure 4.9. Interface direct shear results for RCA-Geosynthetic interaction, and respective Mohr-Coulomb failure criteria.....	68
Figure 4.10. Extensive tensional deformation of the nonwoven geotextile at the cross-section (left), and at the clamp connection (right).	71
Figure 4.11. Extension of the width (left), and height (right) of the nodes located at each aperture corners of the biaxial geogrid.	71
Figure 4.12. Interface direct shear test results for RAP-geosynthetic interaction and Mohr-Coulomb failure envelopes	73
Figure 4.13. Pull-out test results for RCA reinforced with woven geotextile (left), and uniaxial geogrid (right)	76
Figure 4.14. Pull-out test results for RAP reinforced with woven geotextile (left), and uniaxial geogrid (right)	78
Figure 4.15. Results of CD triaxial compression tests for compacted RAP at room temperature: (a) deviator stress versus axial strain and (b) volumetric strain versus axial strain.....	80
Figure 4.16. Evolution of volumetric strain with time through consolidation at different temperatures (T=35 °C-22 °C represents the compaction temperature of 35 °C and shearing temperature of 22 °C).....	81

Figure 4.17. Results of CD triaxial compression tests for RAP compacted and consolidated at different temperatures but sheared at 22 °C ($\sigma_3'=70$ kPa for these tests): (a) deviator stress versus axial strain and (b) volumetric strain versus axial strain	82
Figure 4.18. Creep test results for RAP at 22 °C and $\sigma_3'= 70$ kPa: (a) axial strain versus time (b) axial strain rate versus time (c) volumetric strain versus time and (d) stress level versus cube root of minimum strain rate.....	83
Figure 4.19. (a) Axial strain (b) axial strain rate, and (c) volumetric strain versus time for RAP compacted and consolidated at 22 °C and subjected to creep at different temperatures ($\sigma_3'= 70$ kPa).	85
Figure 4.20. (a) Axial strain (b) axial strain rate, and (c) volumetric strain versus time for RAP compacted and consolidated at different temperatures and subjected to creep tests at 22 °C ($\sigma_3'= 70$ kPa)	87
Figure 4.21. Variation of axial strain rate for compacted RAP with (a) creep temperature and (b) compaction temperature.....	88
Figure 4.22. The effect of (a) apparent opening size, and (b) geotextile permittivity on calculated permeability ratios.....	92
Figure 4.23. Temporal characteristics of (a) permeability ratio and (b) system permeability in RCA- nonwoven geotextile systems.....	93
Figure 4.24. Temporal characteristics of (a) permeability ratio and (b) system permeability in RCA- woven geotextile systems.....	94
Figure 4.25. The effect of hydraulic gradient on (a) permeability ratio, and (b) system hydraulic conductivity of geotextiles exposed to filtration with RCA	95
Figure 4.26. Changes in grain size distribution (GSD) of RCA exposed to filtration with nonwoven and woven geotextiles.	98
Figure 4.27. Changes in grain size distribution (GSD) of RCA exposed to filtration with woven geotextile.....	99
Figure 4.28. (a) Planar and (b) cross-sectional images of a virgin, and (c) planar and (d) cross-sectional images of post-gradient ratio test specimens of the nonwoven geotextile (Magnification = 2.5X for planar images and 5X for cross-sectional images).....	100
Figure 4.29. Images of woven geotextile: (a) virgin, and collected from (b) GRT2, and (c) GRT3.....	101

Figure 4.30. Changes in pore size distribution (PSD) of the nonwoven geotextile filtering RCA
..... 102

Figure 4.31. Changes in pore size distribution (PSD) of the woven geotextile filtering RCA.. 103

PREFACE

Granular materials are often the product of construction operations, industrial operations, or dredging operations in rivers, ports, and harbors. Traditional sources of reinforced granular backfill in Mechanically Stabilized Earth (MSE) wall construction (e.g., from crushed rock quarries and gravel pits) can be costly and environmentally not desirable. The use of recycled materials sourced from construction, industrial, or dredging operations could be a potentially more economical and environmentally beneficial source of backfill material than traditional sources. However, their suitability and limitations must be comprehensively assessed.

While there has been significant past research on the engineering properties of a wide range of recycled materials, such properties need to be investigated in the specific context of MSE wall performance. These notably include internal and interface frictional strength, hydraulic conductivity, geosynthetic pull-out resistance, durability, creep potential, corrosivity, and drainage performance.

Previous research, for example, has shown that recycled concrete aggregate (RCA) is an adequate reinforced backfill for MSE walls, although its potentially marginal hydraulic conductivity requires additional drainage to be provided. High pH and potentially high chloride or sulfate content often associated with RCA leachate can cause corrosion of aluminum or galvanized steel reinforcing members, particularly in the presence of high moisture contents resulting from poor drainage (Popova et al., 1998; FHWA, 2000). Another unresolved issue is the potential precipitation of tufa (CaCO_3), which can clog filter fabrics and further inhibit adequate backfill drainage (Rathje et al., 2006).

Recycled asphalt pavement (RAP) can also satisfy general criteria for use in MSE backfill applications (e.g., grain size distribution, shear strength), but displays significant potential for deviatoric creep and thermal sensitivity due to its asphalt content. These issues require more attention for use of RAP in long-term applications. Similarly, foundry sand/slag, bottom ash, and iron/steel slag can have suitable frictional and drainage properties. All of these materials, when compacted, can display adequate friction angle required for MSE reinforced backfill. However, secondary issues such as compatibility with geosynthetic reinforcement, drainage, creep potential, and interface frictional behavior require more consideration.

The overall goal of this project is to facilitate use of RAP and RCA in reinforced backfills for MSE retaining wall construction. This report consists of four chapters. In Chapter 1, the engineering properties of different types of recycled materials for potential use as backfill material are summarized from the literature. The design procedures for MSE walls, selection of backfill and geosynthetics, and current specifications are also summarized in Chapter 1. Chapter 2 summarizes issues related to responses of different types of recycled materials, as well as failure modes of MSE walls. The materials selected to conduct this research (including different types of geosynthetics and RAP and RCA samples) and testing procedures are described in Chapter 3. The experimental testing program includes index property tests, interface direct shear tests, pull-out tests, triaxial compression tests, creep tests, and hydraulic gradient ratio tests. Chapter 4 describes the test results and interpretation.

1. RECYCLED MATERIALS

1.1. Common Types of Recycled Materials

The use of recycled materials in engineering applications presents economic and environmental benefits. The disposal of these materials in landfills is costly and presents potential environmental issues for air and groundwater (Elias et al 2001; Rathje et al. 2006). Common recycled materials used in civil engineering applications include Recycled Concrete Aggregate (RCA), Recycled Asphalt Pavement (RAP), Bottom Ash (BA), Fly Ash (FA), Recycled Asphalt Shingles (RAS) and Foundry Sand (FDS). These materials have been used as base coarse for roadways, backfill for Mechanically Stabilized Earth (MSE) walls, aggregates for construction of highways and embankments, and the production of new asphalt and cement (FHWA 2004a; Anderson et al. 2009; Soleimanbeigi et al. 2015).

RCA particles have rough surfaces and angular shape, with a mix of natural aggregates and cement mortar (Anderson et al. 2009). The material is acquired from the reconstruction or demolition of pavements, airport runways, bridge structures and buildings (Rathje et al. 2006). The production of RCA is analogous to the production of natural aggregates (e.g. limestone, granite, etc.). It differs on the need to separate reinforcing steel and sealants which were added to the concrete for structural reinforcements, and materials that become mingled with the concrete waste during demolition (e.g. wood chips, plastics, tiles, and glass) (Kuo et al. 2002; Rathje et al. 2006). The final RCA product is then stored according to particle sizes. RCA can also be recycled in-situ using mobile plants and the material is usually reincorporated into the roadway (FHWA 2004a; Rathje et al. 2006).

RAP is a mixture of angular natural aggregates coated with bituminous material (i.e. asphalt binder) (Cosentino et al. 2001). The material is obtained from the recycling of asphalt concrete that is removed from roadways and parking lots during construction and resurfacing. RAP can be produced in-situ or through a recycling plant. RAP taken to recycling facilities is crushed and screened for impurities (e.g. glass, woodchips, metal, etc.) before being stacked for storage (Cosentino et al. 2001; ARRA 2001).

BA consists primarily of inorganic minerals, but also of organic matter that remains uncombusted in the process of combustion of coal. BA is characterized by an angular particle shape and porous surface (Seals et al. 1972), with grain sizes typically within the range of coarse sand with traces of gravel (Gautreau et al. 2009). BA is produced in coal burning plants, and is the heavier byproduct of coal combustion that accumulates onto the hot side walls of the furnaces. The clinkers eventually make their way through the ash hoppers below the furnaces and are collected as waste (Seals et al. 1972; Huang 1990; ACAA 2013).

FA is the finer portion of the ash that escapes the combustion chamber along with flue gases. FA is captured before exiting the chimney by emission control techniques (e.g. electrostatic precipitation, fabric filters and scrubbers) (ACAA 2015). FA is characterized as a non-plastic fine-grained material (Kumar et al. 2004; ACAA 2013) and its properties can vary with coal source. ASTM International (ASTM) classifies fly ash into two categories according to origin

and chemical composition. Class “F” fly ash is normally originated from burning Anthracite or bituminous coal, and presents pozzolanic properties. Class “C” fly ash originates from burning of lignite and sub-bituminous coal. In addition to pozzolanic properties, class “C” fly ash shows cementitious properties and will harden with contact with water (NAS 2006; Thomas 2007).

RAS is typically composed of asphalt cement (20-35%), cellulose felt (2-15%), mineral granule/aggregate (20-38%) and mineral filler/stabilizer (8-40%) (Townsend et al. 2010). RAS is obtained from re-roofing of existing structures and as rejected material from the production of roof asphalt shingles (Soleimanbeigi et al. 2015). Tear-off shingles require a more diligent recycling process than roofing shingle tabs. This is due the presence of nails, metal flashing, and felt underlayment resulting from the re-roofing process. The material is taken to a recycling plant, where it undergoes shedding and screening. Mixing with sand and water is necessary to avoid re-solidification and agglomeration of the material during stockpiling (FHWA 1997).

FDS is composed of well graded silica sand, bentonite clay or chemicals for binding, water and additives (e.g. coal dust, cereal, fuel oil or wood flour, etc.) (Javed et al. 1994; Goodhue et al. 2001; Soleimanbeigi et al. 2015). FDS is produced in foundry plants as a byproduct of metal casting. During a typical foundry process, sand from collapsed molds and cores is collected and reused into the foundry process. The recycled sand can be reused through many foundry cycles, but a portion of the material must be discarded when the storage capacity of the facility is reached (Abichou et al. 2004). The sand that exceeds the facility’s storage capacity may be landfilled or recycled as aggregate for engineering applications (FHWA 1997).

1.1.1. Production Rates

RAP and RCA are the most extensively recycled construction materials used in the United States to date (Edil et al. 2012). Over 140 million tons of RCA (EPA 2015) and 75.8 million tons of RAP (NAPA 2014) are produced per year. According to the National Asphalt Pavement Association (NAPA), 99.0% of RAP waste is recycled (NAPA 2014).

BA and FA are produced at rates of 14 and 53 million tons a year, respectively. From this total production, 39.0% of BA and 43.7% of FA are reused as construction materials or in other applications (ACAA 2014).

RAS has an annual production rate of 11 million tons in the United States (RMRC 2015; Soleimanbeigi et al. 2015). Ten million tons come from roof reconstruction (tear-offs) and another one million tons come from waste scrap produced during manufacturing (Sengoz et al. 2004; Warner et al. 2010). Approximately 85.0% of asphalt shingle waste is disposed in landfills, while 15.0% of the material is reused in the construction of new pavements (Soleimanbeigi et al. 2015).

FDS is a high volume waste and in most cases is non-hazardous. Foundries in the US produce approximately 15 million tons of foundry sand every year, out of which about 28% is reused. Reuse is primarily in construction-related applications, while the remaining sand is landfilled (AFS 2015).

1.1.2. Applications

Waste materials not landfilled are used in diverse engineering applications. RCA is used as aggregate in Portland cement concrete production (FHWA 2004a), aggregate base course in roadways, pipe bedding (CDRA 2015), riprap revetments (ODNR 2015), and backfill aggregate for retaining structures (Rathje et al. 2006).

RAP is mostly used in the production of new asphalt concrete, or as base course/subbase aggregate in roadway construction, accounting for the use of nearly 98.0% of all RAP production (NAPA 2015). These applications, widely used in highway construction, include the production of asphalt cement supplement, hot-mix asphalt (HMA), cold mix asphalt (CMA) (FHWA 1997; ARRA 2001), base aggregates, embankments and fills (Rathje et al. 2006; Edil et al. 2012).

BA has been successfully used as backfill for MSE walls and as embankment fills (Gautreau et al. 2009). The material is employed as fine aggregate substitute in the production of HMA, base course, granular base and sub-base for highway construction (FHWA 1997). Additional use of BA is as a constituent of cement manufacturing (ACAA 2015).

FA is widely used in the manufacturing of concrete products for use in roads, bridges, buildings, concrete blocks, and similar applications. FA can also be used as fill and embankment material. In landfill applications, FA is used to stabilize and solidify waste materials (Gutt et al. 1979; ACAA 2015). Other applications of FA include flowable fills, soil and road base stabilization, structural fill and asphalt filler (FHWA 2004b).

RAS has been used as aggregate for road base and as a substitute for natural binder in the production of HMA (Warner et al. 2010). It is also used in the production of new roof shingles, cold patch, temporary roadways and driveways, and as fuel oil (CDRA 2015).

FDS beneficial uses include flowable fills, highway embankments, aggregate sub-base under flexible pavements (Partridge et al. 1999; Abichou et al. 2004) and backfill for MSE walls (Goodhue et al. 2001). Another application of FDS is as material substitution on the production of HMA and concrete (Abichou et al. 2004; CWC 2015).

1.1.3. Engineering Properties

The typical range for physical and mechanical properties of the recycled materials are summarized in Table 1.1. Parameters reported include grain size indices, material composition, absorption, specific gravity, dry unit weight, water content, angle of internal friction, cohesion, and hydraulic conductivity. The physical and mechanical properties of recycled materials may be affected by the chemical composition of parent materials and recycling process (Kuo et al. 2002).

RCA differs from natural aggregates in composition (e.g. presence of mortar). It is more angular and has rougher surface than its virgin aggregate counterparts (Griffiths et al. 2002, Juan et al. 2009; Rathje et al. 2006; Soleimanbeigi et al. 2015). These physical characteristics are believed to augment the friction angle of RCA (Tatsuoka et al. 2005; Rathje et al. 2006). RCA is susceptible to higher-than-normal particle breakdown which can potentially increase the amount

of fines (e.g. particles passing No. 200 sieve), thus reducing hydraulic conductivity and altering the material's compaction characteristics (Rathje et al 2006).

RAP consists of nearly 92-97% aggregates that are coated with asphalt binder (Rathje et al. 2001). The specific gravity of asphalt binder is 1.0-1.04 (Roberts et al. 1996). The low specific gravity of asphalt binder thus lowers bulk values of specific gravity and dry unit weight of RAP. RAP particles have low absorption potential and a low content of fine particles. Because the material consists of angular particles, values of internal friction angles observed in the literature are equivalent to or higher than those of natural aggregates (Rathje et al. 2006; Cosentino et al. 2006; Soleimanbeigi et al. 2012; Edil et al. 2012). A critical characteristic of RAP is its creep potential. The viscoelastic properties of the bituminous coating in RAP may cause excessive creep strains when RAP is subjected to sustained deviatoric stresses (Rathje et al. 2006; Soleimanbeigi et al. 2015).

BA's physical and engineering properties depend on the parent coal type, specific plant processing, and recycling methodology. Gradation varies broadly between samples, and generally varies from well-graded gravel to poorly-graded sand. The presence of iron increases the values of specific gravity of BA. Specific gravity values reported in the literature range from 1.3 to 3.2 (Huang 1990). BA presents angles of internal friction comparable to that of well-graded angular sands (Gautreau et al. 2009) and hydraulic conductivities comparable to compacted sand (Kim et al. 2015).

FA is a lightweight, non-plastic material and is typically classified as well graded silt. Angles of internal friction reported in the literature fall within 29°- 40°, which is within the general range of broader types of granular materials. The specific gravity of FA is directly related to iron content (e.g. iron increase specific gravities values) (Martin et al. 1990; Kumar et al. 2014).

RAS composition varies according to parent product types and recycling methods. Depending on the recycling procedure, RAS particles can be spherical or plate-like shaped. RAS is non-plastic in nature and exhibits low dry unit weights, typically varying from 9.0 to 13.8 kN/m³ (Sengoz et al. 2004; Warner et al. 2010). The compressibility of RAS is higher than natural soil, thus often requiring stabilizing additives such as fly ash. As with other materials having asphalt as constituents, RAS is subject to creep deformation. This phenomenon is increased at higher temperatures (Soleimanbeigi 2012).

FDS is composed of subangular to round sand particles, uniformly graded, with 0.0-12.0% bentonite (Goodhue et al. 2001; FHWA 2004c). The amount of fines (e.g. bentonite) controls plasticity of FDS. Liquid limits higher than 20.0% are common for FDS with bentonite contents between 6.0-10.0%. Other typical properties, such as gradation and specific gravity are comparable to natural sand, with angles of internal friction slightly higher. The permeability of FDS is influenced by the bentonite content, ranging from 5×10^{-3} - 1×10^{-7} cm/s (Abichou et al. 2000; Goodhue et al. 2001; FHWA 2004).

Table1.1. Index and Engineering Properties of Recycled Materials.

	RCA	RAP	BA	FA	RAS	FDS
USCS	GW, GP, SW, SP, SC	GW, SW, SP	GW, SW, SP, SM	ML	SW - SP	SP, SM, SC
AASHTO	A-1-a, A-1-b	A-1-a, A-1-b	A-1-a, A-1-b, A-2-4	-	-	A -2-4, A-3, A-2
Fine Content (%)	3.2 - 12.8	0.6 - 3.0	0.0 – 12.0	100	3.8	1.0 - 13.0
Mortar/Asphalt/Clay (%)	37.0 – 65.0	3.5 - 7.1	-	-	20.0 – 35.0	2.3 - 15.0
Absorption (%)	5.0 - 6.5	0.6 - 2.0	0.6 - 0.8	-	-	-
G_s	2.24 - 2.72	2.20 - 2.56	1.30 - 3.20	2.10 - 2.81	1.74 - 2.70	2.51 - 2.80
γ_{d, max} (kN/m³) (SP)	17.5 - 19.2	13.9 - 19.4	9.9 - 17.6	13.4 - 19.6	8.8 - 13.8	16.5 - 18.4
ω_{opt} (%)	8.7 - 11.9	5.2 - 8.8	1.6 - 2.8	16.0 - 18.6	8.0 - 9.8	9.6 – 16.4
φ' (degrees)	41 - 63	39 - 44	32 - 45	29 - 40	36	35 - 43
c' (kPa)	0 - 55.2	2.3 - 55	0 - 20.1	20.1	7.0 - 24.0	6.0 – 15.0
k (cm/s)	7.1x10 ⁻⁴ - 1.8x10 ⁻³	1.1x10 ⁻⁴ - 1.6x10 ⁻³	1.0x10 ⁻² – 1.0x10 ⁻⁴	5.6x10 ⁻⁴ 6.0x10 ⁻⁵	- 2.0x10 ⁻⁴	5.2x10 ⁻³ 4.8 x 10 ⁻⁸

Note: USCS = United Soil Classification System, AASHTO = American Association of State Highway and Transportation Officials (soil classification system). Mortar content for RCA, asphalt content for RAP and RAS, and clay for FDS . G_s = specific gravity; γ_{d,max}= maximum dry unit weight; ω_{opt}=optimum water content; φ'=effective friction angle; c'=effective cohesion and k=hydraulic conductivity; SP=Standard Proctor

1.1.4. Variability of Engineering Properties

In this section the variability of index and mechanical properties of recycled materials observed in the literature and presented in Table 1.1 is discussed.

Variations in gradation and dry unit weight in RCA samples is believed to be the result of mortar content. Mortar content between RCA samples may vary as a result of differences in recycling processes (e.g. increasing numbers of crushing sections can reduce mortar amounts). Because mortar has a lower specific gravity (2.10), samples of RCA with higher mortar contents will present lower specific gravity and lower dry unit weight than samples of RCA with lower mortar contents. (Juan et al. 2009; Edil et al. 2012, RMRC 2014).

The reported engineering properties of RAP are similar among samples. Because only 3.0 to 7.0% of RAP consists of asphalt binder, differences in properties between RAP samples are likely to be the result of differences in the virgin aggregates used for construction of pavements (Rathje et al. 2001). However, different asphalt contents between samples of RAP may explain the variability observed in specific gravity values (2.20 to 2.56).

BA samples show a wide variation for mineral constituents. Samples with higher iron content exhibit higher values of specific gravity (Seals 1972). Variations in grain size distribution are common between plants, and even between samples from the same plant (RMRC 2015). Differences in friction values of BA (32°-45°) were observed. Friction angles of BA depend on the angularity of BA particles, which can vary with different recycling processes (Soleimanbeigi et al. 2012).

FA samples show similar grain size distribution, but variable specific gravity values due to differences in iron content. Values of dry unit weight are affected by specific gravity, and also show some variation amongst the samples (Martin et al. 1990; Kumar et al. 2014).

RAS is manufactured from shingles that present different compositions. In addition, different procedures of recycling affect grain size distribution (Warner et al. 2010). Significant variation was also observed in specific gravity which may be the result of asphalt content variability (Soleimanbeigi 2012).

FDS includes clay or chemically bonded sand. Sands from the same foundry are not likely to show much variability. However, samples from different foundries can present differences in chemical composition. The main difference in FDS by literature review was observed in the range of clay content reported, from 5.0 to 15.0% (FHWA 2004c; Benson et al. 2000). These variations in clay contents directly influence corresponding values of hydraulic conductivity and cohesion (Abichou et al. 2000; Goodhue et al. 2001).

1.2. Mechanically Stabilized Earth (MSE) Walls

Mechanically Stabilized Earth (MSE) walls are retaining walls with face angles from 70° to 90° . MSE walls are internally stabilized and comprise three main components: facing, internal reinforcement (e.g. geosynthetics or metallic components) and selected backfill (Yohchia 1997; Rathje et al. 2006; Das 2008). Coarse, free-draining material is generally chosen for backfill in order to ensure high drainage capacity as well as structural integrity of the wall (Berg et al. 2009). The interaction between reinforcement and backfill allows MSE walls to sustain significant loading and deformation, and to behave like a flexible unit (Rathje et al. 2006; Berg et al 2009). A general schematic model of an MSE wall is shown in Figure 1.1.

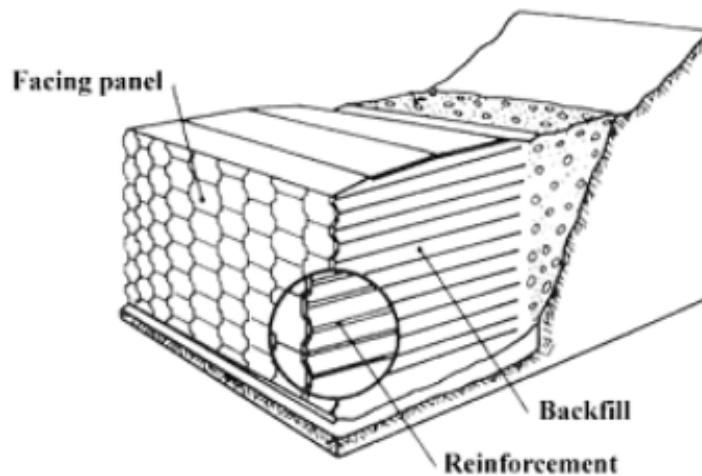


Figure 1.1. Schematic view of a MSE wall cross-section (FHWA 2009).

MSE walls offer economic and technical advantages over conventional types of retaining walls (e.g. Gravity, Semi-Gravity, Cantilever and Counterfort), including less site preparation requirements, reduction of right-of-way acquisition and stability for wall-heights over 30 m. Geosynthetic reinforced MSE walls are the least expensive choice for most wall heights (Koerner et al. 2000).

MSE walls eliminate the need for deep foundations and are flexible and are thus capable to tolerate deformations due to poor subsoil conditions. In addition, MSE walls are more resistant to seismic loading and can tolerate much larger settlements than conventional retaining walls (Koerner 2000; Elias et al. 2001; Basudhar et al. 2008; Berg et al. 2009;). Figure 1.2 shows the relationship between costs vs. height for retaining walls of different types.

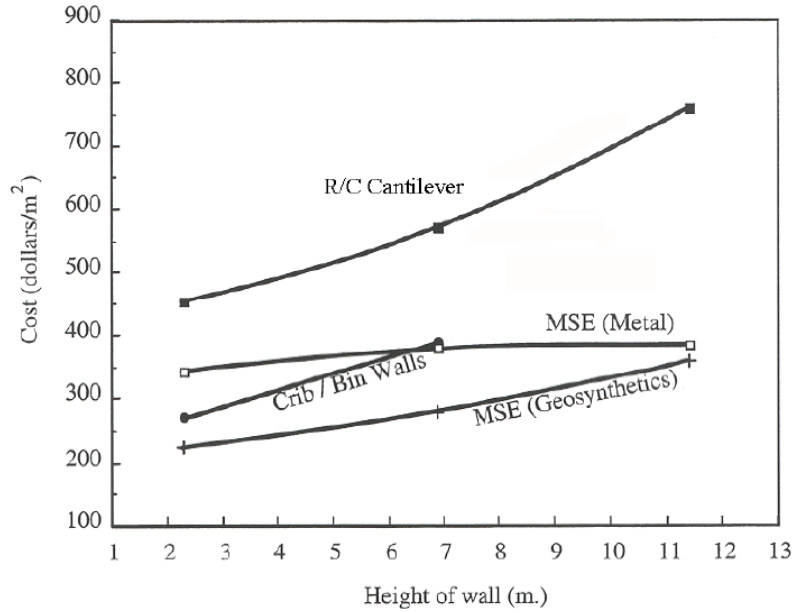


Figure 1.2. Cost projection of retaining structures versus height (Koerner 2000).

1.2.1. MSE Wall Applications

MSE walls have been the choice of retaining structures in many applications including bridge abutments, embankments and excavations where the lack of space limits the construction of stable side slopes. MSE walls are also widely used as temporary walls for detours during highway reconstruction projects, the construction of containment dikes and dams – including increasing heights of existing dams – and seawalls. The figures in Tables 1.2 and 1.3 illustrate some additional representative uses of MSE walls.

Table 1.2. MSE wall applications, urban (after Elias et al. 2001), continued

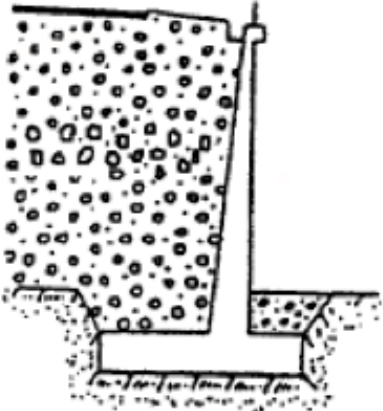

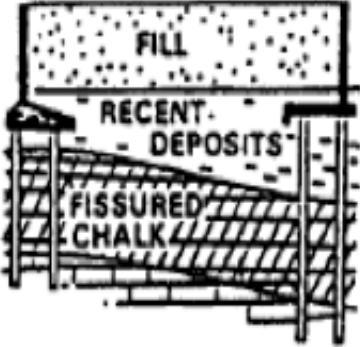
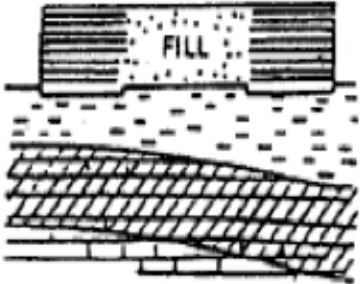
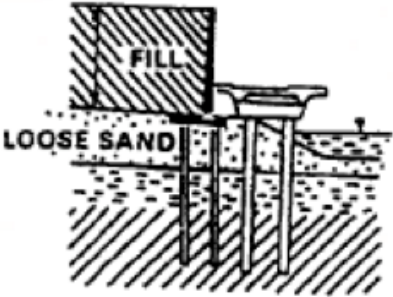
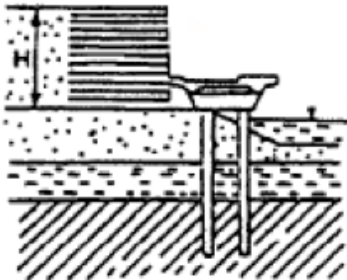
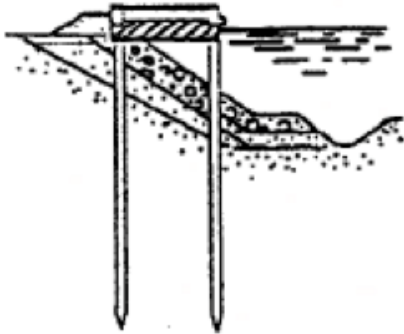
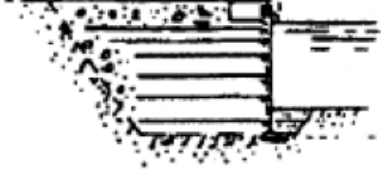
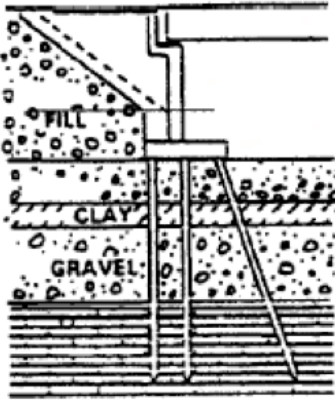
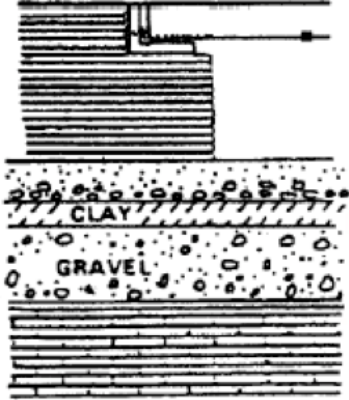
	Standard Solution	MSE wall
Retaining Wall		
Bridge Approach Fill over Compressible Foundation		
Interchange Access Ramps with		

Table 1.2. Continued, MSE wall applications, abutments and marine (after Elias et al. 2001).

	Standard Solution	MSE wall
Marine Wall		
Bridge Abutment		

1.2.2. MSE Wall Components

The most critical components of a MSE wall are the selected backfill and reinforcements. The facing component is important for aesthetical purposes, but contributes little to the overall stability of the MSE wall system. The components of the MSE walls are discussed below:

1.2.2.1. Selected Backfill

Backfill materials can be natural or recycled materials that meet design criteria established by regulatory agencies (e.g. AASHTO, FHWA, state DOTs, etc.). The backfill used in MSE walls consists of coarse-grained material with low fines content (less than 15%) (AASHTO 2010; Anderson et al. 2012).

The selection of backfill material considers the long-term performance of the wall system. The material shall offer good drainage, and thus the hydraulic conductivity of a selected material must be high enough to allow water to percolate freely through the backfill. Excessive amounts of fines can reduce the hydraulic conductivity of a given coarse material, thus contributing to long-term performance issues of the wall (Elias et al. 2001; Rathje et al 2006). Based on the AASHTO T-27 criteria discussed by Berg et al. (2009), to obtain reasonable drainage, the fines content of the selected

material for reinforced fill shall have no more than 15% fines (as determined from passing No. 200 sieve) and 60% fine sand size particles (as determined from particles passing No. 40 sieve). The plasticity index of the material shall be less than 6.

The potential corrosion of metal reinforcements can be enhanced if water is retained by poorly draining backfill. For this reason, the use of material with high water absorption potential such as clay and silt is not recommended as backfill (Elias et al. 2001; Berg et al. 2009). Corrosion is a major concern when the MSE wall system utilizes metal reinforcements because it can result in sudden failure of the wall system (FHWA 2009; Anderson et al. 2012).

The mechanical stability of the wall depends, in part, on the mechanical properties of the backfill. The material should yield adequate angle of internal friction allowing high shear strength against horizontal pressures imposed by the soil mass (Elias et al. 2001; Rathje et al. 2006; Berg et al. 2009). The selected backfill should also develop sufficient interface friction with the reinforcement. Well-graded and less angular materials yield higher values of dry unit weight during compaction (FHWA 2009). Materials compacted at low dry unit weight and low water content can experience significant settlement upon wetting (Basma et al. 1992; Rathje et al. 2006; Berg et al. 2009).

An additional deformation mechanism of concern in MSE walls is creep if the backfill is a material with high creep potential such as RAP or RAS (Soleimanbeigi et al. 2014, 2015). This behavior will be more enhanced at higher temperatures. The use of materials susceptible to creep is usually not recommended for backfill because they affect the long-term stability of the wall, leading to excess deformation of the MSE wall system (Rathje et al. 2006).

1.2.2.2. Reinforcements

The function of reinforcements is to provide shear strength to the backfill against the lateral earth pressure. Reinforcements used in MSE walls can be classified as extensible and inextensible (Koerner 2005; Das 2008). Inextensible reinforcements show deformation at failure much less than the deformability of the soil. Steel strips and bar mats are examples of inextensible reinforcement. Extensible reinforcements, on the other hand, show deformation at failure equal to, or greater than the deformability of the soil. Geotextiles, geogrids and woven steel wire mesh are extensible reinforcements (Koerner 2005; Das 2008; Berg et al. 2009).

The terms machine direction (MD) and cross-machine direction (CD – sometimes referred to as XMD) are commonly found in literature and specifications from manufacturers. In general, geotextiles are stronger in the machine direction. The difference between MD and XMD could be as large as 50% (Koerner 2005).

Geotextiles are made from geosynthetic fibers, fashioned into a flexible, porous fabric. Geotextiles can be made into woven and nonwoven patterns (Koerner 1994). The weaving process makes two sets of parallel filaments into a planar surface by systematically interlacing them to produce woven geotextiles. Nonwoven geotextiles, on the other hand, are produced by matting geosynthetic fibers together in a random or organized manner. After the placement of the fibers, these filaments are chemically, thermally or mechanically bonded (Holtz et al. 1998; Koerner et al. 2005; Das 2007). In MSE wall applications, woven geotextiles are typically used for reinforcements as they have much

higher tensile strength. Nonwoven geotextiles are typically used to provide drainage along the facing and behind and underneath reinforced zones (Berg et al., 2009).

Geogrids are made with polypropylene (PP) or polyethylene (PET) (high-modulus plastic materials) into wide, grid-like shape. The apertures (e.g. opening between the longitudinal and transverse ribs) of geogrids are large enough to allow passage of soil from one side to another. Manufacturing of geogrids can be done with different process: extruded, woven and welded (Das, 2007; Koerner 2005; Holtz et al. 1998). Geogrids can be further engineered in uniaxial or biaxial strength directions. The Terms MD and XMD apply to geogrids in much the same way as they do for geotextiles (Koerner 2005). Geogrids are usually stiff and the apertures allow interlocking with surrounding backfill material (Das 2007). Samples of different types of geosynthetics are shown in Figure 1.3.

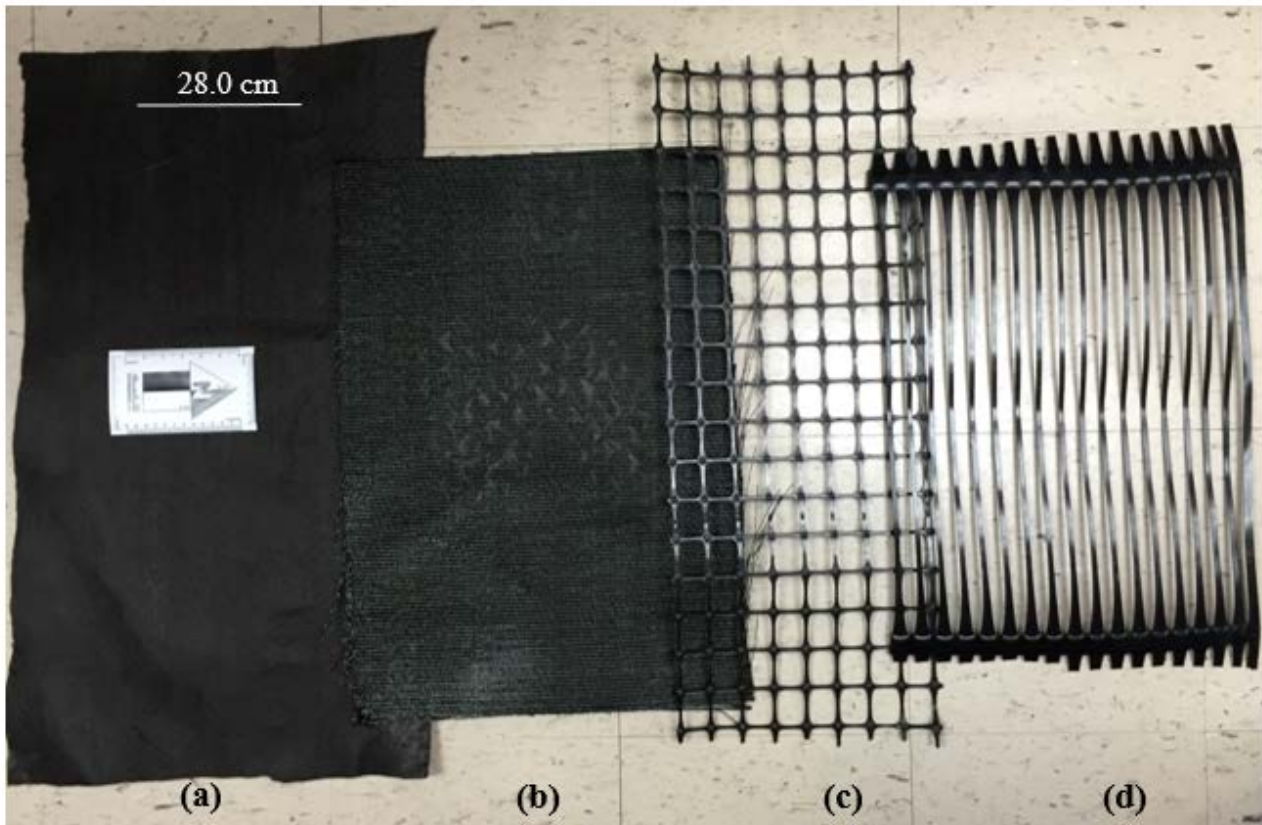


Figure 1.3. Geosynthetic reinforcement samples: (a) nonwoven geotextile, (b) woven geotextile, (c) biaxial geogrid, and (d) uniaxial geogrid.

Metallic reinforcements are generally made of steel and are susceptible to corrosion. Corrosion protection is achieved by galvanization but epoxy coating is also common. Main types of metal reinforcements used in MSE wall applications are flat ribbed strips (Elias et al. 2009) and welded wire metal mats (Bilgin et al. 2014).

The type of reinforcement to be used in a given backfill depends on specific MSE wall applications, environmental conditions, expected loads, and the properties of the backfill material. Criteria regarding the general design are governed by codes that consider resistance according to various

failure modes (Berg et al. 2009; Anderson et al. 2012; Elias et al. 2001). The efficiency of reinforcements depends on reinforcement length, reinforcement-to-panel-connection, as well as friction between the soil and the reinforcement face or ribs. Other factors, such as compaction and the facing system, affect the efficacy of a given reinforcement against horizontal movement. The type of reinforcement must be further analyzed based on its intrinsic properties such as creep potential, corrosion potential, ultra violet (UV) resistance and biodegradation susceptibility. These properties are material dependent. The selected backfill material will also affect some of these intrinsic properties such as corrosion and biodegradation (Berg et al. 2009).

1.2.2.3. Load Transfer Mechanisms

When vertical stress is applied to a soil mass, the soil particles respond by transferring the stress through surrounding particles, creating additional horizontal stress. The use of reinforcements is necessary to resist this additional horizontal stress. Stress is transferred from the soil to reinforcements via passive resistance and frictional resistance. Friction between soil particles and the reinforcement acts in the direction counter to soil movement. Passive resistance is developed through normal pressure acting on the face of the reinforcement. Passive resistance is a bearing-type stress that compresses the soil against the surface of the reinforcement, causing an increase in friction transverse to the direction of movement (Elias et al. 2001; Berg et al. 2009). Figure 1.4 shows a schematic of the interaction between backfill and reinforcement.

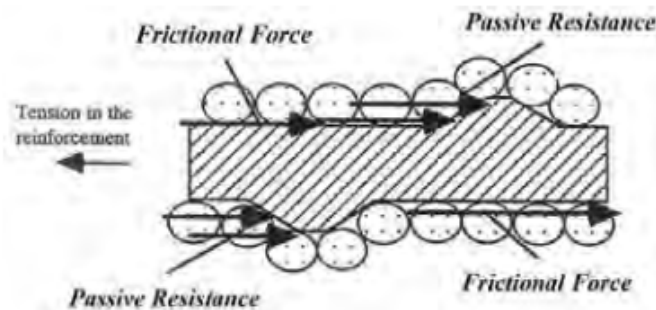


Figure 1.4. Schematic view of soil-reinforcement interaction (FHWA 2009)

1.2.2.4. Soil-Reinforcement Interface Properties

Soil-reinforcement interactions depend on the nature and mechanical characteristics of both the soil and the reinforcement. While surface frictional mechanisms may dominate soil-geotextile interaction, interlocking friction dominates interaction between soils and geogrids.

Interface direct shear tests and pull-out tests are used to acquire soil-reinforcement interface properties. These tests are performed under plane-strain conditions to better represent the soil-reinforcement interactions within an MSE wall system.

The soil-reinforcement interface friction angle (δ) is obtained from interface direct shear tests. During the test the soil is sheared past the static reinforcement under different normal pressures. A linear

Mohr-Coulomb failure criterion is constructed, and the interface shear angle is calculated. Interface direct shear test results can be interpreted in terms of friction efficiency (E_ϕ), which is the ratio of interface friction angle and the internal friction angle of the soil:

$$E_\phi = \tan \delta / \tan \phi \quad (1.1)$$

where,

δ = interface friction angle

ϕ = internal soil friction angle

Values of E_ϕ are used as a measurement of shear interaction efficiency between the soil and geosynthetic, and only account for the friction interaction between them. E_ϕ is usually less than one for geotextiles, and larger than one for geogrids. This suggests that interlocking and passive pressure on transversal ribs also contribute to shear resistance in geogrids.

In pull-out tests, a geosynthetic embedded in backfill material is pulled at a constant rate. The interaction coefficient (C_i), can be calculated from pull-out test results using Equation 1.2:

$$C_i = P / (2 \cdot W \cdot L \cdot \sigma_n \cdot \tan \phi) \quad (1.2)$$

where,

P = maximum pull-out force

W = width of the reinforcement

L = length of the reinforcement

σ_n = normal pressure

C_i = interaction coefficient

ϕ = internal soil friction angle

In design, the C_i value is used to calculate the required anchorage length (L) of the reinforcement within the MSE wall backfill. Table 1.3 summarizes representative values of friction angle for common backfill soils and soil-reinforcement interaction values reported in the literature.

Table 1.3. Values of soil friction angle, interface friction angle, friction efficiency and interaction coefficient reported in the literature.

Soil Type	Reinforcement type	Soil internal friction angle (ϕ)	Interface friction angle (δ)	E_{ϕ}	C_i	References
Sand	Woven geotextile (PP)	37.5	35.3	0.92	0.92	Hsieh et al. (2011)
	Geogrid (PET)	37.5	37.0	0.98	0.93	
	Uniaxial geogrid	34.6	33.8	0.97	0.43	
Gravel	Woven geotextile (PP)	38.4	26.9	0.64	0.42	Hsieh et al. (2011)
	Geogrid (PET)	38.4	38.6	1.01	0.88	
	Geogrid uniaxial	45.8	44.4	0.95	0.71	
Crushed stone	Woven geotextile (PP)	55.0	30.6	0.41	0.36	Hsieh et al. (2011)
	Geogrid (PET)	55.0	43.3	0.66	0.58	
RCA	Biaxial geogrid (PP)	65.0	50.0	0.55	-	Arulrajah et al. (2013)
RAP	Biaxial geogrid (PP)	45.0	40.5	0.71	-	Arulrajah et al. (2013)
FDS	Woven geotextile (PP)	43.0	29.0	0.60	0.32	Goodhue et al. (2001)
	Woven geotextile (PP)	31.0	29.0	0.90	0.26	
	Uniaxial geogrid (PET)	44.0	31.0	0.60	-	
	Uniaxial geogrid (PET)	31.0	26.0	0.80	0.44	

1.2.3. Design Specifications and Criteria

1.2.3.1 Stability Criteria

MSE walls must be evaluated for both internal and external stability. Internal stability of MSE walls results from the interaction between the backfill and reinforcements. Failure of the reinforcement may occur through breakage, excessive deformation (e.g. tension failure), or when the reinforcements slide excessively (e.g. pull-out failure) (Figure 1.5). Designs for internal stability of MSE walls are achieved through several different methods. Commonly used methods are Coherent Gravity, Tieback Wedge, FHWA Structure Stiffness and Simplified Method (Allen et al. 2001).

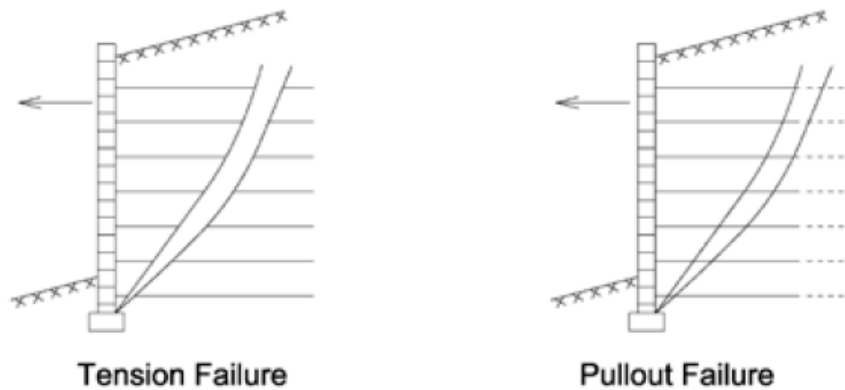


Figure 1.5. Schematic of internal stability failures in MSE walls (WisDOT 2015).

Internal stability considers pull-out resistance between the soil and reinforcement, tensile strength and durability of the reinforcement. The maximum factored load is determined for each reinforcement, and compared to the factored pull-out and tensile resistance of the reinforcement for strength, service, and extreme event limit states (FHWA 2009). The nominal tensile strength of geosynthetic reinforcement (T_{al}) is selected after consideration of several factors that may induce strength losses over the life time of the design. Some factors commonly considered include creep, installation damage, aging and temperature. Because of the wide variation in geosynthetic properties, T_{al} may be determined for each product as follows:

$$T_{al} = T_{ult} / RF \quad (1.3)$$

where,

T_{ult} = ultimate tensile strength (strength per unit width), which is based on the minimum average roll value (MARV) given by the manufacturer.

RF = reduction factor, which is the product of all applicable reduction factors (e.g. RF_{ID} = installation damage factor, RF_{CR} = creep reduction factor, RF_D = durability reduction factor).

Recommended values for RF_{ID} , RF_{CR} , and RF_D are shown in Tables 1.4, 1.5 and 1.6 respectively.

Table 1.4. Installation Damage Reduction Factors (after Berg et al. 2009).

Reduction Factor, RF_{ID}		
Geosynthetic	Backfill	
	Max. size 100 mm , D_{50} about 30 mm	Max. size 20 mm , D_{50} about 0.7 mm
HDPE uniaxial geogrid	1.20 - 1.45	1.10 - 1.20
PP biaxial geogrid	1.20 - 1.45	1.10 - 1.21
Woven geotextiles (PP & PET)	1.40 - 2.20	1.10 - 1.40
Slit film woven geotextile	1.60 - 3.00	1.10 - 2.00
Nonwoven geotextiles (PP & PET)	1.40 - 2.50	1.10 - 1.40

Table 1.5. Creep Reduction Factors (after Berg et al. 2009).

Reduction Factor, RF_{CR}	
Polymer Type	RF_{ID}
Polyester (PET)	1.6 - 2.5
Polypropylene (PP)	4.0 - 5.0
High Density Polyethylene (HDPE)	2.6 - 5.0

Table 1.6. Durability Reduction Factors (after Berg et al. 2009).

Reduction Factor, RF_D^*		
Geosynthetic^a	RF_D	
	$5 \leq pH \leq 8$	$3^b < pH \leq 5$ $8 \leq pH < 9$
Geotextiles (PET), ($M_n < 25,000$), ($40 < CEG < 50$)	1.6	2.0
Coated geogrids (PET), Geotextiles (PET) ($M_n > 25,000$), ($CEG < 30$)	1.15	1.3
All other geosynthetic types ^c	1.3 – 1.7	1.3 – 1.7

M_n = number average molecular weight
CEG = carboxyl end group

Notes:

- Use of materials outside the indicated molecular property range requires specific product testing. Use of products outside of $3 < pH < 9$ range is not recommended.
- Lower limit of pH for permanent applications is 4.5 and lower limit for temporary applications is 3, per Article 11.10.6.4.2b (AASHTO, 2007).
- A default $RF_D = 1.3$ may be used if the product specific installation damage testing is performed, and it is determined that $RF_{ID} = 1.7$ or less, and if the other requirements in Table 3.12 of the “FHWA Design Manual for MSE Walls” are met

Resistance factors for different types of reinforcements are recommended by AASHTO. Table 1.7 presents resistance factor values for different reinforcement types and loading conditions (Berg et al. 2009; AASHTO 2010).

Table 1.7. Resistance Factors for Tensile and Pull-out Resistance for MSE Walls (after Berg et al. 2009; AASHTO 2010).

Reinforcement Type and Loading Condition		Resistance Factor
Geosynthetic Reinforcements and connectors	Static loading	0.90
	Combined static/earthquake loading	1.20
	Combined static/traffic barrier impact	1.20
Pull-out Resistance of geosynthetic	Static loading	0.90
	Combined static/earthquake loading	1.20
	Combined static/traffic barrier impact	1.00

The resistance factor due to loading accounts for potential overstress caused by differential pressure on the geosynthetic and for uncertainties that may affect the strength of the geosynthetic over the life time of the wall. For static loading, a resistance factor of 0.9 is recommended, due to the ductile nature of polymeric materials. This recommendation is justified because the soil controls the amount of strain in the geosynthetic, which is significantly less than its corresponding rupture strain. Even at the limit state, excessive strain in the geosynthetic would allow a time-dependent deformation of the wall, rather than sudden collapse. Moreover, the mechanical properties of geosynthetics are significantly improved when confined in soil (Berg et al. 2009).

External stability assumes that the wall behaves as a coherent block. Therefore, the geometry of the entire wall is taken into consideration (Caltrans 2004; WisDOT 2015). The wall must be designed to resist overturning (limiting eccentricity), sliding and bearing capacity failures. These are illustrated in Figure 1.6 (Das 2007; Berg et al. 2009). Loads of permanent and transient natures are considered in these calculations.

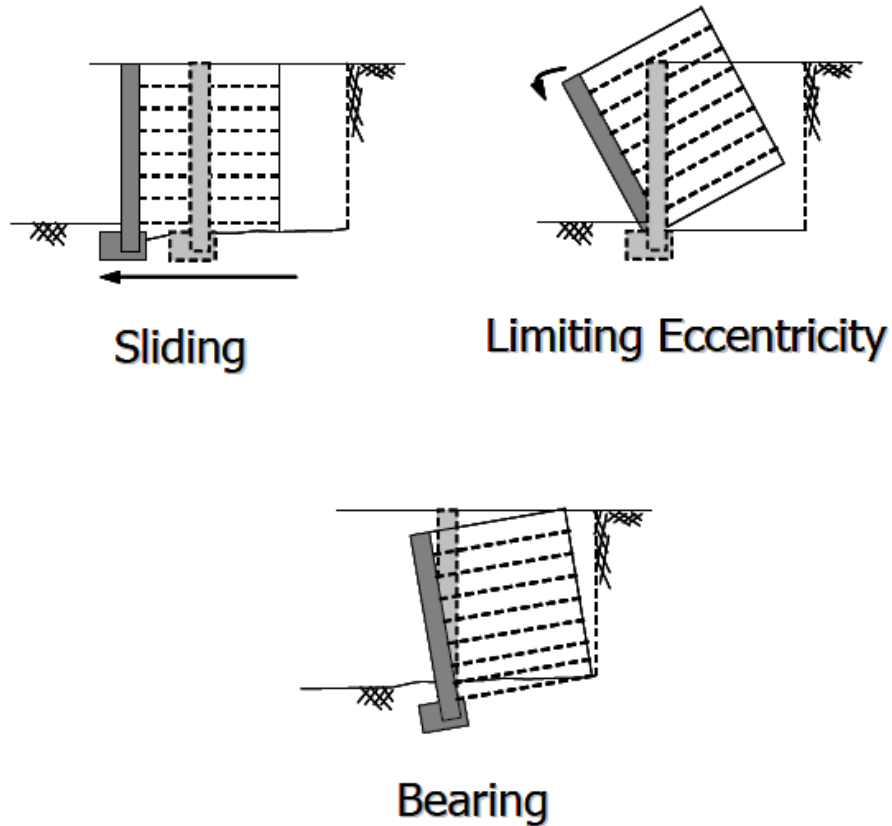


Figure 1.6. Schematic of external stability failures in MSE walls (Berg et al. 2009).

Permanent loads include horizontal earth loads (EH), earth surcharge loads (ES) and vertical pressure from dead loads (EV). Transient loads depend on the specific application of the wall. For use in transportation, for example, a wall must be designed with resistance to vehicular collision forces and vehicular live load. A more general case for a transient load can be an earthquake load (EQ) (Berg et al. 2009). Only loads that apply to MSE walls are required for consideration in the design.

Load factors for different load types are recommended by state and federal agencies. As part of the stability check, load factors consider the minimum and maximum extremes for each load type, resulting in a total extreme factored load effect (WisDOT 2015). Table 1.8 presents values of load factors for different load types. Resistance factors against bearing capacity failure, sliding, and global stability are provided in Table 1.9 (Berg et al. 2009; ASHTO 2010).

Table 1.8. Values of load factors and load combinations (after WisDOT 2015).

Direction of Load	Load Type	Load Factor		
		Strength Limit		Service Limit
		Max.	Min.	
Load Factor for Vertical Loads	Dead load for structural components and non-structural attachments (DC)	1.25	0.90	1.00
	Earth surcharge load (ES)	1.50	0.75	1.00
	Vertical surcharge load (EV)	1.35	1.00	1.00
	Water load (WA)	1.00	1.00	1.00
	Live load surcharge (LS)	1.75	0.00	1.00
	Dead load of wearing surfaces and utilities (DW)	1.50	0.65	1.00
Load Factor for Horizontal Loads	Horizontal Earth Pressure (EH)			
	Active	1.50	0.90	1.00
	At-rest	1.35	0.90	1.00
	Passive	1.35	N/A	1.00
	Earth surcharge (ES)	1.50	0.75	1.00
	Live load surcharge (LS)	1.75	1.75	1.00

Table 1.9. Stability resistance factors for MSE walls (after Berg et al. 2009; AASHTO 2010).

Stability Mode	Condition	Resistance Factor
Bearing Resistance	All	0.65
Sliding	All	1.00
Global Stability	Where geotechnical parameters are well defined, and slope does not support or contain a structural element	0.75
	Where geotechnical parameters are based on limited information, or the slope contains or support a structural element	0.65

1.2.3.2. Geosynthetic Specifications

Most commonly, the selection of geosynthetic reinforcements follow project-specific specifications (Koerner 2009). However, specifications from manufacturing organizations, federal and state agencies, such as the American Association of State Highway and Transportation Officials (AASHTO), and Geosynthetic Institute (GSI) are also available for reference. The Wisconsin Department of Transportation (WisDOT) uses the AASHTO’s M288-06 specifications as a guideline excluding any modifications necessary for specific cases (Koerner 2005; WisDOT 2015).

Holtz et al. (1998) notes that the selection of geosynthetics should follow project specific criteria because geotextiles and geogrids range a broad span of physical and mechanical characteristics. The AASHTO M288-06 specification presented in Table 1.10 summarizes general requirements regarding the use of geotextiles for highway applications.

Table 1.10. Geotextile Strength Property Requirements AASHTO M288-06 (after Koerner 2005).

Geotextile Classifications ⁽¹⁾

	Test Methods	Units	Type 1		Type 2		Type 3	
			Elongation < 50 % ⁽²⁾	Elongation ≥ 50 % ⁽²⁾	Elongation < 50 % ⁽²⁾	Elongation ≥ 50 % ⁽²⁾	Elongation < 50 % ⁽²⁾	Elongation ≥ 50 % ⁽²⁾
Grab strength	ASTM D4632	N	1400	900	1100	700	800	500
Sewn seam strength ⁽³⁾	ASTM D4632	N	1200	810	990	630	720	450
Tear strength	ASTM D4533	N	500	350	400 ⁽⁴⁾	250	300	180
Puncture strengths ⁽⁵⁾	ASTM D4833	N	500	350	400	250	300	180

Notes:

- (1) The severity of installation conditions for the application generally dictate the required geotextile class. Class 1 is specified for more severe or harsh conditions where there is a greater potential for geotextile damage. Class 2 and 3 are specified for less severe condition
- (2) As measured in accordance with ASTM D4632. Note: Woven geotextiles fail at elongation (strains) <50%, while nonwovens fail at elongation (strains) >50%.
- (3) When sewn seams are required. Overlap seam requirements are application specific.
- (4) The required MARV tear strength for woven monofilament geotextiles is 250 N
- (5) Puncture strength will likely change from ASTM D4833 to ASTM D6241 with approximately five times higher values.

The required strength of geogrids is project dependent and defined base on global stability analysis (Koerner 2005). Proposed generic specifications for geogrids are presented in Table 1.11.

Table 1.11. Geogrid Property Recommendations for Reinforcement Applications (after Koerner 2009).

Geogrids		Test Methods (ASTM GRI)	or	Type I (Monolithic PE and PP)	Type II (Coated Yarns)	(a) Type II (Coated Yarns)	(b) Type II (PVA Rods/Straps)	Type III (PET Rods/Straps)	Test Frequency
Allowable Tensile Strength (min.)⁽¹⁾		D6637							
(a) Least strength requirements				10 kN/m	10 kN/m	10 kN/m	10 kN/m		MARV
(b)				20 kN/m	20 kN/m	20 kN/m	20 kN/m		MARV
(c)				30 kN/m	30 kN/m	30 kN/m	30 kN/m		MARV
(d)				40 kN/m	40 kN/m	40 kN/m	40 kN/m		MARV
(e)				50 kN/m	50 kN/m	50 kN/m	50 kN/m		MARV
(f) highest strength requirements⁽²⁾				60 kN/m	60 kN/m	60 kN/m	60 kN/m		MARV
Junction Efficiency (MD)		GG1/GG2		80%	10%	10%	30%		year
Interaction Coefficient⁽³⁾		GG5		0.8	0.8	0.8	0.8		year
Direct Shear⁽³⁾		D5321		30 deg.	31 deg.	32 deg.	33 deg.		year
Default Reduction Factors⁽⁴⁾									
creep (RF_{CR})		GG4		2.8	1.9	1.5	1.9		formulation
installation damage (RF_{ID})		GG4		1.3	1.3	1.3	1.3		formulation
chem/bio degradation (RF_{CBD})		GG4		1.2	1.2	1.2	1.2		formulation
Durability									
oven aging (90 days)		D5721/GG1		75%	n/a	75%	n/a		year
carbon black (range)		D4218		0.5-3.0%	n/a	n/a	n/a		year
UV stability (500 hrs.)		D7238/GG1		70%	70%	70%	70%		year
mol. weight (min.)		GG7		n/a	25,000 gm/mol	25,000 gm/mol	25,000 gm/mol		year
CEG (max.)		GG8		n/a	30m mol/Kg	n/a	30m mol/Kg		year

Notes:

(1) To determine the comparable ultimate tensile strength per ASTM D6637 for each category, these allowable strengths should be multiplied by the product of the appropriate reduction factor as given in the table (unless less conservative values can be justified).

(2) Still higher strength geogrids are generally available from manufacturers on a product-specific basis.

(3) Test conditions are using well graded concrete sand at optimum moisture control and 95% density under 50kPa normal pressure.

(4) These default conditions are to be used unless manufacturer has product-specific and/or site-specific data justifying lower values.

n/a = Not applicable

1.2.3.2. Backfill Specifications

Specifications for backfill for MSE walls follow guidelines set by state and federal agencies. The WisDOT adopts the recommendations set forth by the FHWA and AASHTO except when provisions by the agency are made necessary. The following requirements presented here are consistent with current practice.

The backfill material should be as free as possible of organic and other deleterious materials (Berg et al. 2009; AASHTO 2010; Anderson et al. 2012; WisDOT 2015). Table 1.12 summarizes a range of values for gradation, plasticity index and soundness (Holtz et al. 1998; Berg et al. 2009; AASHTO 2010). The reinforced backfill should be well graded in accordance with the Unified Soil Classification System (USCS) in ASTM D2487.

In addition to the specifications and recommendations regarding grain size distribution, Koerner (2005) suggests a specific backfill gradation for maximizing drainage while minimizing installation damage in geotextiles and geogrids. These values are shown in Table 1.13.

Unstable poorly-graded soils with coefficients of uniformity (C_u) larger than 20 (e.g. with concave upward grain size distributions), and gap-graded soils should be avoided. These types of soil may pipe and erode internally, thus losing materials and causing clogging of drainage systems (Berg et al. 2009).

Table 1.12. MSE wall selected granular reinforced fill requirements (after Berg et al. 2009; AASHTO 2010).

	U.S. Sieve Size	Percent Passing ^(a)
Gradation: (AASHTO T-27)	102 mm (4 in.) ^(a,b)	100
	No. 40 (0.425 mm)	0-60
	No. 200 (0.075mm)	0-15
Plasticity Index: (AASHTO T-90)	PI ≤ 6	
Soundness: (AASHTO T-104)	The materials shall be substantially free of shale or other soft, poor durability particles. The material shall have a magnesium sulfate soundness loss of less than 30% after four cycles (or a sodium sulfate value less than 15 % after five cycles).	

Notes:

(a) To apply default F^* values, C_u should be greater than, or equal to 4.

(b) As a result of recent research on construction survivability of geosynthetics and epoxy coated reinforcements, it is recommended that the maximum particle size for these materials be reduced to (19 mm) for geosynthetics, and epoxy and PVC coated steel reinforcements unless construction damage assessment tests are or have been performed on the reinforcement combination with the specific or similarly graded large size granular fill. Prequalification tests on reinforcements using standard agency fill materials should be considered.

The WisDOT does not recommend use of backfill materials containing foundry sand, bottom ash, or other potentially corrosive material. Additionally, the backfill material must meet the electrochemical criteria by the WisDOT as presented in Table 1.14 (WisDOT 2015).

Table 1.13. Recommended Soil Backfill Gradation for Geotextile and Geogrid Reinforcement Applications (Walls and Slopes) (After Koerner 2005).

Sieve (No.)	Size (mm)	Particle Size	Percent Passing
4	4.76		100
10	2.0		90 - 100
40	0.42		0 - 60
100	0.15		0 - 5
200	0.074		0

Table 1.14. Electrochemical Property Criteria for Reinforced Fill in MSE Walls (WisDOT 2015).

Reinforcement Material	Property	Criteria
Metallic	Resistivity	> 3000 ohm cm/H
Metallic	Chlorides	< 100 ppm
Metallic	Sulfates	< 200 ppm
Metallic / Geosynthetic	pH	3.5 < pH < 9
Metallic / Geosynthetic	pH	4.5 < pH < 10

The recommended maximum effective friction angle (ϕ') assumed for design of reinforced backfill fill is 34° (FHWA 2009 and AASTHO 2010), and 30° (WisDOT 2015) in the absence of specific data. For desired friction angles higher than 30°, direct shear tests (AASSTO T-236) shall be performed on the portion of material finer than the No. 10 sieve (WisDOT 2015). If the measured friction angle exceeds 40°, then the design angle of friction should not exceed 40° (Article 11.10.6.2, AASHTO 2007). Cohesion is considered to be 0.0 kN/m³ for all cases (Berg et al. 2009). The WisDOT recommends a minimum unit weight of 18.9 kN/m³ and cohesion of 0.0 kN/m³ (WisDOT 2015).

1.2.4. MSE Wall Design Procedures

The design procedures presented herein follow the Load and Resistance Factor Design (LRFD) method established by the MSE wall Design Manual by the FHWA Volume I (Berg et al. 2009)

1.2.4.1 Project Parameters

Design of MSE walls shall consider the topography, ground water conditions, and the engineering properties of base, retained and reinforced soils. Engineering parameters include unit weight, friction angle, and cohesion, as applicable for each soil type and condition.

The selection of backfill material follows the guidelines presented in Tables 1.13 and 1.14 of Section 1.2.3.2. Cohesion of the backfill is assumed to be zero and the maximum friction angle of the soil is assumed to be 34° in the absence of specific data. Friction angles larger than 40° for the backfill shall not be used in design even if the measured friction angle is greater than 40° . While 34° is the maximum friction angle allowed in the absence of data, some soils that meet AASHTO specifications will exhibit friction angles lower than 34° . The rounded sands found in the state of Wisconsin are one example of such soils, and laboratory strength tests are recommended. The use of a maximum friction angle of 30° is recommended for base and retained backfill only for preliminary design. Project specific site condition evaluation and laboratory tests are recommended to obtain the minimum friction angle.

1.2.4.2. Wall Embedment and Reinforcement Length

Sizing the MSE wall involves establishing the embedment depth, and the total exposed height of the wall. Guidelines for embedment depth are recommended by the FHWA and are summarized in Table 1.15.

Table 1.15. Minimum wall embedment lengths (after Berg et al. 2009).

Slope in front of the wall	Minimum Embedment Length to top of leveling pad*
All geometries	0.6 m, minimum
Horizontal (walls)	H/20
Horizontal (abutments)	H/10
3H:1V	H/10
2H:1V	H/7
1.5H:1V	H/5

The preliminary minimum length of soil reinforcements is established as $0.7H$ or 2.5 m, whichever is greater, where H is the design height of the wall. This length is necessary to initiate the design, and is checked during external and internal stability calculations. Table 1.16 shows minimum length of reinforcements for MSE walls.

Table 1.16. Minimum preliminary length of reinforcements (after Berg et al. 2009).

Case	Typical minimum L/H ratio
Static loading or surcharge traffic surcharge	0.7
Sloping backfill surcharge	0.8
Seismic loading	0.8 - 1.1

1.2.4.3. Defining Nominal Loads, Load Combinations and Load factors

Earth pressure from the retained earth behind the backfill and surcharge loads above the reinforced zone are the primary sources of external load on MSE walls (nominal loads). Load combinations and load factors, which were presented in Table 1.8 of section 1.2.3.1, are applied to the nominal loads and the factored loads are attained.

1.2.4.4. Evaluating Sliding, Limiting Eccentricity, and Bearing Capacity

Three external failure mechanisms should be considered in MSE wall design. They include sliding on the base, limiting eccentricity (overturning) and bearing resistance. External stability resistance factors for MSE walls are presented in Table 1.10 of Section 1.2.3.1.

Sliding resistance along the base of wall is calculated by considering all horizontal force components acting in the back of the wall. Therefore, two resultant forces are calculated, from the retained backfill, and from the combination of all surcharges on the wall. The most critical frictional properties at the base of the wall are determined. Live forces are not considered in sliding resistance calculations.

Limiting eccentricity is a strength limit check, and only considers the live loads acting above the retained backfill. Eccentricity (e) is calculated by summing the overturning and resistant moments, divided by the sum of vertical loads. Eccentricity is considered acceptable if the location of the resultant vertical force is within the middle one half of the base width ($L=1/4$).

Bearing failure can result in general or local shear modes. Calculated factored bearing pressure must be less than the calculated factored bearing resistance. Live loads above the retained backfill and reinforced zones are applied in bearing check calculations. The weight and width of the wall facing are neglected.

1.2.4.5. Evaluating Settlement

Settlement analysis is carried to check the extent of primary and secondary settlement. If post-construction settlement estimation is significant, the wall elevation must be adjusted. If elevation of the wall is not possible, the base conditions may be improved by wick drains, stone columns, dynamic compaction, or the use of a lighter fill material.

1.2.4.6. Selection of Reinforcement

Reinforcements are selected with consideration given to life time (e.g. corrosion for metals, and degradation for polymers), critical plane failure geometry, and lateral stress. Properties of geotextiles and geogrids are presented in Tables 1.10 and 1.11, respectively.

1.2.4.7. Defining Critical Slip Surface

It is assumed that the critical slip surface coincides with the location of maximum tensile force (T_{max}), in each reinforcement layer, and that it is linear for geosynthetic reinforcements. Because geosynthetics will elongate more than the soil, a Rankine failure surface is considered.

1.2.4.8. Defining Unfactored Loads

The lateral earth pressure from the retained backfill and from the top of the reinforced zone are the primary loads in the MSE wall. Unfactored loads may include vertical earth pressure and live loads. Water, seismic and impact loads may also be considered as appropriate.

1.2.4.9. Vertical Layout of Reinforcements

Vertical spacing of reinforcements should not exceed 800 mm in order to provide a coherent reinforced zone. The reinforcement density (T_{al}/S_v) can be varied by changing the strength (T_{al}), or vertical spacing (S_v). The range of acceptable spacing depends on the placement and compaction of the backfill. S_v can be from one to three times the compacted lift thickness. Low to medium walls (5 m) are commonly built with only geosynthetic strength. Higher walls usually use a combination of different geosynthetic strengths.

1.2.4.10. Calculation of Factored Tensile Forces in the Reinforced Layers

Horizontal and vertical stresses are calculated with depth. The maximum load factor of 1.35, given in Table 1.8, is used to find the critical stress. Horizontal stress in the simplest MSE wall configuration (level backfill and no surcharge) may be given as follows:

$$\sigma_H = K_r [(\gamma_r Z) \gamma_{EV-MAX}] \quad (1.4)$$

where,

K_r = coefficient of lateral earth pressure ($K_r = 1$ for geosynthetics)

γ_r = unit weight of soil in the reinforced soil zone

γ_{EV-MAX} = maximum load factor (1.35) for load type "EV" (Table 1.9)

Calculation of the maximum factored tension (T_{MAX}) in each reinforcement layer per unit width of the wall is based on the horizontal stress (σ_H) and the vertical spacing of reinforcements (S_v):

$$T_{MAX} = \sigma_H S_v \quad (1.5)$$

The value of σ_H is calculated at the level of each reinforcement, except at the bottom and top layers, where the distance S_v is taken as the midpoint between the first and second layer of the reinforcement.

1.2.4.11. Calculating Soil Reinforcement Resistance

The factored soil resistance (T_r) can be calculated as the product of the allowed tension (T_{al}) and the resistance factor (RF), given in Table 1.7.

$$T_r = RF_{\text{tension}} T_{al} \quad (1.6)$$

Equation 1.6 is expressed in terms of strength per unit width of the wall.

1.2.4.13. Selection of the Number of Soil Reinforcement Elements at Each Level

With the vertical layout of reinforcement, the factored tensile forces at each reinforcement level, and the factored reinforcement resistances previously defined, the selection of reinforcement strength can be done for the defined vertical reinforcement layout. With this layout, the pull-out loading can be checked. Stability with respect to breakage of the reinforcements requires that:

$$T_{\text{MAX}} \leq T_r \quad (1.7)$$

where

T_{MAX} = the maximum factored load in a reinforcement

T_r = the factored reinforcement tensile resistance

1.2.4.14. Internal Stability with Respect to Pull-out Failure

For stability with respect to pull-out of the reinforcements, the factored effective pull-out length must be equal to or larger than the factored tensile load in the reinforcement, T_{MAX} . Each layer of reinforcement should be checked, and the following criterion should be satisfied:

$$(RF_{\text{pull-out}}) L_e \geq [T_{\text{MAX}} / (C_i \sigma_v C)] \quad (1.8)$$

where,

L_e = length of embedment in the resisting zone.

T_{MAX} = maximum factored load in a reinforcement

$RF_{\text{pull-out}}$ = resistance factor for soil reinforcement pull-out (see Table 1.7)

C_i = pull-out interaction coefficient

σ_v = nominal vertical stress at the reinforcement level in the resistant zone, including distributed dead load surcharges, neglecting traffic loads

$C = 2$ for strip, grid, and sheet type reinforcement

The total length required for internal stability is:

$$L = L_e + L_a = L_e + (H - z) \tan(45^\circ - \phi'/2) \quad (1.9)$$

where

H = height of the wall

Z = depth to reinforcement level

L_a = length of reinforcement in the active zone

1.2.5. MSE Walls and Recycled Materials

1.2.5.1. Selection of Recycled Material for Backfill

In this section, properties of recycled materials are compared with current design specifications. Values are presented in Table 1.17. Properties considered include gradation, fines content and angle of internal friction.

With the exception of FA, all recycled materials considered here are assumed to be free-draining coarse aggregates that meet the specifications for grain size distribution, maximum fines content, and plasticity ($PI \leq 6$). As noted previously, RCA, BA, and FDS show a wide variation of fines content, which may approach the maximum boundary limits of the specifications. RAS and RAP show less variability of fines content and typically range closer to the lower boundary of the specifications.

Recommended angles of internal friction are maximum values that can be assumed for design. However, data from laboratory tests should be used whenever available. There is a slight difference between recommended friction angles from different specifications. While the WisDOT allows the assumed maximum value of 30° , both the AASHTO and FHWA recommend an assumed value of 34° . All recycled material reviewed in the literature as part of this effort exhibit measured friction angles near or well above the recommended values.

Table 1.17. Summary of MSE Wall backfill specifications and Engineering Properties of Recycled Materials (after Berg et al. 2009; AASHTO 2010 and WisDOT 2015).

	WisDOT	AASHTO	FHWA	RCA	RAP	BA	FA	RAS	FDS
Gradation (USCS)	GW - SC	-	GW SC	GW - SC	GW - SP	GW - SM	ML	SW SP	SP - SC
Fine Content (%)	< 15	< 15	< 15	3.2 - 12.8	0.6 - 3.0	0.0 - 12.0	100	3.8	1.0 - 13.0
ϕ' (degrees) (Assumed)	30	34	34	41 - 63	39 - 44	32 - 45	29 - 40	36	35 - 43

Note: WisDOT=Wisconsin Department of Transportation, AASHTO = American Association of State Highway and Transportation Officials, FHWA=Federal Highway Administration Agency, USCS = United Soil Classification System.). ϕ' =effective friction angle.

1.2.5.2. Selection of Geosynthetic Reinforcements

As noted before, Holtz et al. (1998) adverts that the selection of geosynthetics should follow project specific criteria because geotextiles and geogrids can have a wide range of physical and mechanical characteristics. The selection of geotextile and geogrid reinforcements for MSE wall considers tensile strength, creep susceptibility, reinforcement/soil interaction and durability. Recommended values for such properties are summarized in Tables 1.10 and 1.11.

Creep is a time-dependent deformation under constant load. Creep is especially important when the reinforcements must be selected for a backfill material that is also susceptible to creep, such as RAP (Berg et al. 2009). Values of expected creep of reinforcements should be compared with creep test data performed on the backfill material. Reduction factors listed on Table 1.8 may then be applied.

The friction angle between the backfill and reinforcements (geotextiles and geogrids) is assumed to be between 2/3 the angle of internal friction angle of the backfill material. Interface direct shear testing with the selected backfill is recommended for each prospective geosynthetic reinforcement. Values from different samples of reinforcements may be compared as part of the selection process (Holtz et al. 1998). The friction efficiency for geogrids can be further calculated by correlating geogrid aperture size versus particle size (Koerner 2005). The minimum width of geogrid aperture (B_{GG}) shall be larger than 3.5 times the average particle size of the backfill (e.g. d_{50}) (Sarsby 1985).

The durability of geosynthetic reinforcements is environmentally and backfill dependent. The resistance to corrosion (e.g. pH levels) of a prospective reinforcement should be investigated for each backfill considered (Holtz et al. 1998; Koerner 2005; Berg et al. 2009). Table 1.14 shows pH ranges recommended for geosynthetic materials (WisDOT 2015). Electrochemical test results from the selected backfill shall be investigated to aid in the selection of reinforcements (See subsequent experimental program).

The selection of geogrids does not consider water flux because of the large apertures of the material. For geotextiles, on the other hand, their hydraulic properties become important. The hydraulic conductivity of the geotextile is expressed as a water flow rate, while the permittivity is the flux of water in-plane with the geotextile (Holtz et al. 1998; Koerner 2005). The values of water flux and permittivity for a specific material may be compared with the desired flow rate for a specific project.

2. BENEFICIAL USE FRAMEWORK

The benefits and limitations of using recycled materials as aggregates are discussed in this Chapter. A review of successful and unsuccessful MSE walls built with geosynthetic reinforcements is also presented to provide context.

2.1. Beneficial Use of Recycled Materials as MSE Wall Backfill

The use of recycled materials as aggregates can offer economic and environmental advantages over natural materials. Considerable cost reductions can be attained by incorporating locally available recycled materials into a project in lieu of disposing the materials in landfills. The environmental benefits gained by using recycled materials include the conservation of natural resources, and reduction of greenhouse gas emissions and air and water pollution (Rathje et al. 2006; Edil et al. 2012; Benson et al. 2012).

2.2. Limitations of Recycled Materials as Backfill Aggregates

Recycled aggregates have different compositions than natural aggregates (e.g. mortar in RCA and, asphalt binder in RAP, clay or chemical binders in FSD) and therefore can exhibit distinct behavior under typical loading and environmental conditions compared with natural aggregates.

A characteristic feature of RCA is the cement paste bonded to the aggregates. High alkalinity of calcium hydroxide comprising the cement paste may raise pH levels in RCA-water mixtures to over 11 (Bruinsma et al. 1997; Kuo et al. 2002; Rathje et al. 2006), which surpasses recommended pH levels for the use of geosynthetic reinforcements. In addition, the presence of free lime and portlandite [$\text{Ca}(\text{OH})_2$] in RCA can contribute to precipitation of calcium carbonate, CaCO_3 (tufa) (Muethel 1989; Rathje et al. 2006; Bruinsma et al. 1997). Tufa can potentially clog the filters of drainage systems, potentially leading to accumulation of water behind face of the wall (Rathje et al. 2006).

A characteristic feature of RAP is the bituminous coating on the particles and associated viscous behavior of the bulk material. Creep deformation may develop (Rathje et al. 2006) and result in excessive time- and temperature-dependent deformation (Bleakley et al. 2014; Soleimanbeigi et al. 2015b). Creep deformation of compacted RAP may increase with increasing temperature. In designing MSE walls with RAP as backfill, creep potential of the compacted RAP at different temperatures should be investigated (see subsequent experimental program).

BA is rich in trace elements (Yoon et al. 2009), including Arsenic, Cesium, Mercury, Selenium, Nickel, Lead and Antimony (Huang 1990). The potential leaching of such elements and the consequential contamination of soil and groundwater may pose an environmental concern for the use of BA as backfill material. Studies, however, have found that the contamination of groundwater due to the leaching of heavy metals in BA is minimum (Yoon et al. 2009). Edil et al. (2005a) observed that levels of Cadmium, Chromium, Selenium and Silver found in leachate from BA met the criteria in the Wisconsin Administrative Code (Table 2.1).

FA is classified as low plasticity silt (ML) by the Unified Soil Classification System (USCS), with an amount of fines far exceeding current specifications. Class “C” fly ash hardens in contact with water, and therefore it is not recommended as backfill material (FHWA 1997). Edil et al. (2005b) reported concentrations of Chromium, Cadmium and Silver in FA samples (lower than

in natural soil), but within the limit stipulated in Sections NR 538 and NR 140 of the Wisconsin Administrative Code (Table 2.1).

RAS has high compressibility compared to natural aggregates, and thus can require further stabilization (e.g. addition of self-cementing FA, or mixing with granular material) to become suitable as backfill material. Like RAP, RAS may exhibit temperature-dependent creep deformation due to its bituminous content (Soleimanbeigi et al. 2012 and 2015).

FDS may contain considerable amounts of clay, which can negatively affect drainage in backfill constructed with FDS (Partridge et al. 1999). The plasticity index of FDS varies from non-plastic to 12 (Goodhue et al. 2001), and could potentially fall outside of the current recommendations (e.g. $PI \leq 6$). Waste FDS, due to its composition, may also exhibit higher deformation and creep compared to conventional backfill materials under typical loading conditions.

Table 2.1. Regulatory Limits for Cadmium, Chromium, Selenium and Silver as defined by Sections 538 and 140 of Wisconsin Administrative Code (after Edil et al. 2005a)

Element	Maximum Concentration (µg/L)	
	NR 538	NR 140
Cadmium	25	5
Chromium	500	100
Selenium	250	50
Silver	250	50

2.3. Geosynthetically Reinforced MSE Walls: Failure Modes and Case Histories

2.3.1. Failure Modes

The modes of failure of MSE walls are divided into excessive deformation and collapse. Of 141 reported case history failures, *internal instability*; e.g., wide spacing, short lengths and low shear strength soil, accounts for 37 cases (26%), *external instability*; e.g., poor foundations, sloping exit angles, excessive surcharge loads, seismicity and low global shear strength accounts for 23 cases (16%); *internal water*; e.g., leaking drainage systems, broken water mains, and infiltrating water, accounts for 51 cases (36%); and *external water*; e.g., from the retained zone, tension cracks and elevated water level, accounts for 30 cases (22%) (Koerner and Koerner 2012).

The primary causes of MSE wall failures are reported to be inadequate or improper design and/or construction. The *major design inadequacy* appears to be the lack of proper drainage procedures. The *major construction inadequacy* is the use of fine-grained silt or clay backfill soils and inadequate placement and compaction. Corresponding poor drainage leads to hydraulic pressures mobilized behind or within the reinforced soil zone, and requires the use of back and base drains to dissipate the pressures and remove the water at the front of the wall (Koerner and Koerner 2012). Figure 2.1 shows different failure modes for illustration.

Precipitation of tufa in RCA can potentially clog the drainage filters and therefore evaluation of

hydraulic properties and drainage capacity of RCA is a key requirement to verify adequate drainage of the backfill for proper MSE wall design. Creep of RAP due to asphalt binder content can potentially lead to excessive deformation and failure of the MSE and thus also needs to be characterized.

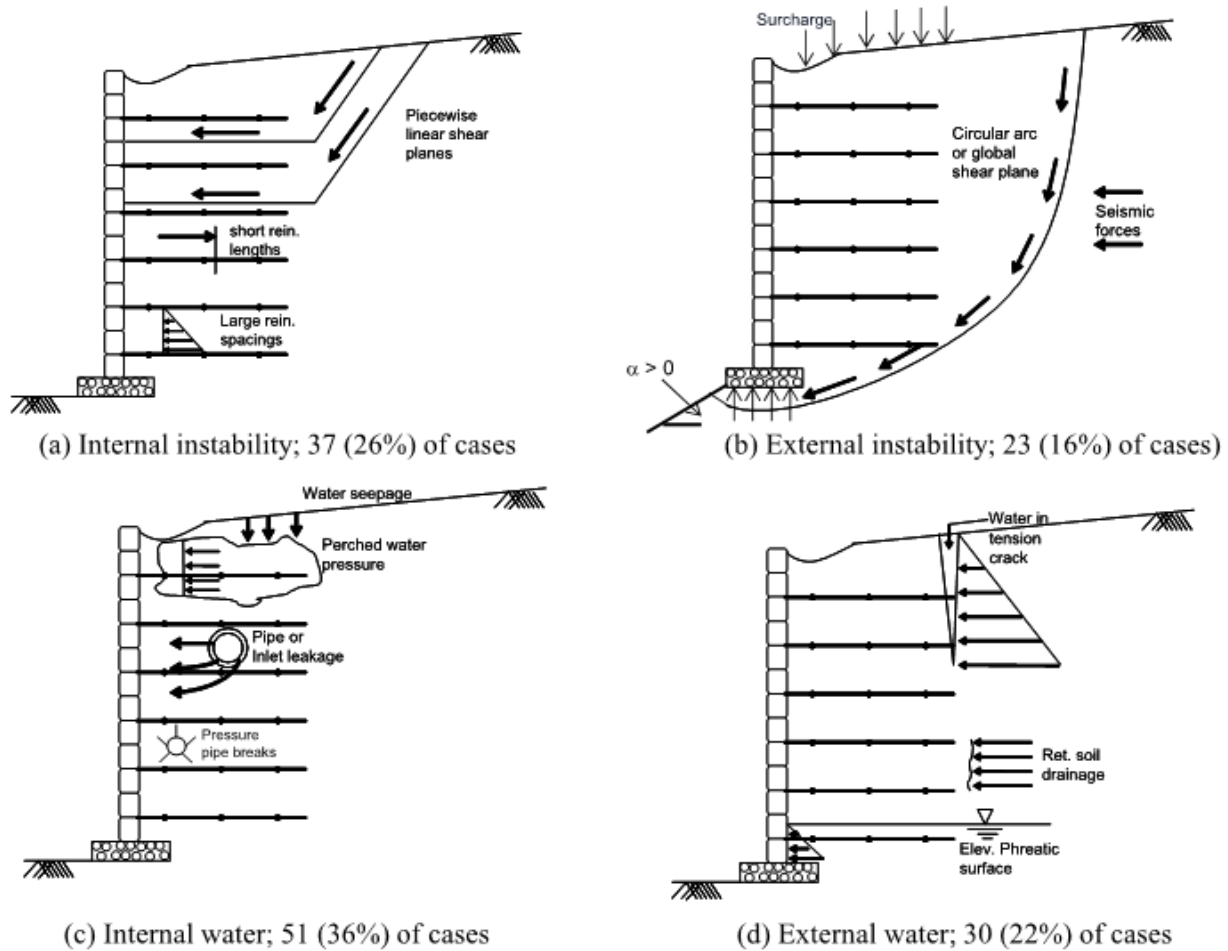


Figure 2.1. MSE wall failure mechanisms (after Koerner and Koerner 2012)

2.3.2. Case Histories

2.3.2.1. Snailback Geotextile Shotcrete Wrapped Face Wall, Siskiyou National Forest, Oregon, 1974

The Snailback MSE wall was the first geosynthetic wall constructed in the United States, and the third in the world. The wall was 2.9-m high and had an additional 0.9-m sloped soil surcharge. The backfill material consisted of uniform sub-rounded fine to medium sand. Nonwoven needle punched geotextile (Fibratex 420, [420 g/m²]) was used as reinforcement. The geotextile was installed with XMD aligned with the tensile load direction, and the overlap behind the face was 1.5 meters.

Post-construction evaluation of the geotextile reinforcement was not conducted. However, because non-aggressive soil was used as a backfill, it is believed that damage due to installation and loss of strength of the reinforcement were kept to a minimum. Although no maintenance has been performed on the wall since it was built, a long-term performance observation carried out in 1999 indicated no evidence of wall deformation, concluding that the wall performed well. No displacement data was collected during the observation. The cross-section of the wall is shown in Figure 2.2.

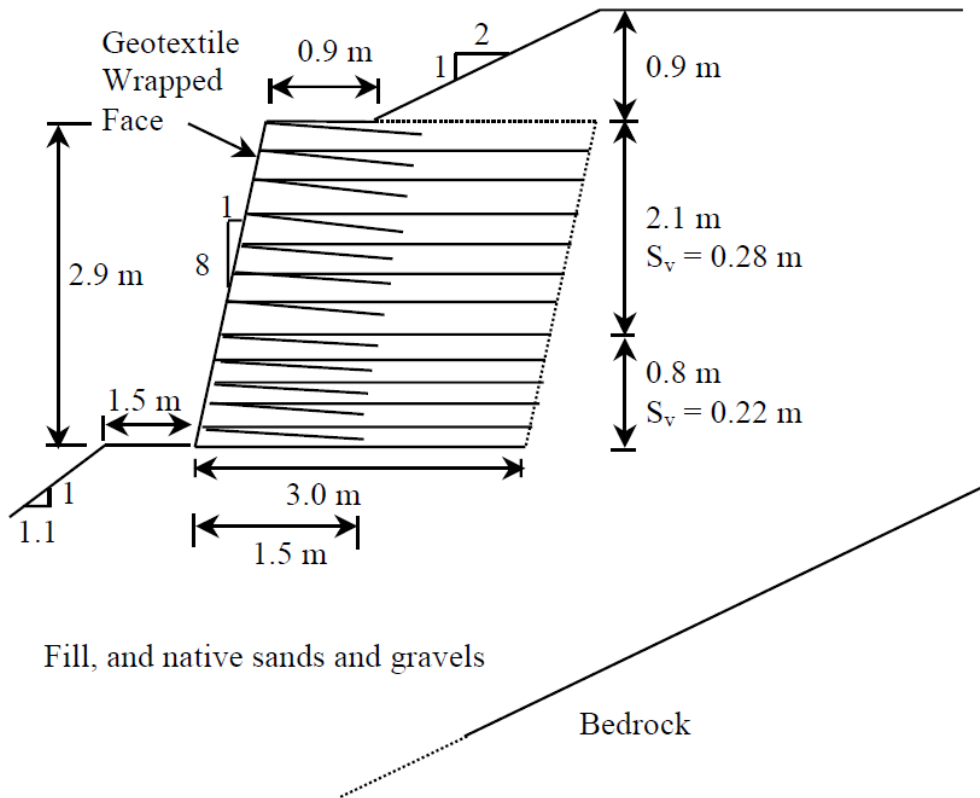


Figure 2.2. Cross-section for the Snailback MSE wall in the Siskiyou National Forest, Oregon (Allen et al. 2001).

2.3.2.2. Propped Panel Geogrid Wall, London, Ontario, 1989

In 1989, a MSE wall was built in London, Ontario, as part of the reconstruction of the Highbury Avenue. The wall is 7.1-m tall, with precast concrete panel facing. The backfill used was silty sand and gravel, conforming to the local soil gradation requirements. The selected backfill was reinforced with uniaxial HDPE geogrids (UX1600 Tensar).

The wall suffered a maximum deformation of 44 mm and the geogrid a maximum strain of 3.5%. The deformation was measured at the very top portion of the wall and occurred within 6 months from the removal of the temporary support members. Geogrid strains occurred near the face of the wall and were likely the result of downward movement of the backfill. The wall has not

suffered excessive deformation since it was built (Allen et al. 2001). The cross-section of the wall is shown in Figure 2.3.

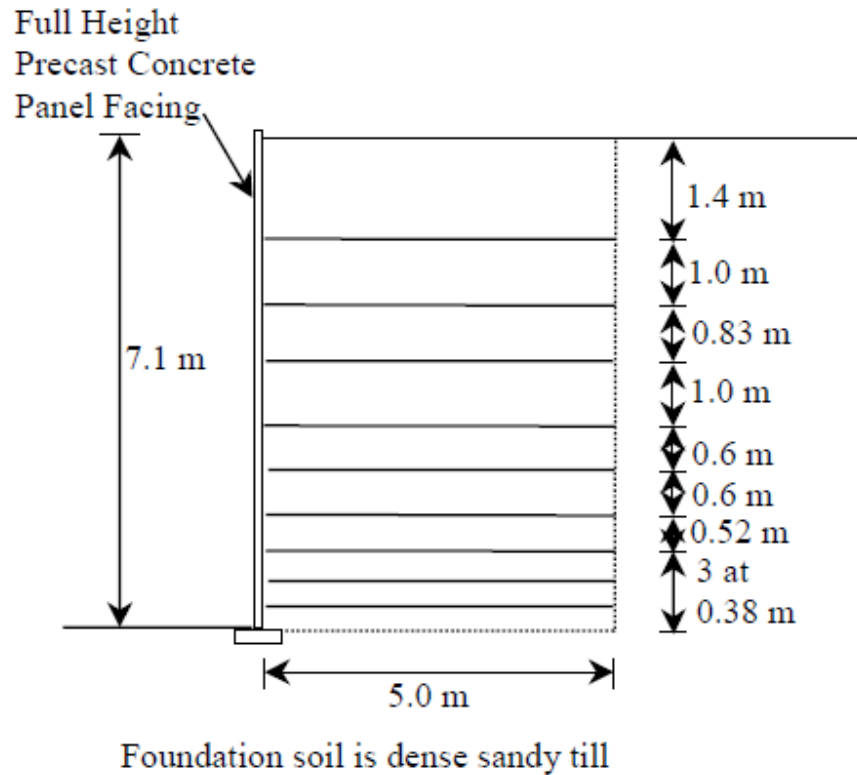


Figure 2.3. Cross-section for geogrid reinforced MSE wall, London, Ontario (Allen et al. 2001).

2.3.2.3. Devils Punch Bowl Wrapped Face Geogrid Wall, Devils Punch Bowl State Park, Oregon, 1982

The Devils Punch Bowl MSE wall was the first permanent geogrid wall constructed in the United States. The wrapped-face geogrid wall was constructed to support roadway access to the State Park in 1982. The wall is 8.8-m high, with a face angle nearing 80 degrees. Crushed basalt was selected as backfill material and HDPE geogrids (Tensar SR-2) were used to reinforce the backfill. The MSE wall is subject to traffic surcharge from the roadway.

Observations carried in 1993 found little signs of movement since construction. The geogrid was reported to be in excellent condition with no apparent sign of degradation or damage (Allen et al. 2001). The cross-section of the wall is shown in Figure 2.4.

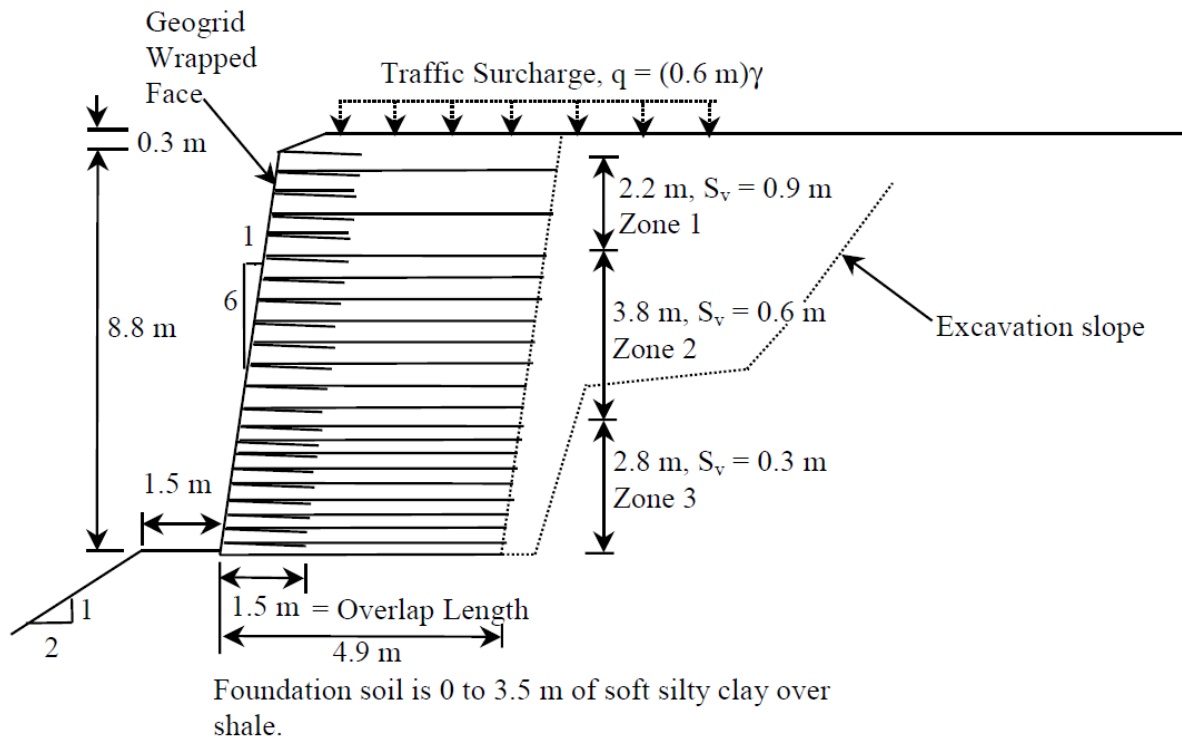


Figure 2.4. Cross-section for the wrapped face geogrid MSE wall in Devils Punch Bowl State Park, Oregon (Allen et al. 2001).

2.3.2.4. Tanque Verde Geogrid Concrete Panel Wall, Tucson, Arizona, 1984

Forty six MSE wall sections were constructed in Tucson, Arizona as part of the Tanque Verde-Wrightstown-Pantano Roads project. This was the first geogrid reinforced MSE wall with precast facing constructed in the United States (Geosynthetics 2009). The wall segments were built to provide grade separation for the intersection of three roads.

The 4.65-m high MSE wall consists of clean, well-graded gravelly sand backfill, HDPE geogrid reinforcements (Tensar SR-2), and full height precast concrete panel facing. The panels were propped until the completion of 2/3 of the backfill behind the face. After completion, the MSE wall was subjected to traffic surcharge.

The peak temperature inside the backfill was recorded at 38° C, with average of 25 to 30° C. The maximum strain at the end of the construction was reported at 0.3%, and happened at the connection between the wall and reinforcements. Post-construction inspection found that the maximum strain occurred in geogrids was 1.0%, most of which happened during the construction of the wall. In 1992, samples of the geogrid reinforcement were exhumed. Analysis of these samples showed no significant reduction in tensile strength of the reinforcements (Allen et al. 2001). The cross-section of the wall is shown in Figure 2.5.

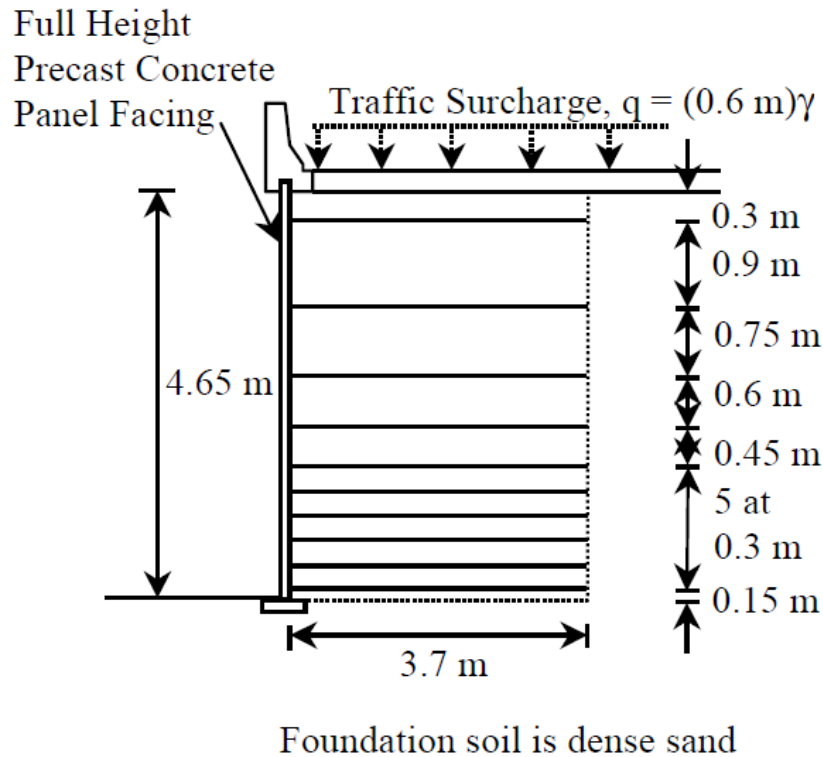


Figure 2.5. Cross-section for the precast concrete, geogrid reinforced MSE wall in Tucson, Arizona (Allen et al. 2001).

2.3.2.5. Tower Oaks Residential MSE wall failure, Rockville, Maryland, 2003 (Mahmood 2009)

The Tower Oaks MSE wall was constructed in 1996, along the eastern side of the Tower Oaks residential development in Rockville, Maryland. The wall was built with to the height of 4.5 m., with silty soil backfill and geogrids reinforcement. Segmental blocks were used for the facing component.

In late 2002, large scarps appeared along the slope at the top of the wall at distances between 4 and 5 m from the wall face (Figure 2.6). Large gaps and separation between the segmental blocks were observed (Figure 2.7). The largest amount of bulging occurred at locations where the wall was the highest. Horizontal separations between the facing blocks were measured up to 2.5 cm. thick, and continued to grow until the wall collapse in 2003.

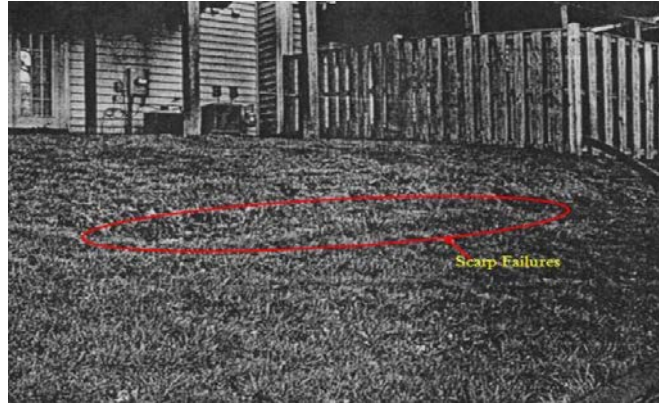


Figure 2.6. Scarps located at the top of the wall (Mahmood 2009).

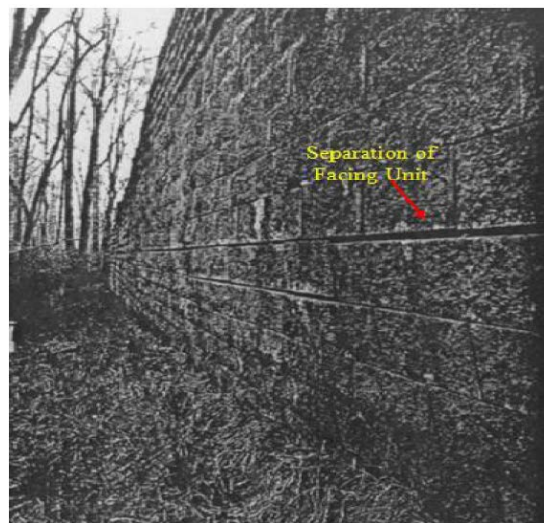


Figure 2.7. Visible bulging and separation between facing blocks (Mahmood 2009).

Forensic investigation concluded that the collapse of the wall was caused by failures in the reinforcements, combined with poor drainage of the backfill. Improper installation of the geogrids allowed bends and slacks, which impaired proper tensioning of the geogrids. It was also concluded that the length of the geogrids was insufficient at the top three layers of the wall. The silty soils used as backfill (ML) had low permeability and did not provide adequate drainage within the wall system. Hydrostatic pressure developed at the face component and at the end of the reinforced zone where depressions occurred.

2.3.2.6. Segmental Block MSE Wall Failure, SW Virginia, 2001 (Scarborough 2005)

This MSE wall was constructed in 1999 adjacent to and below an existing car wash. The width of the wall was 152 m with a maximum height of 9.1 m. The backfill consisted of clayey soil reinforced with geogrids. Segmental blocks were chosen as the facing unit. The cross section of the wall showing the location of the geogrid layers is provided in Figure 2.8.

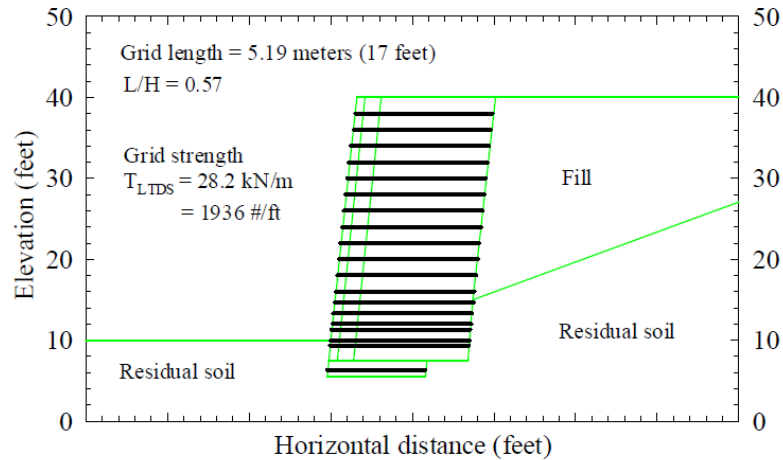


Figure 2.8. Cross section of the MSE wall in Southwestern Virginia (Scarborough 2005).

Cracking of some facing blocks was observed approximately one month after completion of the wall. Failure occurred nearly one year from its completion. Post-failure investigation of the site found cracking in the ground surface at the top of the wall, about 4.5 to 11 m from the wall face. The geogrids were apparently pulled out from between individual facing blocks, while the reinforced backfill was generally intact. Failure (Figure 2.9) was mainly restricted to the wall blocks and the crushed rock used as drainage material behind the wall facing unit.



Figure 2.9. Failure of the MSE wall in Southwestern Virginia showing shallow failure surface behind the wall facing (Scarborough 2005).

Forensic investigation performed after the failure characterized the compaction of the backfill as erratic. Testing indicated water contents varying from 20%, to over 40% in the retained, and reinforced fills. Largest moisture contents were approximately 15 to 20 points higher than the corresponding optimum water content from Proctor compaction testing. In-place densities varied from 80% to more than 100% of the standard Proctor maximum dry density.

Investigation of the design documents found that the original design was complete for a 7.3 m. height wall. An additional 1.8 m were added by the contractor without consultation of the design engineer. Global stability analysis of the as-designed geometry found a factor of safety of 1.24, however, this factor of safety fell below one for the full height of the constructed wall.

After laboratory and site forensic investigation, it was concluded that most likely cause of failure was poor drainage, leading to excessive pore pressures behind the wall facing. Contributing factors included poor compaction, the increase of wall height, and use of clayey soil in the reinforced zone.

2.3.2.7. Segmental Block MSE Wall Deformation, East. Tenn., 2001 (Scarborough 2005)

This MSE wall was constructed in 2000 in eastern Tennessee along and below a proposed site for an office building. The wall was 137-m long and 8.5-m high. The reinforced backfill consisted of clayey soil reinforced with geogrids. Segmental masonry blocks were used for the facing component. The cross section of the wall is shown in Figure 2.10.

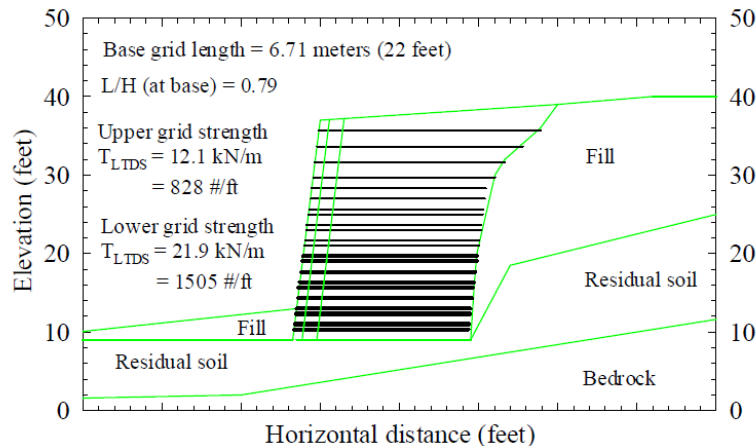


Figure 2.10. Cross section of the MSE in eastern Tennessee (Scarborough 2005).

The MSE wall failed nine months after its completion. Failure was observed as excessive movement of the retained fill, including unloaded building foundations and lateral movements of about 150 mm. Movement was also observed in nearby buried utility ducts and manholes. After failure, drilled shafts were installed under and just beyond the reinforced zone.

Forensic investigation on the wall and design documents concluded that no global stability analysis was performed during design. Although internal, external and facing stability were

found adequate as-designed, it was found that if global stability check had been performed, longer layers of geogrid would have been required. In addition, the magnitude of the movements observed was likely affected by the use of clayey soils as backfill.

3. MATERIALS AND METHODS

Index, mechanical, and hydraulic properties of RAP and RCA were evaluated according to ASTM International (ASTM) standard test procedures, except when such tests were not available. The tests performed included grain size distribution, specific gravity, standard Proctor compaction, large scale triaxial compression tests, direct shear tests, pull-out tests, and creep tests. Additionally, to evaluate the drainage compatibility of RCA with geotextiles, long-term gradient ratio tests were performed. Two types of geotextiles (woven and non-woven) and two types of geogrids (uniaxial and biaxial) were considered to evaluate representative geosynthetic reinforcement materials. Interface shear resistance between the geosynthetics and the recycled materials were measured using a pull-out test apparatus and a large-scale direct shear machine. In this Chapter, the procedures and equipment used to quantify the index, mechanical, and drainage properties of the aggregates and their interaction with geosynthetics are summarized. The properties of each selected geosynthetic reinforcement are also presented.

3.1. Recycled Aggregates and Geosynthetic Reinforcements

3.1.1. Index Properties

3.1.1.1. Recycled Concrete Aggregate

Samples of RCA were obtained from two different sources. RCA sample used to evaluate drainage properties was obtained from a facility in Chantilly, northern Virginia, where concrete is frequently crushed and produced as aggregate for use in road and structural fill applications. RCA sample used in all other tests was obtained from Mandt Sandfill, located in Fitchburg, Wisconsin [Figure 3.1(a)].

The RCA particles were angular with rough particle surfaces and contained noticeable attached (bonded to aggregate) and separated (unbonded to aggregate) mortar. Inspection of the samples showed the presence of contaminant materials (e.g. wood chips, glass, tiles, plastic), consisting of approximately 0.6% of the bulk sample by mass [Figure 3.1 (b)]. Grain size distribution (GSD) tests were conducted following ASTM C136 and ASTM C117 test procedures.

The RCA used for drainage properties had approximately 8% fines content and 60% fine sand sized particles, which is right at the boundary of acceptable granular backfill as defined by Berg et al. (2009). This material was classified as SW-SM (i.e., well-graded sand to silty sand) according to the Unified Soil Classification System (USCS). This RCA was specifically selected for the study because it was considered representative material to evaluate drainage characteristics for an upper threshold (worst case) of acceptable granular material.

The RCA used for all other tests was medium gravel in size with 8.7% fines content. This RCA was classified as GP (i.e. poorly graded gravel) according to USCS.

The mortar content of RCA used in mechanical analyses was determined from Thermal Treatment Method, as described in Butler et al. (2011). An RCA Sample was placed in water and allowed to saturate for 24 h. The RCA sample was heated at 500 °C for 2 h in a furnace chamber. At this temperature, the mortar dehydrated and tensional cracks were developed. After heating the sample was immediately placed into cold water (4 °C). The sudden change in temperature results in the breakdown of mortar attached to the natural particles. The mortar was removed by rubber hammer and manual scraper. This process produced a mortar content for the RCA of 35.7%. The specific gravity (G_s) and water adsorption of the RCA particles were measured according to ASTM C127 and ASTM D854, respectively. The RCA sample used for mechanical tests had G_s of 2.56 and the sample for hydraulic test had G_s of 2.79. The water adsorption of the RCA sample used for mechanical tests was 4.34% measured according to ASTM C127.

Standard Proctor compaction tests conducted per ASTM D698, Method C revealed a maximum dry unit weight of 19.5 kN/m³ for both RCA samples. An optimum water content of 14.5% was obtained for the RCA sample used for drainage evaluation and 11.0% for the sample used for mechanical property tests.



Figure 3.1. RCA sample from Mandt Sandfill, Fitchburg, WI (a) and impurities found in RCA sample include broken glass, wood, chips and tile pieces (b).

3.1.1.2. Recycled Asphalt Pavement

Samples of RAP were acquired from Payne and Dolan, located in Fitchburg, Wisconsin (Figure 3.2). RAP particles were angular with rough surface texture. Bituminous coating was noticeable on the surface of the particles. RAP has approximately 5.10% of fines and was classified as SP (poorly-graded sand).

Asphalt content of 5.58% was measured by loss on ignition (LOI) testing using an automatic ignition furnace. Sample of RAP was heated to 540 °C. The mass loss of the sample was measured by an automated scale inside the furnace. Asphalt content was calculated as the

difference between initial and final masses following the ASTM D6307 procedure. Specific gravity of 2.39 and water absorption of 2.58% were measured according to ASTM C127 and D854. Maximum dry unit weight of 18 kN/m³ was achieved at 4.0% optimum water content following standard the Proctor compaction test according to ASTM D698, Method C. The index properties of RCA and RAP measured in this study, including comparative values reported in the literature, are summarized in Table 3.1.



Figure 3.2. RAP Sample from Payne and Dolan, Fitchburg, WI

Table 3.1. Index Properties of RCA and RAP acquired in this study compared to values observed in the literature.

	RCA (Measured)	RCA (Literature)	RAP (Measured)	RAP (Literature)
USCS	GP	GW, GP, SW, SP, SC	SP	GW, SW, SP
Fine Content (%)	8.70	3.2 - 12.8	5.10	0.6 - 3.0
Mortar/Asphalt (%)	35.7	37.0 – 65.0	5.84	3.5 - 7.1
Absorption (%)	4.34	5.0 - 6.5	2.58	0.6 - 2.0
Specific Gravity, G_s	2.56	2.24 - 2.72	2.39	2.20 - 2.56
γ_{d,max} (kN/m³) (Standard)	19.5	17.5 - 19.2	18.6	13.9 - 19.4
w_{opt} (%)	11.0	8.7 - 11.9	4.0	5.2 - 8.8
k (cm/s)	-	7.1x10 ⁻⁴ - 1.8x10 ⁻³	-	1.1x10 ⁻⁴ - 1.6x10 ⁻³

Note: USCS = United Soil Classification System, AASHTO = American Association of State Highway and Transportation Officials (soil classification system). Mortar content for RCA, asphalt content for RAP. G_s = specific gravity; γ_{d,max}= maximum dry unit weight; w_{opt}=optimum water content, and k=hydraulic conductivity.

3.1.2. Geosynthetic Reinforcement

Four geosynthetic reinforcements commonly used in industry were selected in this study (uniaxial and biaxial geogrids, and woven and nonwoven geotextiles) to assess their interaction properties with RAP and RCA. Selection of these products was based on consideration of specification requirements for MSE wall designs such as strength, hydraulic properties, and friction/interlock efficiency between the aggregate and geosynthetics.

The uniaxial geogrid chosen was Tensar UX-1500MSE, which is commonly used as structural earth reinforcement, as shown in Figure 3.3(a). The material is made of high density polyethylene (HDPE) that is integrally formed punched and uniaxially drawn. The aperture dimensions are 406.0 mm in MD (machine direction) and 17.0 mm in the XD (cross-machine direction). The rib thicknesses are 1.5 mm in MD and 4.2 mm in XD. This material was selected due to its extensive application by the industry as MSE wall reinforcement.

The selected biaxial geogrid was Tensar BX-4200, which is made with polypropylene polymer (PP) as shown in Figure 3.3(b). This geogrid has an aperture size of 33.0 mm in both MD and XD. Rib thicknesses are 1.3 mm in both MD and XD. Selection of Tensar BX-4200 was based on frictional efficiency determined from aggregate sizes and geogrid aperture dimensions. Equation 2.1 gives the minimum required aperture size of the geogrid as a function of average particle size, as recommended by Sarsby (1985):

$$B_{GG} > 3.5 d_{50} \quad (3.1)$$

where

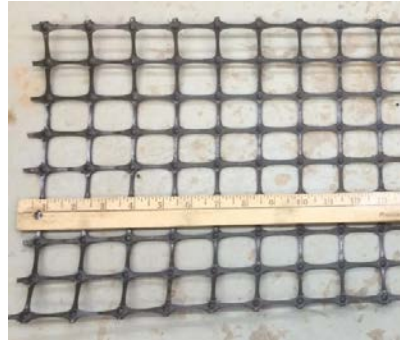
B_{GG} = the minimum width of geogrid aperture, and
 d_{50} = the average particle size of the backfilling aggregate

The woven geotextile selected was Thrace-LINQ GTF-570. This geotextile is manufactured using high tenacity polypropylene multifilament, woven in a stable wave pattern [Figure 3.3(c)]. The apparent opening size was reported by the manufacturer as 0.6 mm and the water flow rate as 1,222.0 l/min/m². The strength of this geotextile falls mid-range compared to similar products. Thrace-LINQ GTF-570 is considered representative of woven geotextiles available for reinforcement purposes and has required values of water flow rate and wide width tensile strength for typical reinforced soils.

The non-woven geotextile used was Thrace-LINQ 160EX, which is produced from polypropylene staple fibers that are randomly oriented to form a stabilized needle punched fabric [Figure 3.3(d)]. The selection of this geotextile was based on consideration of its high water flow rate and wide width tensile strength. Both properties were considered to be representative of the non-woven geotextiles available for MSE wall reinforcements. Minimum average roll values (MARV) of several index and mechanical/structural properties of the selected geosynthetics are provided in Table 3.2. MARV is calculated as the average value less two standard deviations.



(a)



(b)



(c)



(d)

Figure 3.3. (a) Uniaxial geogrid Tensor UX-1500MSE, (b) Biaxial geogrid Tensor BX-4200, (c) Woven geotextile Thrace-LINQ GTF570, (d) Non-woven geotextile Thrace-LINQ 160EX.

Table 3.2. Minimum average roll values (MARV) for several index and mechanical/structural properties of the selected geosynthetics.

					Uniaxial Geogrid	Biaxial Geogrid	Woven Geotextile	Non-Woven Geotextile
					HDPE	PP	HTPE	PP
		Test	Units	Direction	MARV			
Index Properties/ Structural Integrity	Aperture Dimensions	Nominal	mm	MD	406	33	n/a	n/a
				XD	17	33	n/a	n/a
	Minimum Rib Thickness	Nominal	mm	MD	-	1.27	n/a	n/a
				XD	-	1.27	n/a	n/a
	Grab Tensile Strength	ASTM D 4632	N	MD	-	-	2113	801
				XD	-	-	1957	-
	Grab Tensile Elongation	ASTM D 4632	%	MD	-	-	12	50
				XD	-	-	6	-
	Wide Width Tensile Strength (Ultimate)	ASTM D 4595	kN/m	MD	-	-	70	-
				XD	-	-	70	-
	Wide Width Elongation	ASTM D 4595	%	MD	-	-	9	-
				XD	-	-	5.5	-
	Ultimate Tensile Strain	ASTM D 6637	KN/m	MD	114	20.5	-	-
XD				-	23.5	-	-	
Tensile Strength @ 5% Strain	ASTM D 6637	KN/m	MD	52	11.7	-	-	
			XD	-	14.6	-	-	
Tensile Strength @ 2% Strain	ASTM D 6637	KN/m	MD	52	6	-	-	
			XD	-	7.4	-	-	
Trapezoidal Tear	ASTM D 4533	N	MD	-	-	801	334	
			XD	-	-	801	-	
Junction Strength	GRI-GG2-05	KN/m	MD	105	-	-	-	
			XD	-	-	-	-	
Junction Efficiency	ASTM D 7737	%	MD	-	93	n/a	n/a	
			XD	-	-	n/a	n/a	

Table 3.2. (Continued)

					Uniaxial Geogrid	Biaxial Geogrid	Woven Geotextile	Non-Woven Geotextile
					HDPE	PP	HTPE	PP
		Test	Units	Direction	MARV			
Index Properties/ Structural Integrity	Flexural Stiffness	ASTM D 5732	mg-cm	MD	5,100,000	750,000	-	-
				XD	-	-	-	-
	CBR Puncture	ASTM D 6241	N	MD	-	-	8896	2113
				XD	-	-	-	-
	Permittivity	ASTM D 4491	sec ⁻¹	MD	-	-	0.4	1.5
XD				-	-	-	-	
Water Flow Rate	ASTM D 4491	l/min/m ²	MD	-	-	1222	4482	
			XD	-	-	-	-	
Apparent Opening Size (AOS)	ASTM D 4751	mm	MD	-	-	0.6	0.15	
			XD	-	-	-	-	
Durability	Resistance to long Term Degradation	EPA 9090	%	n/a	100	100	-	-
	Resistance to UV Degradation	ASTM D 4355	%	n/a	95	95	80	70

Note: MARV=minimum average roll values, HDPE=high density polyethylene, PP=polypropylene, MD= machine direction, XD=cross-machine direction, n/a= not applicable

For the drainage tests, a typical nonwoven geotextile used for filtration purposes was selected and for the woven geotextile a typical geotextile used in geosynthetically reinforced structures was selected. Properties of the selected geotextile are shown in Table 3.3.

Table 3.3. Physical and hydraulic properties of the geotextiles used in this study.

Name	Structure, polymer type	Hydraulic Properties			Physical Properties				
		Apparent opening size, <i>AOS</i> (mm)	Permittivity, ψ (s^{-1})	Porosity, <i>n</i> (%)	Mass/unit area (g/m^2)	Thickness (mm)	Grab tensile strength (N)	Puncture (N)	Ultimate wide-width tensile strength (kN/m)
NW	NW, NP, PP	0.212	1.7	87	163	1.4	534	1380	NA
W	W, FY, PP	0.6	0.40	NA	490	0.65	NA	NA	70

Note: NW: nonwoven, NP: needle punched, W: woven, FY: Fibrilated yarn, PP: polypropylene, NA: not analyzed. The thickness, mass/per unit area, permittivity, and apparent opening sizes were determined using the appropriate ASTM standardized methods. The grab, puncture and wide-width strengths are the manufacturer’s minimum average roll value (MARV) for each geotextile. All strengths are the machine direction values.

3.2. Laboratory Tests

3.2.1. Large Scale Triaxial Test

A large-scale triaxial test apparatus was used to evaluate shear strengths of compacted RCA and RAP. Monotonic loading tests were performed using an MTS closed-loop servo-electro-hydraulic system. The test followed recommendations of ASTM D7181 (Standard Test Method for Consolidated Drained Triaxial Compression Test for Soils).

The triaxial compression testing equipment consisted of a pressure board used to apply cell pressure and backpressures, and a triaxial cell able to accommodate a specimen of 152-mm diameter and 310-mm high. Vertical force was applied to the specimen by an actuator with a maximum load capacity of 22 kN. A piston attached to the actuator intruded the cell and was seated on top of the specimen. Vertical deformation was measured by a LVDT mounted on the actuator piston. Data was acquired using LabView® installed in a PC equipped with data acquisition card.

The samples were compacted to the desired density (95% of γ_{dmax} and w_{opt}) inside a splitting mold and then enveloped by an impermeable membrane. Porous stones were placed on either ends of the specimen to provide drainage during the test. Figure 3.4 shows an assembled RCA specimen for triaxial compression testing. The specimens were saturated until a B-value of 90% or higher was attained. The specimens were compressed using four confining pressures of 35 kPa, 70 kPa, 105 kPa, and 140 kPa. The specimens were compressed for 24 h at each confining pressure and were then sheared at an axial loading rate of 0.2 mm/min. During the test the

backpressure valve was open to accommodate drained pore pressure conditions. Tests were run until failure of each specimen.

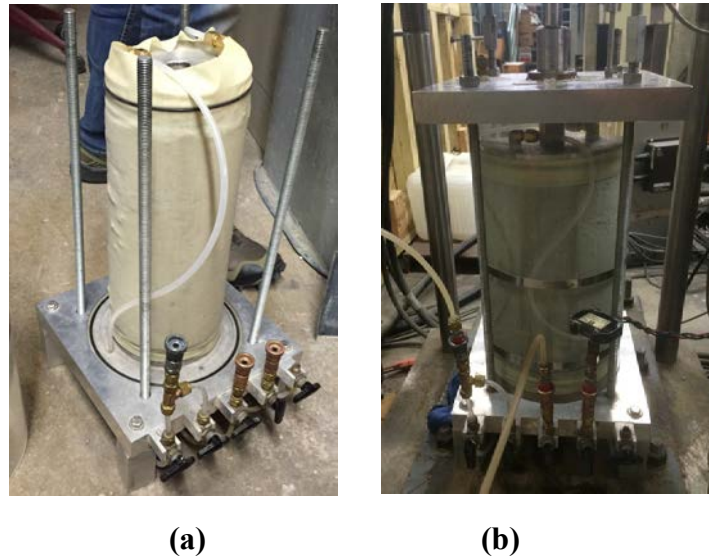


Figure 3.4. (a) RCA sample enveloped by a rubber membrane during triaxial test setup. (b) Sample under confined pressure and vertical load during test.

3.2.2. Large Scale Interface Direct Shear Test

Interface friction angles between RCA, RAP, and the selected geosynthetics were evaluated by interface direct shear testing following test method ASTM D5321. The large scale direct shear testing machine (Figure 3.5) included an upper box with dimensions of 300-mm long, 300-mm wide, and 76-mm deep, and a lower box of 356-mm long, 300-mm wide, and 76-mm deep. The longer length of the lower box afforded stress calculations without requiring an area correction.

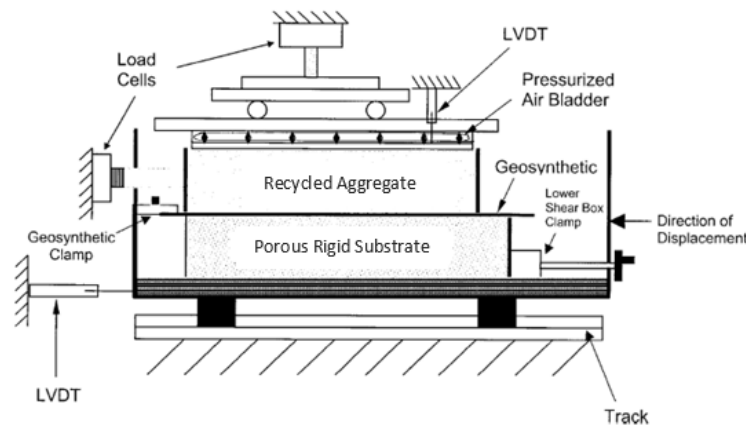


Figure 3.5. Schematic figure of large scale interface direct shear apparatus (adapted from Goodhue et al. 2001)

A porous, rigid, plastic substrate was used in the lower box to provide drainage and a solid base for the geosynthetic. The geosynthetic was placed on top of the plastic base and clamped to the outer end of the lower box. Recycled aggregate samples were placed and compacted on top of the geosynthetic.

Normal pressure was applied by an air bladder affixed under a square top platen. The top platen was placed directly on top of the backfill and was confined by a steel plate connected to the outer frame. The shear box was constrained inside of an outer box. This set up allows for soaking tests to be performed. An LVDT placed outside of the outer box was used to measure horizontal displacement. A load cell in contact with the inner box was used to measure the vertical load. Data was acquired using Labview® installed in a PC equipped with data acquisition card.

RCA samples were compacted at 22 °C. Soleimanbeigi and Edil (2015) suggested that compaction of RAP at elevated temperatures improves mechanical properties of RAP. To verify the effect of compaction temperature on interface properties of RAP-Geosynthetics, RAP samples were compacted at 22 °C, 35 °C and 50 °C. These tests were intended to evaluate the effects of variations in field compaction temperature on interface properties.

For preparation of specimens at each temperature, the RAP sample, pore water, and compaction equipment were all placed in a temperature-controlled environmental chamber for 24 h to achieve the target temperature (i.e., 22 °C, 35 °C, or 50 °C). After equilibrating at each target compaction temperature, specimens were removed from the chamber and immediately compacted into the shear box. Sample temperatures remained within ± 1 °C of the target temperature during the preparation process. For the target temperature of 22 °C, the specimen was compacted at w_{opt} and 95% of γ_{dmax} . For compaction at 22 °C, the number of blows per layer using a standard Proctor hammer was determined by trial and error to achieve the target density. The same compaction energy (blows per layer) was applied to specimens compacted at 35 °C and 50 °C to ensure that the compaction temperature was the only variable parameter.

The compacted RAP specimens at elevated temperatures were allowed to cool down to 22 °C over 8 h and the tests were performed at 22 °C thereafter under normal pressures of 50, 100 and 200 kPa. A displacement rate of 1 mm/min and the total test travel distance of 50 mm were employed, except when the total limit of 17 kN was reached or the geosynthetic ruptured.

3.2.3. Pull-out Test

Pull-out tests were performed on RCA and RAP samples reinforced with woven geotextile and uniaxial geogrid. Test procedures followed the ASTM D6706 standard using a large-scale pull-out box manufactured by GeoSyntec Consultants. The steel pull-out box was 1524-mm long, 609-mm wide, and 406-mm deep. Normal stress was applied by a rubber air bladder confined between the soil and three steel covers bolted to the top of the pull-out box.

Pull-out force was applied by two hydraulic jacks attached to the either side of the pull-out box. The hydraulic jacks were equipped with valves to control the pull-out rate. An AC hydraulic power unit and a compressed air pump provided power to the hydraulic jacks. The AC hydraulic power was equipped with a valve that could be used to change fluid flow direction, thus moving

the hydraulic jacks in a forward or backward motion. A compressed air unit applied constant load to the hydraulic jacks. A load cell mounted on the front of the pull-out box was used to measure pull-out force.

Extensometers were used to measure the displacement at the front of the pull-out box and along the length of the geosynthetics. The front LVDT was mounted on the head of the pull-out box and was used to measure displacement of the pull-out clamp. The back LVDTs were mounted in a rack outside of the box frame and used to measure displacements at three different points along the length of the geosynthetic.

The geosynthetic was attached to the pull-out clamps, which consisted of two 13-mm-thick metal plates bolted together with screws. Two thin metal sleeves were used to cover the plates to avoid interaction between the screws and the pull-out box during the test.

The aggregate sample was placed into the box and compacted with a hand tamper to 95% of γ_{dmax} . The bottom half of the machine was filled and the geosynthetic was placed on top of the material. The pull-out clamp that held the geosynthetic exited the box through the front opening and was bolted to a metal bar. The hydraulic jacks were connected to either side of the metal bar, which was in contact with the load cell.

The three telltales connecting each back LVDT entered the box through opening slots in the back and were connected to the geosynthetic body at 331.2, 628.7 and 920.8 mm for the woven geotextile, and 241.3, 711.2 and 1168.4 mm for geogrid (measured from the back of the pull-out box.) These telltales were protected by still rods that moved along with the geosynthetic during the pull-out test. The upper half of the box was then filled following the same procedures of compaction. A space of 38 mm was left between the backfill and the top of the machine to accommodate the air bladder.

The air bladder was placed on top of the backfill and the covers were bolted into place. A hole in one of the cover plates allowed access to the nipple of the air bladder. Compressed air was pumped into the bladder until the target normal stress was reached. All pull-out tests were performed at 20, 30, 50, 100 and 200 kPa normal stresses. A pull-out displacement rate of 1.0 mm/minute was used. Tests ran for 100 mm or until failure of the geosynthetics occurred. The pull-out test equipment is shown in Figure 3.6.

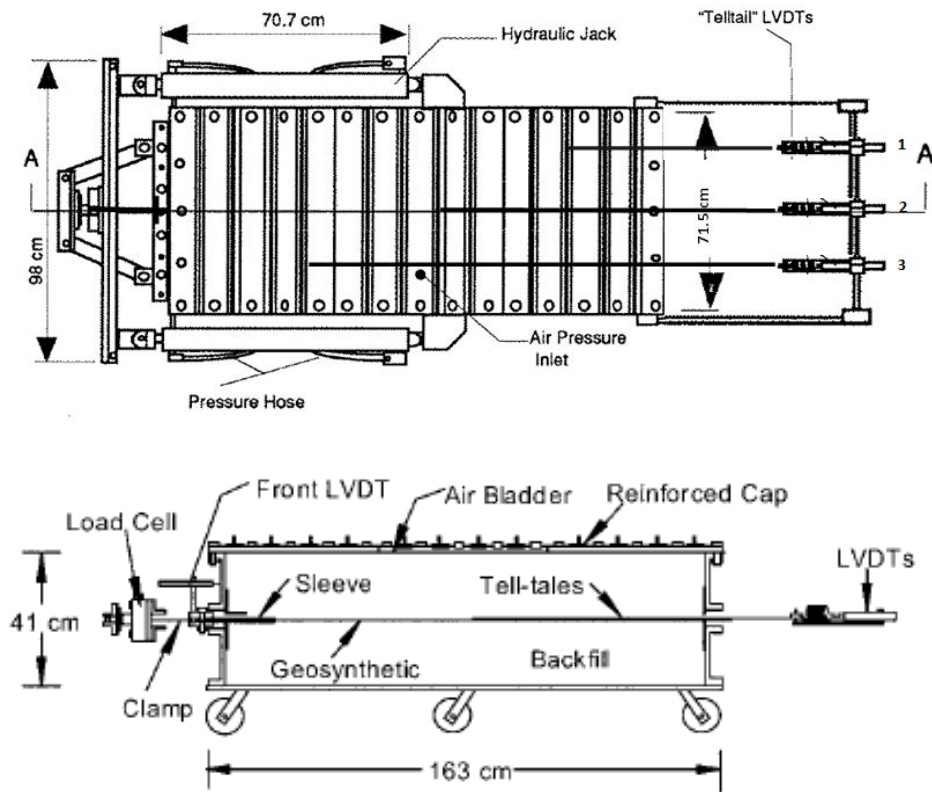


Figure 3.6. Schematic figures of the pull-out box apparatus. Top view (upper figure) and side view (lower figure) (adopted from Tatlisoz et al. 1998)

3.2.4. Temperature-Controlled Creep Tests

Unlike conventional materials, the asphalt binder coating on RAP particles increases the material's compressibility, and may lead to excessive long-term deformations under sustained deviator stresses present in embankments and retained fills (Viyanant et al. 2007; Soleimanbeigi et al. 2015). Creep for soils and aggregate materials is the accumulation of time-dependent shear strain under a sustained shear stress that is controlled by the viscosity of the material structure (Mitchell and Soga 2005). Evaluation of creep behavior is important in design of structural fills to quantify long-term deformations and to assess potential failure due to excessive strain or rupture. Viyanant et al. (2007) conducted laboratory experiments to evaluate creep response of compacted RAP at room temperature and concluded that the material is susceptible to excessive strain and rupture under shear stresses typical in structural fills. It was suggested that applied shear stresses in construction applications involving beneficial use of RAP be limited to minimize these effects. Since the viscosity of asphalt binder is temperature-sensitive (Roberts et al. 1996; ASTM D2493), temperature changes expected in field applications may also affect the creep characteristics and performance of RAP as an alternative construction material. In previous work, Soleimanbeigi and Edil (2015) reported results from laboratory tests showing that higher temperatures (35 °C) increased the compressibility of RAP and other materials containing asphalt binder (e.g., recycled asphalt shingles).

Creep tests at elevated temperatures were conducted in a conventional triaxial cell equipped with a heating and cooling system that maintained a constant temperature between 5 °C and 35 °C. The selected temperature system range represents the typical field temperature in the contiguous US (Soleimanbeigi 2012). A schematic of the system is shown in Figure 3.7. A coil of copper tubing (6-mm outside diameter) was wound around the specimen to circulate heated or cooled water. A 30-mm separation distance was maintained between the copper coil and the specimen to avoid contact during shearing. Test temperatures above room temperature were obtained by circulating warm water in the coil using a pump placed outside of a heating water bath. Tygon tubing was used to connect the pump to the coil to minimize temperature loss during water circulation. Temperatures in the bath (T_b), in the cell chamber (T_c), and inside the specimen (T_s) were measured using three type-K thermocouples. A LabView program was used to control heating in the bath so that the temperature of the test specimen could be maintained within ± 0.5 °C of the target temperature. Temperatures less than room temperature were obtained by circulating water from a cooling bath (PVC box filled with ice in equilibrium with water). The flow rate from the pump was controlled by a program written in LabView so that the temperature of the specimen was maintained within ± 0.5 °C of the target temperature. To avoid disturbance due to insertion of a thermocouple into the specimen, a correlation was determined from the initial tests to estimate T_s from T_c . The required time to bring the T_s to the target temperature was approximately 100 min.

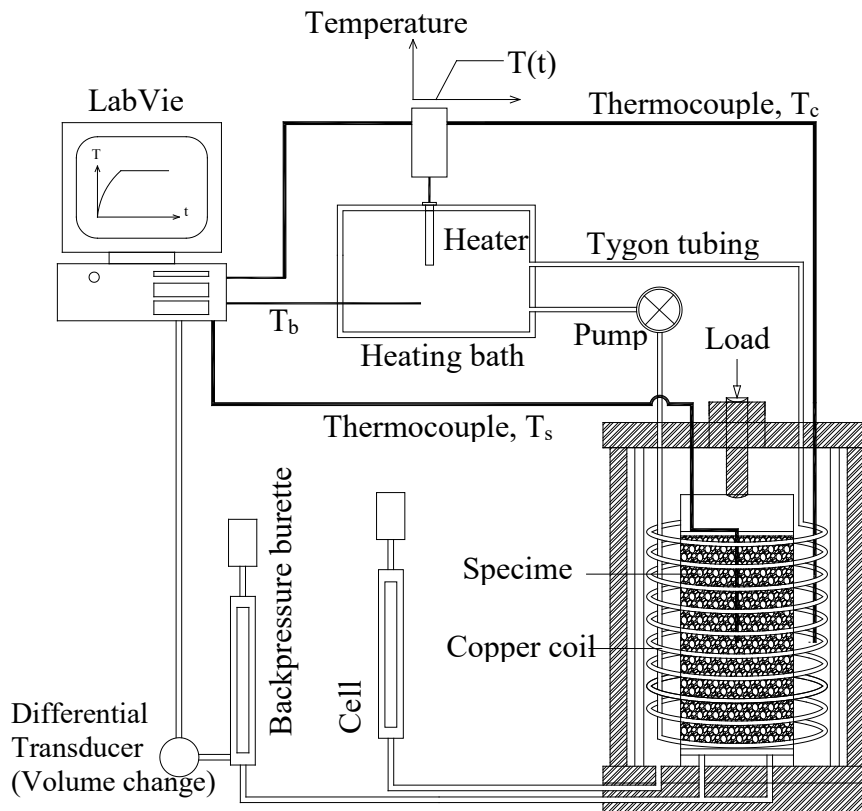


Figure 3.7. Schematic of temperature-controlled triaxial creep system

Table 3.4 summarizes the laboratory testing program for creep. Triaxial compression tests included a suite of consolidated drained (CD) compression tests for RAP specimens initially compacted and consolidated at three controlled temperatures (i.e., 22 °C, 35 °C, and 50 °C). For preparation of specimens at each temperature, the RAP sample, pore water, and compaction equipment were all placed in a temperature-controlled environmental chamber for 24 h to achieve the target temperature (i.e., 22 °C, 35 °C, or 50 °C). A thermometer placed in the RAP sample also verified achievement of the target temperature inside the sample. After equilibrating at each target compaction temperature, specimens were removed from the chamber and immediately compacted in three layers in a split cylindrical mold (71-mm inside diameter, 142-mm height). Sample temperatures remained within ± 1 °C of the target temperature during the preparation process. For the target temperature of 22 °C, the specimen was compacted at w_{opt} and 95% of $\gamma_{\delta_{max}}$. For compaction at 22 °C, the number of blows per layer using a standard Proctor hammer was determined by trial and error to achieve the target density. The same compaction energy (blows per layer) was applied to specimens compacted at 35 °C and 50 °C to ensure that the compaction temperature was the only variable parameter.

Table 3.4. Summary of triaxial compression and deviatoric creep tests.

Test	Compaction and Consolidation Temperature (°C)	Test Temperature (°C)	σ'_3 (kPa)	\bar{D}
Triaxial compression	22	22	35, 70, 140	-
	35	22	70	-
	50	22	70	-
Deviatoric creep	22	22	70	0.40, 0.60, 0.80, 0.85, 0.90, 0.95
	35	22	70	0.95
	50	22	70	0.95
	22	35	70	0.95
	22	50	70	0.95

Note: σ'_3 = confining pressure, and \bar{D} =stress level.

Consolidated drained (CD) triaxial compression tests were conducted in a temperature-controlled triaxial compression cell (Soleimanbeigi et al., 2015) to evaluate shear strength and volume change behavior of the compacted RAP specimens. Compacted RAP specimens were initially backpressure-saturated (ASTM D4767) until a B-value greater than 95% was attained and then consolidated at effective isotropic confining stresses of $\sigma'_3=35$ kPa, 70 kPa, or 140 kPa for at

least 24 h. Temperature during consolidation was maintained at the same temperature as controlled specimen compaction. Specimen volume changes during consolidation were measured from effluent water volume monitored using a pipette in the backpressure line. The effective consolidation stresses were selected by considering typical highway embankment heights (1-5 m) (Wright, 1996) and the unit weight of the compacted RAP. After consolidation was complete, specimens were sheared at an axial strain rate of 3.0 %/h. This strain rate was considered appropriate to maintain a drained condition based on comparison with similar soils and from calculations based on pore water expulsion measured during the consolidation stage. The specimens compacted at elevated temperatures (i.e. 35 °C and 50 °C) were consolidated inside the cell at $\sigma'_3=70$ kPa for 24 h at the same temperature, while the volume change was measured from the water elevation in the backpressure burette. The time required to reduce the specimen temperature in these cases was 200 min, as obtained from calibration of the temperature-controlled triaxial cell.

Compaction and consolidation procedures for specimens subject to deviatoric creep tests were similar to those described above for triaxial compression tests. All specimens were consolidated at $\sigma'_3=70$ kPa. One series of creep tests was conducted for specimens compacted and consolidated at 22 °C, 35 °C, and 50 °C, and then subject to deviatoric creep at 22 °C (Table 3.3). Two additional tests were conducted for specimens compacted and consolidated at 22 °C, and then subject to deviatoric creep at 35 °C and 50 °C, respectively. Creep tests for specimens compacted, consolidated, and sheared at 22 °C were conducted at stress levels (\bar{D}) ranging from 0.40 to 0.95 (Table 3.3), where $\bar{D} = \sigma_d/\sigma_{df}$ is the ratio of the applied principal stress difference (σ_d) to the principal stress difference at failure (σ_{df}). Creep tests at elevated temperatures were conducted at a high stress level ($\bar{D}=0.95$) to make sure the specimens are ruptured and the time to creep ruptures are compared at different temperatures. Deviator stress (σ_d) in each case was gradually increased at a loading rate of 0.2 mm/min until the target stress level was attained. Axial deformation of the specimens at sustained deviator stress was measured over a time period of at least one week or until the specimen failed, whichever occurred first. Volume changes were also monitored from the water elevation in the graduated backpressure burette. Specimen temperatures during the creep tests were maintained within a tolerance of ± 1 °C to the target temperature.

3.2.5. Long-Term Filtration and Pore Size Tests

Long-term filtration tests were conducted using the gradient ratio test (GRT) method standardized by ASTM D5101 to determine the filtration performance of RCA with two different geotextiles. As mentioned in the ASTM D5101, the test apparatus consists of a rigid wall permeameter, inflow constant head device, outflow constant head device, and a manometer board. Manometer ports in the permeameter are necessary to measure the total heads at various locations in a specimen (Figure 3.8).

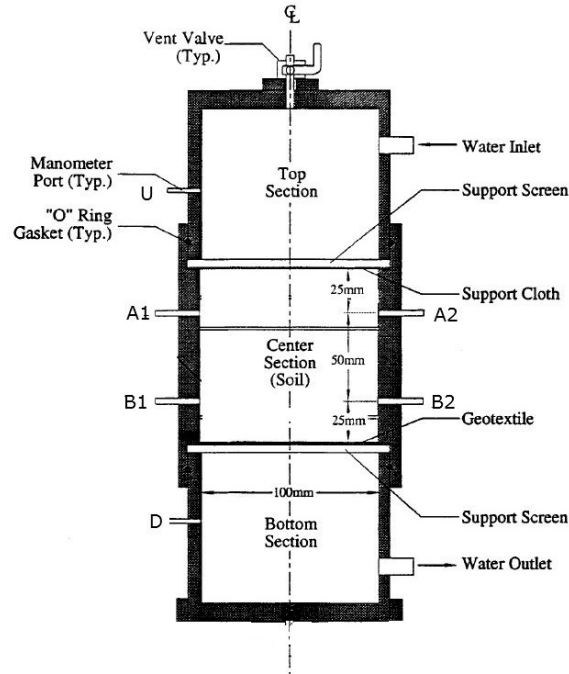


Figure 3.8. Schematic setup of gradient ratio test chamber (modified after Fischer et al., 1999)

Contrary to the 24-hour procedure prescribed in D 5101, the tests in this study were continued for more than 3 months to understand the long-term clogging performance of the geotextile/RCA systems. Hydraulic gradients of 1, 2.5, and 5 were used in the tests. Kutay and Aydilek (2005) showed that potentially biological growth might occur due to presence of microorganisms in the tap water, which decrease the hydraulic conductivities and lead to erroneous measurements. To prevent this, influent water was regularly treated with slowly dissolving chlorine tablets.

As previously discussed by Aydilek and Edil (2002), the evaluation of the reduction in flow capacity of the geotextile system was evaluated based on the permeability ratio (K_R) determined during the gradient ratio tests. K_R is defined as the ratio of the stabilized hydraulic conductivity of the soil to the stabilized system (soil-geotextile) hydraulic conductivity:

$$K_R = \frac{k_{soil}}{k_{system}} \quad (3.2)$$

where k_{soil} and k_{system} are the hydraulic conductivities in the soil and the entire system, respectively. The hydraulic conductivity of the entire system, k_{system} , is determined using the applied hydraulic gradient on the soil-geotextile system (i.e., 1, 2.5, and 5). For k_{soil} calculations, i_{soil} values were calculated using the readings registered by manometers located 25 mm and 75 mm from the top of the middle section of the permeameter. For both of the hydraulic conductivities (i.e., k_{soil} and k_{system}) stabilized flow rates were used (determined by taking the average of the last five stabilized values for each test).

Upon termination of the gradient ratio tests, geotextile samples were subjected to permittivity tests and digital image analyses in order to quantify the changes in their hydraulic performance

and pore structures, respectively. Any soil remaining on the surface of the geotextile was removed by lightly brushing. The permittivity tests were conducted following the procedures outlined in ASTM D4491. Extensive specimen preparation was necessary before imaging the nonwoven geotextiles, as the three-dimensional structure of these geotextiles causes difficulties in capturing pore structures from two-dimensional images, and planar and cross-sectional thin-sections need to be prepared to provide detailed information on clogging. The thin sections of the nonwoven geotextiles investigated in this study were prepared following the procedures summarized by Aydilek et al. (2002). The information extracted from these thin sections were utilized to calculate the changes in geotextile characteristic pore opening sizes (e.g., O_{95} , O_{60} , O_{50} , O_{40} , O_{30} , O_{15} , and O_{10}) to better quantify clogging. The thin sectioning process involved planar sections as well as sections normal to the plane of the geotextile; the latter ones are termed cross-sections. From each post-GRT nonwoven geotextile, 2-4 specimens were cut, and from each specimen, 3 cross-sections and 1-2 planar sections were prepared. The preparation of thin sections required a series of sequential steps: epoxy-resin impregnation, cutting, grinding, lapping and polishing (Aydilek et al. 2002). The polished specimens were then analyzed under a low magnification light microscope to ensure that a smooth and clean surface was obtained for image analyses.

Pore structure images of the all geotextiles were captured using an optical light microscope. The microscope had a 45 mm x 25 mm workstation platform, and a 2.5 to 100X macro zoom lens coupled with an image-capturing software. A digital camera was attached to the microscope that sent the captured images to the software. Resolutions of 1298 by 968 pixels were used for all images. Magnification (objective) ratio was 2.5X and 2.5-5X, and the corresponding pixel size was approximately 6.97 mm and 3.25-6.9 mm for the planar and cross-sections, respectively. The specimens were illuminated from the bottom as suggested by Jang et al. (1999) and Aydilek et al. (2002).

ImageJ, a public domain, Java-based image processing program, which was developed at the National Institutes of Health and commonly used in various engineering applications (Schneider et al. 2012), was utilized to analyze the images. The threshold value for generating a binary image and differentiating the background from the image objects of interest was set to the mid-point of the pixel intensity values recorded at the two ends of the histogram, and ranged from 158 to 225. After thresholding, binary images were obtained in which white and black regions had pixel intensity values of 1 and 0, respectively. After recognition of the fibers and pores in the slice, porosities (n) and the pore opening size distributions of each individual planar and cross-sectional images were calculated. In the binary image, the white and black pixels corresponded to pore openings and fibers, respectively. The pore openings were counted and the ratio of the number of openings to the whole image size was referred to as porosity. For pore size distribution (PSD) calculations, a range of geotextile opening diameters (i.e., comparable to the sieve sizes commonly used in ASTM D4751 dry sieving test) was defined. Each opening diameter was compared to the diameter of a circle fitted to the pore, and percentage of geotextile pore sizes smaller than the defined opening diameters were calculated. The process was repeated for the images of all samples of a particular geotextile, and an average PSD was reported. The details of the procedure are provided in Aydilek et al. (2002).

4. RESULTS

Results from index, mechanical, and hydraulic property tests are presented in this chapter. Index properties include grain size distribution, specific gravity, and absorption. Mechanical properties include compaction characteristics, shear strength, interface shear strength and pull-out resistance between RCA, RAP and the selected geosynthetic reinforcements. Hydraulic property tests include hydraulic conductivity and gradient ratio tests.

4.1. Index Properties

4.1.1. Grain Size Distribution and Gradations Indices

Figure 4.1 shows the grain size distributions of RCA and RAP samples. Table 4.1 summarizes the gradation indices. According to the Unified Soil Classification System (USCS), RCA used for hydraulic tests is classified as Well Graded Sand – Silty Sand (GW-SM) with approximately 7.7% of fine particles. RCA used for all other tests is classified as Poorly Graded Gravel (GP) with approximately 8.7% of fine particles. RAP is classified as a Poorly Graded Sand (SP) with approximately 5.1% of fine particles. The USCS classifications of both materials, presented in this study, compares well with the soil classifications for typical RCA and RAP reported in the literature (Table 1.1).

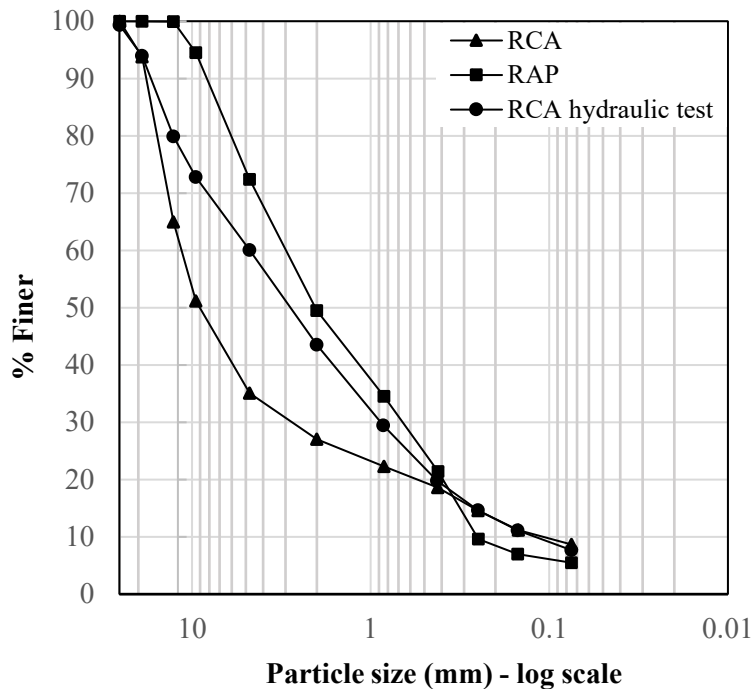


Figure 4.1. Grain size distribution of RCA and RAP

Table 4.1. Soil Classification and Gradation Indices for RCA and RAP.

	USCS classification	Fines (%)	D₁₀ (mm)	D₃₀ (mm)	D₅₀ (mm)	D₆₀ (mm)	C_u	C_c
RCA ^a	SW-SM	7.7	0.12	0.85	2.8	4.7	39.17	1.28
RCA ^b	GP	8.7	0.11	2.90	9.0	10.7	97.27	7.145
RAP	SP	5.1	0.25	0.65	2.0	3.0	12.00	0.563

Note: (a) RCA sample for hydraulic tests, and (b) sample used for all other tests.

4.1.2. Specific Gravity and Absorption

The specific gravity values obtained for RCA (i.e. 2.56 and 2.79) are comparable to the values reported in the literature (2.24 to 2.72). The mortar content of RCA was measured at 35.7%, which is comparable to the lower end of the values surveyed in the literature. The specific gravity of RAP sample in this study (2.39) is also within the range reported in the literature (2.20 to 2.56) (Rathje et al. 2006, FHWA 2008, Benson et al. 2012) (Table 1.1). The lower specific gravity values of RAP and RCA compared to those of natural aggregates may be attributed to presence of mortar in RCA, and asphalt binder in RAP, which have specific gravities of 2.1 and 1.0, respectively (Table 1.1). This is not a confirmed conclusion but is a potential reason for the observation.

The measured absorptions of RCA and RAP are 4.3% and 2.6% respectively. The absorption of RCA measured in this study are comparable to the lowest values found in the literature (5.0% to 6.5%), while the absorption values of RAP are close to the highest values found in the literature (0.6% to 2.0%), as presented in Table 1.1.

4.1.3. Compaction Characteristics

Figures 4.2(a, b) shows the compaction curves for RCA and RAP samples along with their zero air void (ZAV) curves. ZAV curves indicate complete saturation of each sample. RCA and RAP samples show well-defined compaction curves, which indicate their moisture sensitivity during compaction. The compaction curve of RCA suggests that the material is sensitive to moisture, as indicated by the presence of a distinctive peak in dry unit weight. This behavior is atypical of gravelly soils, which generally are not significantly sensitive to water content. The maximum dry unit weight (γ_{dmax}) of 19.3 kN/m³ for RCA was attained for both RCA samples but the RCA sample used for mechanical tests had optimum water content (w_{opt}) of 10.0% and the one for the hydraulic tests had w_{opt} of 14.5%. Again the difference between the optimum moisture contents may be related to the differences in mortar content within RCA. As illustrated in Figure 4.2(a), γ_{dmax} occurs close to the ZAV curve.

The compaction curve of RAP peaks with γ_{dmax} of 18.6 kN/m³ at w_{opt} of 4.2%. Lower absorption of RAP compared to RCA reduces the w_{opt} . Accumulation of water on the surface of specimens during compaction was observed at water contents higher than 6.0%. Loss of water through the bottom of the compaction mold occurred in samples with water content higher than 7.0%.

Table 4.2 summarizes the measured index and compaction properties of RCA and RAP samples obtained in this study along with the corresponding range of each parameter reported in the literature.

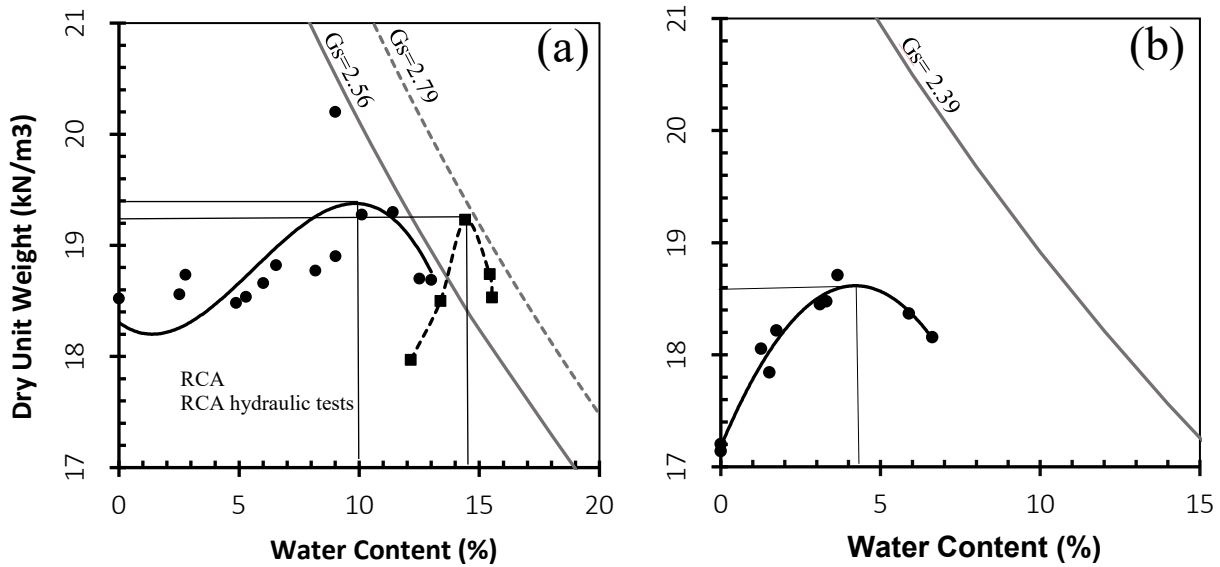


Figure 4.2. Compaction curve of RCA (a) and RAP (b).

Table 4.2. Index Properties of RCA and RAP Compared to Values Observed in the Literature.

	RCA measured	RCA literature	RAP measured	RAP literature
USCS	GP	GW, GP, SW, SP, SC	SP	GW, SW, SP
Fine Content (%)	8.70	3.2 - 12.8	5.10	0.6 - 3.0
Mortar/Asphalt (%)	35.7	37.0 – 65.0	5.84	3.5 - 7.1
Absorption (%)	4.34	5.0 - 6.5	2.58	0.6 - 2.0
Specific Gravity, G_s	2.56	2.24 - 2.72	2.39	2.20 - 2.56
$\gamma_{d,max}$ (kN/m ³)	19.3	17.5 - 19.2	18.6	13.9 - 19.4
w_{opt} (%)	10.0	8.7 - 11.9	4.0	5.2 - 8.8

Note: USCS = United Soil Classification System, AASHTO = American Association of State Highway and Transportation Officials (soil classification system). Mortar content for RCA, asphalt content for RAP. G_s = specific gravity; $\gamma_{d,max}$ = maximum dry unit weight, and w_{opt} = optimum water content.

4.2. Large Scale Triaxial Test

Mohr-Coulomb failure envelopes were constructed from shear testing results obtained using large scale consolidated drained (CD) triaxial tests conducted on specimens of RCA and RAP. An area correction was performed to obtain corrected values of deviator stress during analysis. Results were plotted in terms of deviator stress (σ_d) versus axial strain (ϵ_a). Failure was defined at the maximum value of deviator stress (σ_{max}) or σ_d at 15% axial strain, whichever was reached first. Mohr circles were plotted at failure points to determine shear strengths of the RCA and RAP specimens. Best fit Mohr-Coulomb failure envelopes were constructed for each material.

4.2.1. RCA

The stress-strain curves for RCA specimens and the Mohr-Coulomb failure envelope are displayed in Figures 4.3 and 4.4, respectively. The effective friction angle (ϕ') of 48° and apparent cohesion intercept (c') of 78 kPa were attained from the failure envelope. The ϕ' of 48° is within the range reported in the literature (41° - 65°) as summarized in Table 1.1. The c' of 78 kPa is significantly lower than the value presented by Rathje et al (2006) of 151 kPa, but is close to the range reported in the literature (0 kPa to 55 kPa). The occurrence of a non-zero c' in RCA specimens may be due to the re-cementation of remaining unhydrated cement paste in the material.

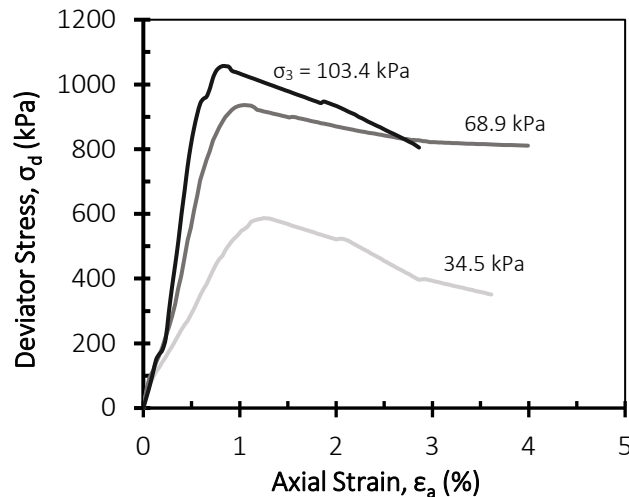


Figure 4.3. Stress-strain curves for RCA specimens from CD triaxial compression tests

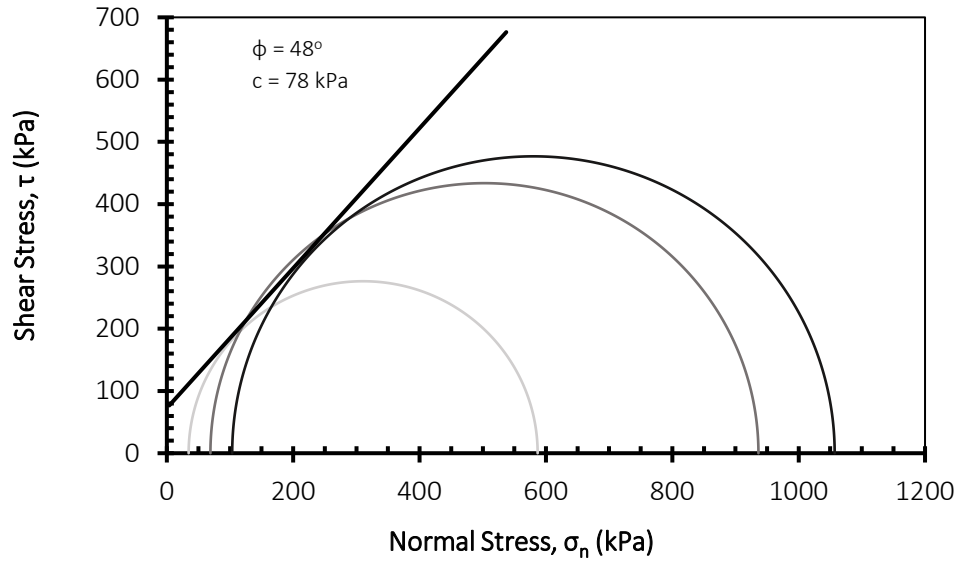


Figure 4.4. RCA Mohr-Coulomb failure envelope

All RCA specimens reached peak deviator stresses at less than 2.0% axial strain before reaching residual conditions. Strain softening behavior was observed at all three confining pressures. All specimens exhibited a typical failure plane as expected for low compressible materials (Figure 4.5).



Figure 4.5. Failure plane for RCA specimens

4.2.2. RAP

Results of CD triaxial compression tests on RAP specimens and the Mohr-Coulomb failure envelope are shown in Figures 4.6 and 4.7, respectively. The ϕ' of 29° and the c' of 25 kPa were attained from the tests. The stress-strain curves of RAP specimens exhibit peak points at relatively large axial strains compared to RCA specimens. The larger axial strain is attributed to asphalt binder coating at the contact surfaces of RAP particles, which increase the shear strain at a given applied shear stress. A distinct failure plane was not observed in the RAP specimens during test. Rather, all specimens bulged axially near their mid-height during compression, as depicted in Figure 4.8. Similar behavior was reported by Rathje et al. (2006) and Soleimanbeigi and Edil (2015) for RAP specimens and by Soleimanbeigi et al. (2014) for RAS specimens. This behavior is typical of loose or compressible materials under drained triaxial loading. The friction angle of 29° for RAP acquired in this study is lower than the values reported in the literature (39° to 44°). The c' of 25 kPa observed in RAP is within the mid-range of values reported in the literature (0 to 55 kPa). The apparent cohesion intercept for RAP is likely the result of bonding of RAP particles due to asphalt binder coatings. Table 4.3 summarizes friction angles of different natural and recycled backfill aggregates reported in the literature as well as those obtained in this study.

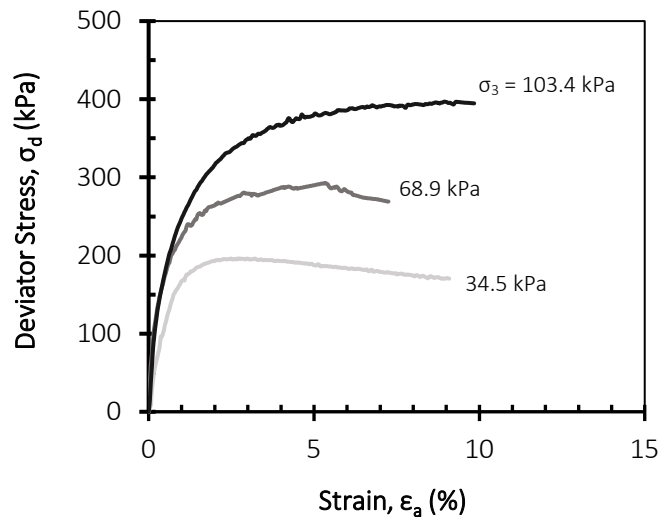


Figure 4.6. RAP drained large-scale triaxial test curves at different confining pressures

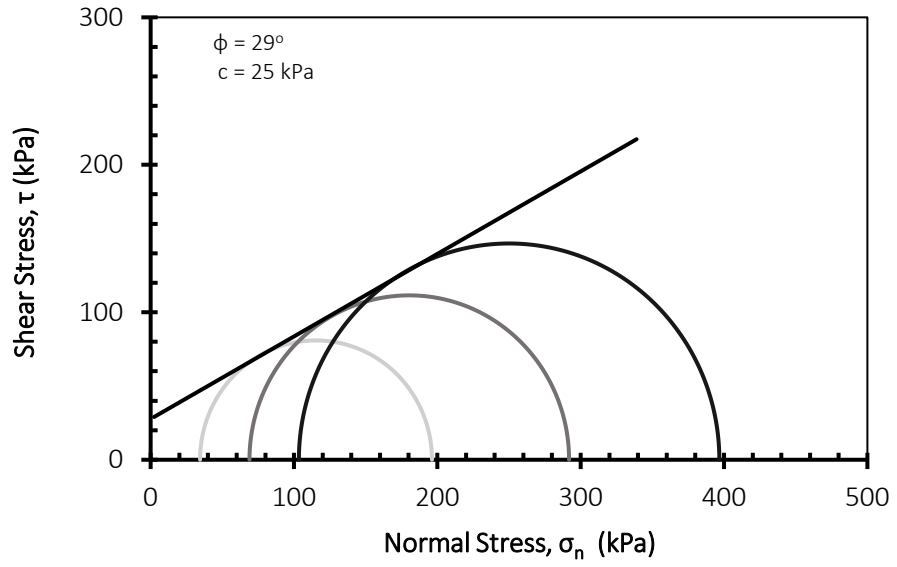


Figure 4.7. RAP Mohr-Coulomb failure envelope



Figure 4.8. Axial bulging deformation in RAP specimen

Table 4.3. Friction Angles of Different Natural and Recycled Backfill Aggregates Reported in the Literature

Soil Type	Range of soil friction angles (ϕ')	References
Sand	34.7 - 37.5	Hsieh et al. (2011), Nejad et al. (2012)
Gravel	38.4 - 45.9	Hsieh et al. (2011), Nejad et al. (2012)
Crushed stone	55.0	Hsieh et al. (2011)
RCA	41.0 – 65.0	Rathje et al. (2006), Arulrajah et al. (2013), Soleimanbeigi et al. (2015)
RCA	48.0	This study
RAP	37.0 – 45.0	Rathje et al. (2006), Arulrajah et al. (2013), Soleimanbeigi et al. (2015)
RAP	29.0	This study
FDS	31.0 – 44.0	Goodhue et al. (2001), Soleimanbeigi et al. (2015)

4.3. Large Scale Interface Direct Shear Test Results

4.3.1. RCA

Results of large-scale interface direct shear tests between RCA and the four selected geosynthetic reinforcements (i.e. woven geotextile, non-woven needle-punched geotextile, uniaxial geogrid, and biaxial geogrid), and their respective Mohr-Coulomb failure envelopes are displayed in Figure 4.9. Interface friction angles (δ) between RCA and geosynthetic reinforcements as well as other interface materials reported in the literature are summarized in Table 4.4.

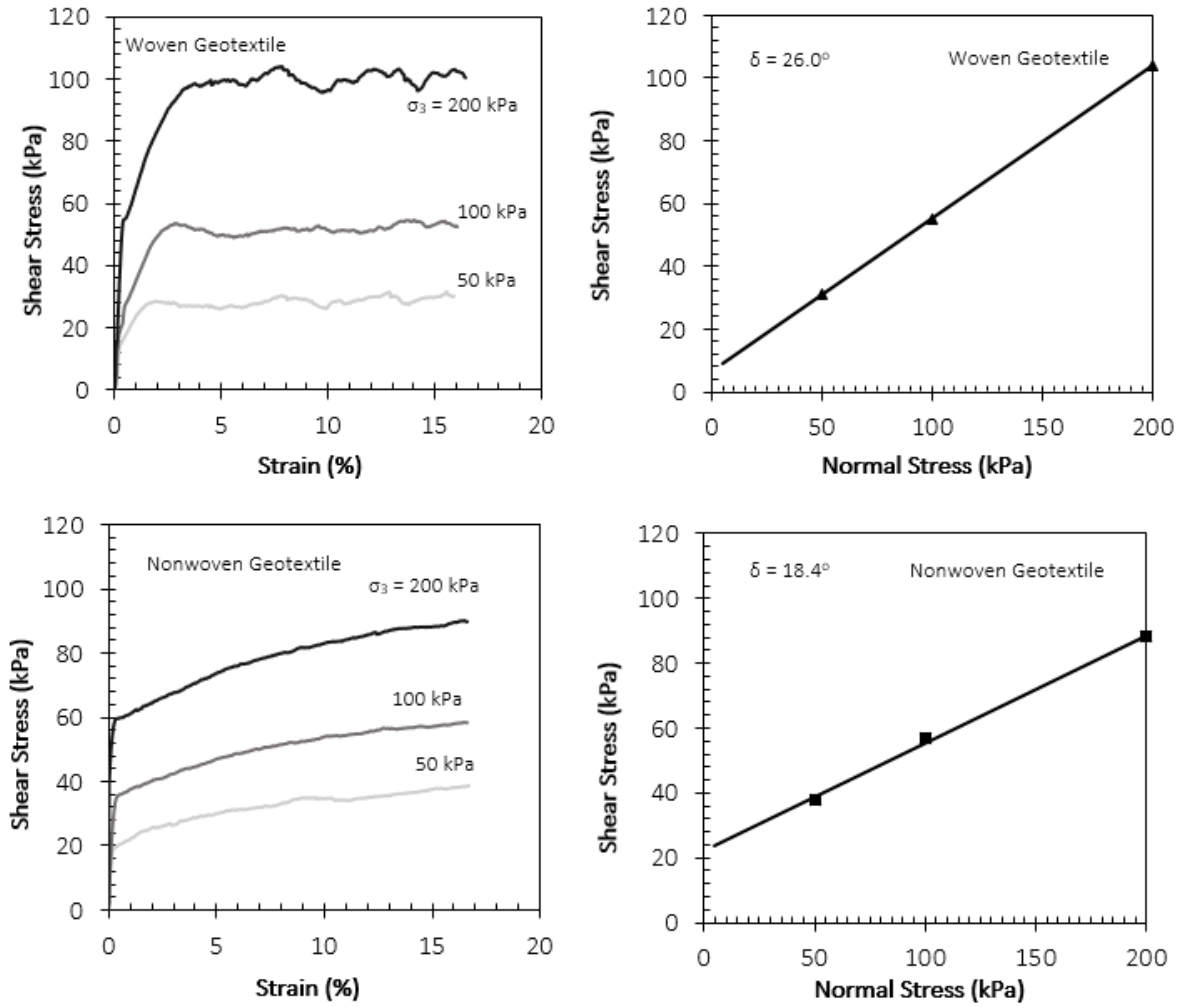


Figure 4.9. Interface direct shear results for RCA-Geosynthetic interaction, and respective Mohr-Coulomb failure criteria

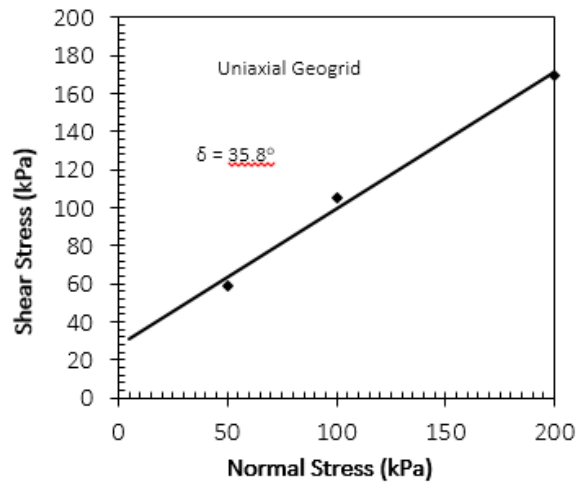
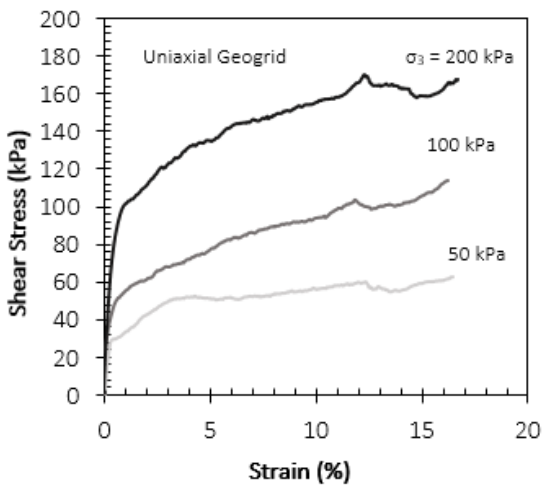
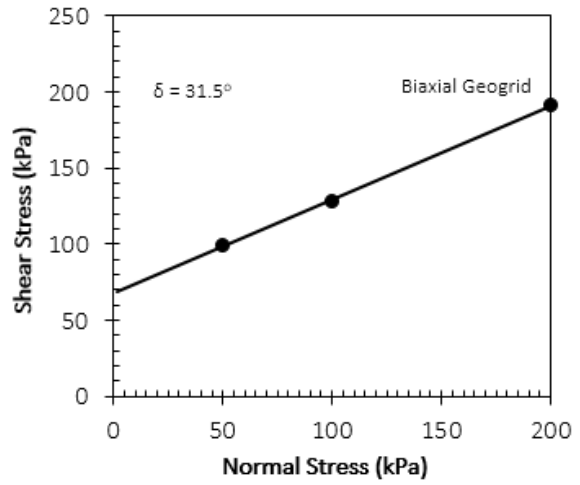
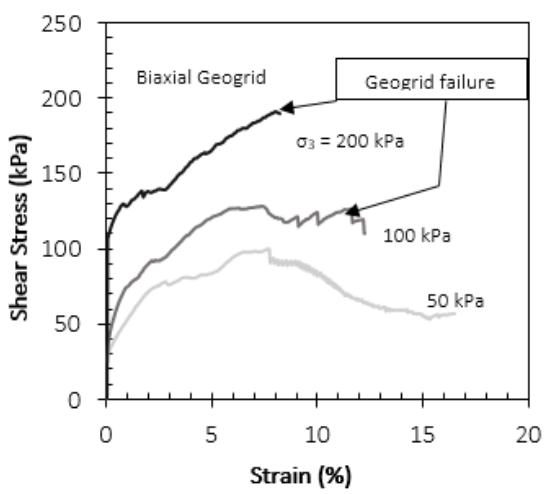


Figure 4.9 (continued). Interface direct shear results for RCA-Geosynthetic interaction, and respective Mohr-Coulomb failure criteria

Table 4.4. Interface friction angles and efficiency factors for different interface materials.

Interface type	Source	Interface friction angle (δ)	Efficiency factor (E_ϕ)
RCA-Woven geotextile	This study	26.0	0.41
Gravel	Hsieh et al. (2011)	26.9	0.64
Crushed Stone	Hsieh et al. (2011)	30.6	0.41
Sand	Hsieh et al. (2011)	35.3	0.92
FDS	Goodhue et al. (2001)	29.0	0.26-0.32
RCA-Nonwoven geotextile	This study	18.4	0.30
RCA-Uniaxial geogrid	This study	35.8	0.62
Gravel	Nejad et al. (2012)	44.4	0.95
Sand	Nejad et al. (2012)	33.8	0.97
FDS	Goodhue et al. (2001)	26.0-31.0	0.80-0.60
RCA-Biaxial geogrid	This study	31.5	0.55
RCA	Arulrajah et al. (2013)	50.0	0.55
Gravel	Hsieh et al. (2011)	38.7	1.01
Crushed Stone	Hsieh et al. (2011)	43.4	0.66
Sand	Hsieh et al. (2011)	37.0	0.98

Because information on interface friction angle between RCA and geosynthetics is scarce, interface properties of different soil-geosynthetics were used for comparison. The δ of RCA-woven geotextile is close to the range reported for gravel-woven geotextile and FSD-woven geotextile (27.0°-29.0 °). However, the efficiency factor (E_ϕ) is noticeably lower than those for Gravel-woven geotextile (0.64) or Sand-woven geotextile reported by Hsieh et al. (2011) and FSD-woven geotextile (0.60-0.90), reported by Goodhue et al. 2001.

The δ for RCA-nonwoven geotextile yielded an unexpected lower value of 18.7°, when compared to rounded sand- nonwoven geotextile (26.0 °), and concrete sand- nonwoven geotextile (30.0 °) reported by Korner (2005). The E_ϕ was also considerably lower (0.30), when compared to sand (0.92 to 1.00). Excessive tensional deformation was observed along the length of the extruded geotextile, near the clamp attachments. Deformation was also significant at the clamp attachments, where the geotextile was fixed to the lower box (Figure 4.10).

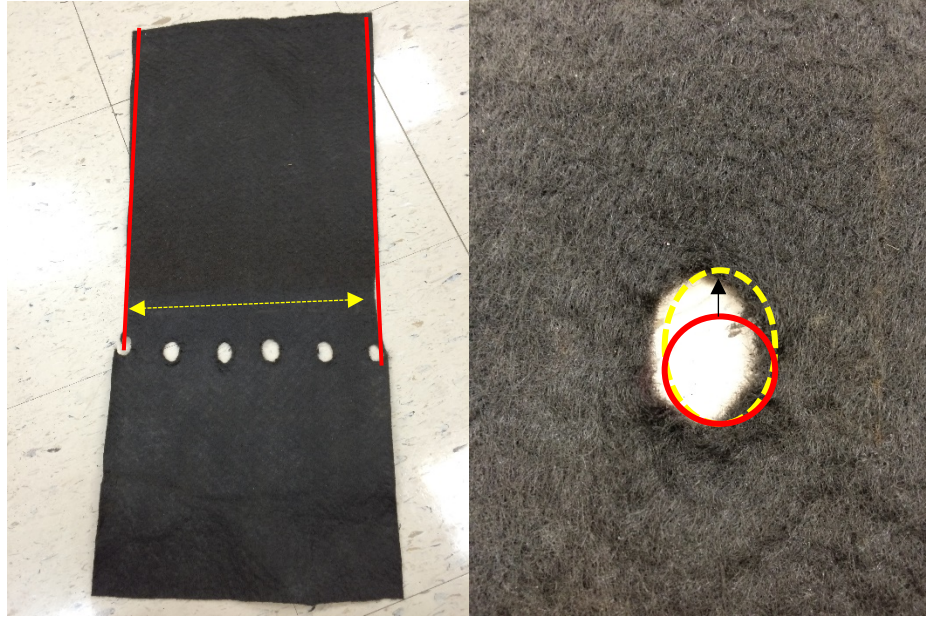


Figure 4.10. Extensive tensional deformation of the nonwoven geotextile at the cross-section (left), and at the clamp connection (right).

The RCA-uniaxial geogrid has the largest values of δ (36°) and E_ϕ (0.62). The δ of RCA-uniaxial geogrid observed in this study is comparable to δ of FDS-uniaxial geogrid (31.0°) and sand-uniaxial geogrid (33.8°), reported by Nejad et al. (2012), and Goodhue et al (2001). Nejad et al. (2011) reported δ of 44.0° between gravel-uniaxial geogrid.

Biaxial geogrid was tested in XM direction due to the larger tensile strength of the reinforcement in this direction. The δ value of 31.5° was observed, representing E_ϕ of 55.0%. Arulrajah et al (2013) reported δ of 50.0° between RCA and a similar biaxial geogrid, with an equivalent E_ϕ of 55.0%. Other coarser materials, such as sand, gravel, and crushed stone, exhibited δ ranging from 37.0° to 43.3° (Hsieh et al. 2011).

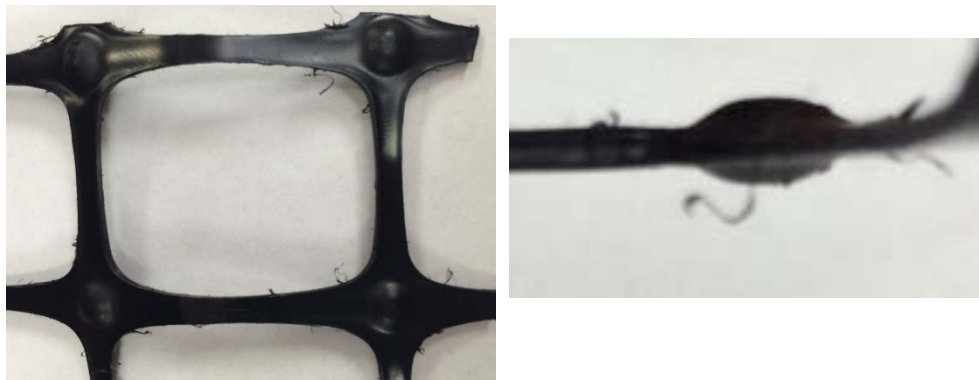


Figure 4.11. Extension of the width (left), and height (right) of the nodes located at each aperture corners of the biaxial geogrid.

4.3.2. RAP

RAP samples were compacted at 22 °C, 35 °C, and 50 °C, and interface direct shear tests were conducted at room temperature (i.e. 22 °C). Results of large scale interface direct shear tests between RAP and the four selected geosynthetic reinforcements, and their respective Mohr-Coulomb failure envelopes are displayed in Figure 4.12. A summary of the δ values at the target temperatures is provided in Table 4.5.

The δ and E_ϕ between RAP and woven geotextile are comparable to values of concrete sand-woven geotextile (26.0° at 22 °C) (Koerner 2005), but slightly lower than that of gravel-woven geotextile and FDS- woven geotextile (27.0° - 29.0°) (Goodhue et al. 2001). The E_ϕ however is noticeably higher for RAP- woven geotextile (0.82) when compared to gravel-woven geotextile and FDS-woven geotextile values of 0.60 (Goodhue et al. 2001) and 0.64 (Hsieh et al. 2011), respectively.

Compaction temperature does not have a consistent effect on δ . Increasing compaction temperature decreased the interface friction angle for RAP-Woven geotextile and RAP-Biaxial geogrid but increased δ for RAP-Nonwoven geotextile and RAP-Uniaxial geogrid at compaction temperature of 35°C. This was followed by a decrease in δ when the compaction temperature increased to 50°C.

RAP-Nonwoven geotextile yielded low δ (17.3° to 20.4°), when compared to rounded sand-Nonwoven geotextile (26.0 °), and concrete sand-Nonwoven geotextile (30.0 °) reported by Korner (2005). The E_ϕ ranged between 0.56 and 0.67, which is significantly lower than that of concrete sand-Nonwoven geotextile (0.84). The δ between RAP-Nonwoven geotextile increased when the compaction temperature increased from 22 °C to 35 °C, but decreased when temperature increased further to 50° C.

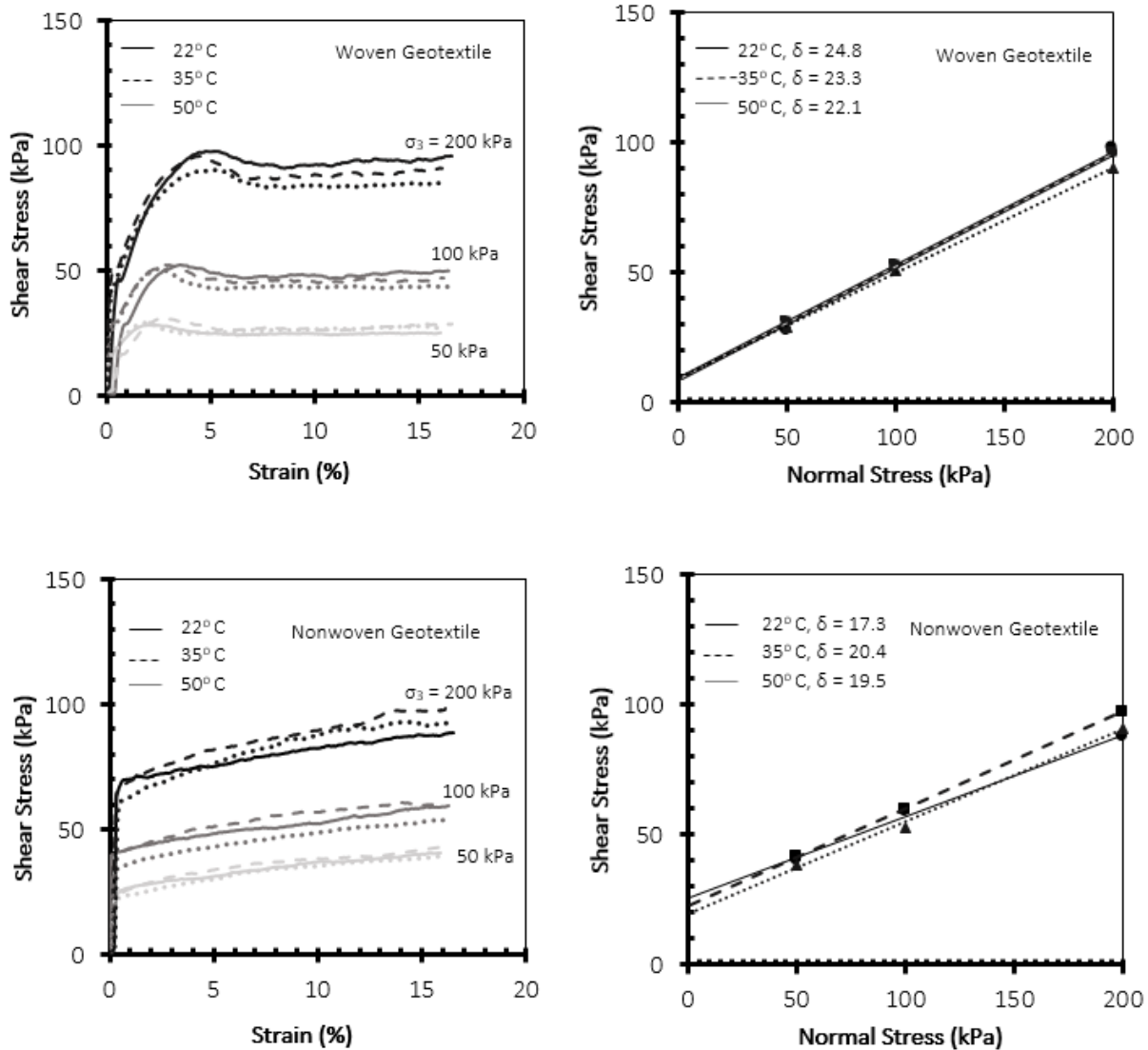


Figure 4.12. Interface direct shear test results for RAP-geosynthetic interaction and Mohr-Coulomb failure envelopes.

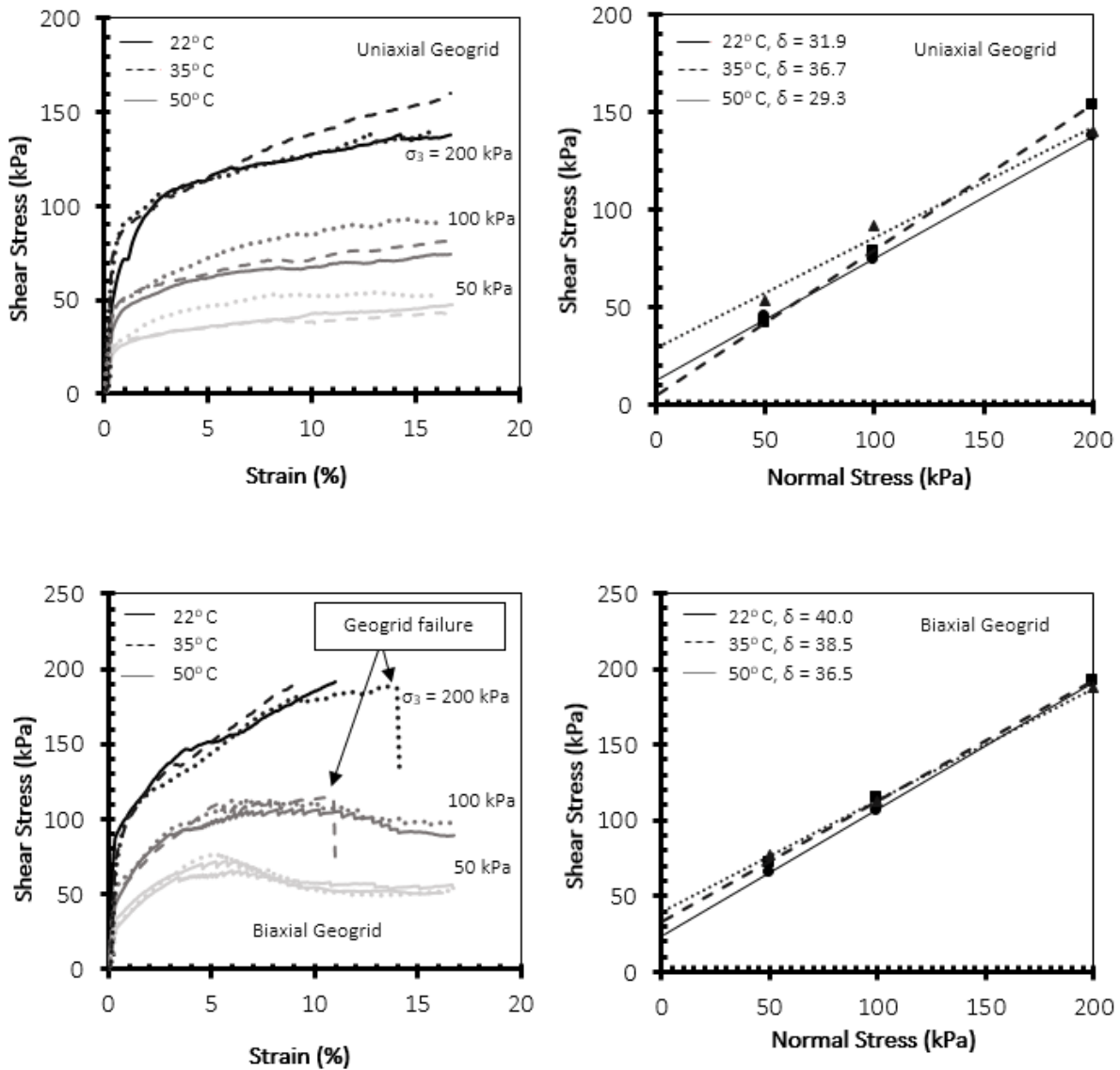


Figure 4.12 (continued). Interface direct shear test results for RAP-geosynthetic interaction and Mohr-Coulomb failure envelopes.

Table 4.5. Interface Friction Angles, and Efficiency Factors between RAP and Selected Geosynthetic Reinforcements at Different Temperatures.

Interface type	Source	Temp. (° C)	Interface friction angle (δ)	Efficiency factor (E_ϕ)	
RAP-Woven geotextile	This study	22	24.8	0.82	
	This study	35	23.3	0.77	
	This study	50	22.1	0.72	
	Gravel	Hsieh et al. (2011)	22	27.0	0.64
	Crushed Stone	Hsieh et al. (2011)	22	30.6	0.41
	Sand	Hsieh et al. (2011)	22	35.4	0.92
	FDS	Goodhue et al. (2001)	22	29.0	0.26-0.32
RAP-Nonwoven geotextile	This study	22	17.3	0.56	
	This study	35	20.4	0.67	
	This study	50	19.5	0.63	
RAP-Uniaxial geogrid	This study	22	31.9	1.11	
	This study	35	36.7	1.33	
	This study	50	29.3	1.00	
	Gravel	Nejad et al. (2012)	22	44.4	0.95
	Sand	Nejad et al. (2012)	22	33.8	0.97
	FDS	Goodhue et al. (2001)	22	26.0-31.0	0.80-0.60
RAP-Biaxial geogrid	This study	22	40.0	1.5	
	This study	35	38.5	1.42	
	This study	50	36.5	1.32	
	RAP	Arulrajah et al. (2013)	22	40.5	0.71
	Gravel	Hsieh et al. (2011)	22	38.7	1.01
	Crushed Stone	Hsieh et al. (2011)	22	43.4	0.66
	Sand	Hsieh et al. (2011)	22	37.0	0.98

Compaction could have increased the surface interaction between RAP and the reinforcement at 35° C. However, at 50° C, the bituminous content in RAP may reduce the particle surface roughness, which could have decreased the effects of friction. As observed in previous tests, the nonwoven geotextile suffered considerable deformation at its cross-section and at the clamp attachments where the geotextile was fixed to the lower box.

The δ between RAP and the uniaxial geogrid reached an optimum at 35° C, with a value of 36.7°, and E_ϕ of 1.33. At 22 °C, the observed δ of 31.9° was comparable to FDS (31.0 °) reported by Goodhue et al (2001), but smaller than sand (33.8°) reported by Nejad et al. (2012). The high E_ϕ observed in RAP-uniaxial geogrid may be the result of bearing interaction between the soil and the ribs of the reinforcement. In addition, RAP particles used in this study were sufficiently small to intrude into the ribs of the geogrid, which would further augment bearing forces acting against

shear movement. Insignificant deformations were observed in the extruded uniaxial geogrid, however, the same physical constraints of the uniaxial geogrid observed with RCA may be considered with RAP.

RAP and the biaxial geogrid attained the largest δ (40.0°) at 22°C , representing E_ϕ of 150%. A similar δ (40.5°) was reported by Arulrajah et al. (2013), but with a significantly lower E_ϕ of 77.0%. RAP performed better than other coarser materials, such as sand and gravel, with δ of 37.0° and 38.6° respectively (Hsieh et al. 2011).

The biaxial geogrid showed excessive interaction with the shear box, and the same constraints observed in section 4.3.1 (between RCA and biaxial geogrid) apply here. Failure due to geogrid rupture was observed at a normal pressure of 100 kPa (35°C), and at 200 kPa (50°C). The large scale direct shear equipment reached a force limit of 17.8 kN at the normal pressure of 200 kPa (22°C and 35°C). At this point the test was stopped and further shear was not possible.

4.4. Pull-out Test Results

4.4.1. RCA

The pull-out strength of RCA reinforced with woven geotextile and uniaxial geogrid was evaluated at different normal stresses. Plots of pull-out force per unit length versus horizontal displacement for woven geotextile and uniaxial geogrid are shown in Figure 4.13. The interaction coefficient (C_i) between RCA and the reinforcements were calculated for each normal stress and the average was obtained. The values of C_i are presented in Table 4.6.

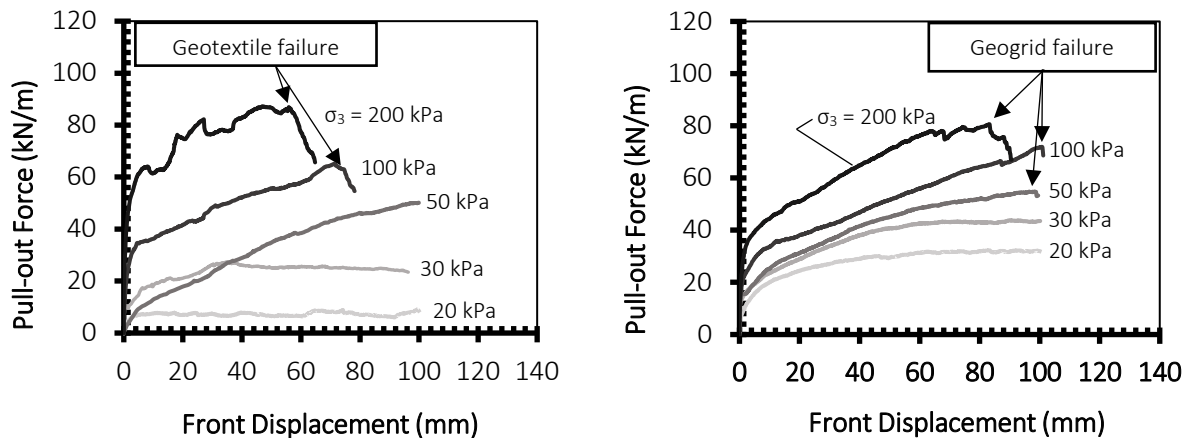


Figure 4.13. Pull-out test results for RCA reinforced with woven geotextile (left), and uniaxial geogrid (right)

Table 4.6. RCA Coefficient of Interaction from Pull-out Tests.

Geosynthetic type	Normal Stress (kPa)	Coefficient of Interaction (C_i)
Geotextile	20	0.13
	30	0.29
	50	0.32
	100	0.21
	200	0.14
	Average	0.22
Geogrid	20	0.52
	30	0.45
	50	0.34
	100	0.23
	200	0.13
	Average	0.33

The uniaxial geogrid presented higher pull-out force (or pull-out resistance) than the woven geotextile at lower normal stresses (e.g. 20 and 30 kPa). The pull-out force of the geotextile gradually approached that of the geogrid with increasing normal stresses. This behavior is also noted in the values of C_i , which was defined in section 1.2.2.3, of Chapter 1. The values of C_i for the geogrid are higher than those of the geotextile at lower normal stresses (20 and 30 kPa), but become similar with increasing normal pressures (50, 100 and 200 kPa). The values observed for geotextile and geogrid indicate a weaker bond between RCA and each of the geosynthetics (e.g. $C_i < 0.5$).

The interaction between RCA and each of the two geosynthetic reinforcements exhibited distinct characteristics. The C_i values for geotextile increased with normal stress, reaching a peak at the moderate normal stress of 50 kPa. A similar pattern was reported by Tatlisoz et al. (1996). In contrast, C_i values for the geogrid peaked at the lowest normal pressure of 20 kPa and thereafter decreased with increasing normal stress.

The decrease in C_i values observed in the geogrid were expected. Typically, increasing normal stress causes increasing progressive failure in reinforcements. Bakeer et al. (1998) reported similar values and a decreasing pattern for lightweight aggregates reinforced with uniaxial geogrid. This behavior was reported also by Tatlisoz et al. (1996) from tests for sand/tire chip mixtures reinforced with uniaxial geogrid.

4.4.2. RAP

Plots of pull-out force vs horizontal displacement for geotextile and geogrid are shown in Figure 4.14. The C_i between RAP and the reinforcements were calculated for each normal stress, and the average was obtained. The values of C_i are presented in Table 4.7.

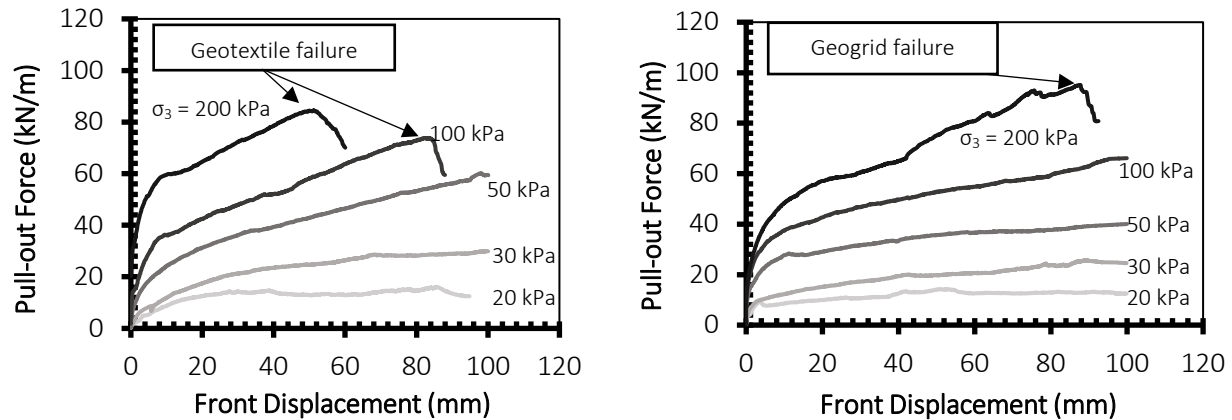


Figure 4.14. Pull-out test results for RAP reinforced with woven geotextile (left), and uniaxial geogrid (right)

Table 4.7. RAP Coefficients of Interaction from Pull-out Tests.

Geosynthetic type	Normal Stress (kPa)	Coefficient of Interaction (C _i)
Geotextile	20	0.21
	30	0.26
	50	0.32
	100	0.19
	200	0.11
	Average	0.22
Geogrid	20	0.16
	30	0.22
	50	0.21
	100	0.17
	200	0.12
	Average	0.18

The geotextile presented progressive deformation with increasing normal pressure, and ruptured at 100 and 200 kPa. Rupture occurred at displacements of 82.0 mm and 48.0 mm, respectively. The geotextile exhibited slightly larger pull-out capacity than the geogrid. This observation is consistent with findings reported by Tatlisoz (1996) from tests using a tire chip/sand mixture aggregate. In contrast, the geotextile achieved a lower pull-out capacity than the geogrid at 200 kPa. This may be the result of tensile failure on the geotextile at 55.0 mm of displacement, thus impeding further development of pull-out resistance.

The geogrid exhibited progressive failure at 63.0 mm and 75.0 mm under the normal stress of 200 kPa and ruptured at 83.0 mm. No rupture was observed in the geogrid at lower normal stress. C_i values observed for RAP followed similar characteristics observed in RCA. RAP/geotextile

interaction yielded an initial increase of C_i values with increasing normal stress. The peak C_i value occurred at 50 kPa normal, and declined thereafter. C_i values for RAP/geogrid initially increased from 20 to 30 kPa, but declined from 30 to 200 kPa normal stresses.

As observed previously, decrease in C_i values are expected in the geogrid. The original increase in C_i may be due to the inability of sand-size RAP particles to properly interlock with the geogrid at very low normal stress (e.g. 20 kPa).

Pull-out test results for geosynthetics embedded in RCA and RAP were not found in the literature. Table 4.8 presents C_i values of several aggregates and their respective geosynthetic reinforcement. These values reflect the wide variability of geosynthetic strength and geometry, as well as in soil properties.

Table 4.8. Coefficients of Interaction Between Several Soils and Geosynthetics Reported in the Literature.

Soil Type	Reinforcement type	Soil friction angle (Φ)	C_i	References
Sand	Woven geotextile (PP)	37.5	0.92	Hsieh et al. (2011)
	Geogrid (PET)	37.5	0.93	
	Uniaxial geogrid	34.7	0.43	Nejad et al. (2012)
Gravel	Woven geotextile (PP)	38.4	0.42	Hsieh et al. (2011)
	Geogrid (PET)	38.4	0.88	
	Geogrid uniaxial	45.9	0.71	Nejad et al. (2012)
Crushed stone	Woven geotextile (PP)	55.0	0.36	Hsieh et al. (2011)
	Geogrid (PET)	55.0	0.58	
FDS	Woven geotextile (PP)	43.0	0.32	Goodhue et al. (2001)
	Woven geotextile (PP)	31.0	0.26	
	Uniaxial geogrid (PET)	31.0	0.44	

4.5. Creep Response of RAP

4.5.1. Triaxial Compression

Table 4.19 is a summary of results from CD triaxial compression tests conducted on compacted RAP specimens at 22 °C.

Table 4.9. Summary of Triaxial Compression and Deviatoric Creep Tests.

Test	Compaction and Consolidation Temperature (°C)	Test Temperature (°C)	Confining Pressure, σ'_3 (kPa)	Stress Level, \bar{D}
Triaxial compression	22	22	35, 70, 140	-
	35	22	70	-
	50	22	70	-
Deviatoric creep	22	22	70	0.40, 0.60, 0.80, 0.85, 0.90, 0.95
	35	22	70	0.95
	50	22	70	0.95
	22	35	70	0.95
	22	50	70	0.95

Figure 4.15(a) is the relation between deviator stress (σ'_d) and axial strain (ϵ) for specimens consolidated to σ'_3 of 35 kPa, 70 kPa, and 140 kPa. Figure 4.15(b) is the corresponding relation between volumetric strain (ϵ_{vol}) and axial strain.

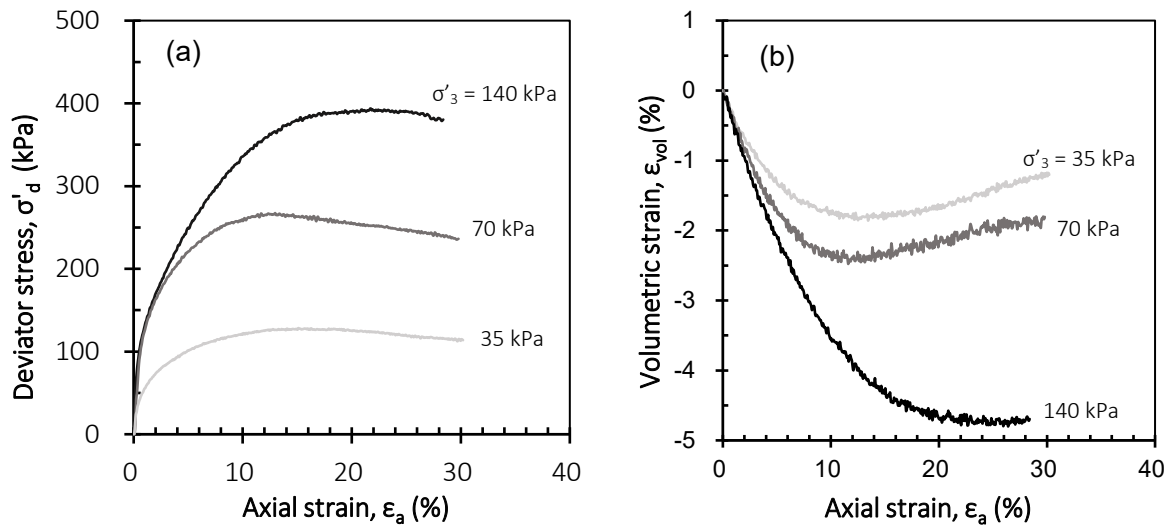


Figure 4.15. Results of CD triaxial compression tests for compacted RAP at room temperature: (a) deviator stress versus axial strain and (b) volumetric strain versus axial strain.

Similar to conventional granular materials, increases in σ'_3 systematically increased the deviator stress at failure (σ_{df}). Corresponding axial strain at failure (ϵ_{af}) also increased and specimen volume change behavior became more compressive. Shear strength parameters determined from

the triaxial compression tests were $c \approx 11.0$ kPa and $\phi \approx 36^\circ$. These values are comparable to those of compacted sand and are within the appropriate range for use of the material as embankment fill or backfill (Holtz et al. 2011).

Figure 4.16 compares the evolution of volume change during the consolidation phase for RAP specimens at 22 °C, 35 °C, and 50 °C.

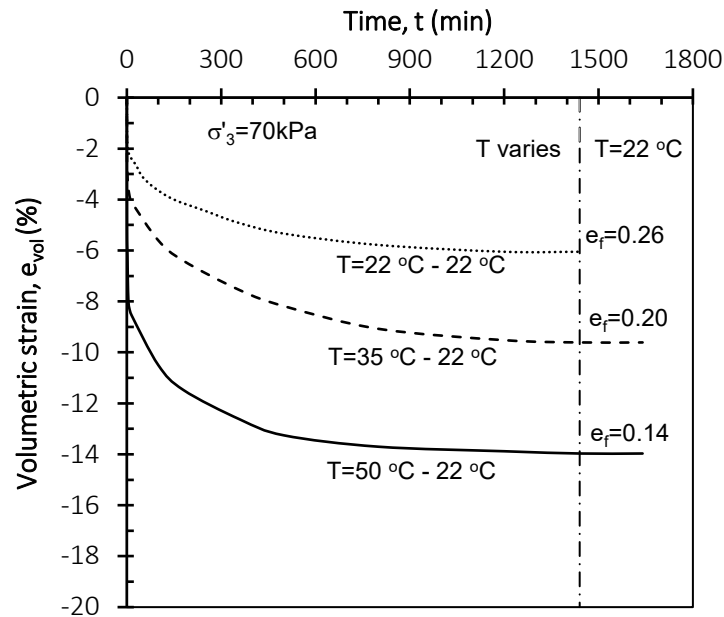


Figure 4.16. Evolution of volumetric strain with time through consolidation at different temperatures ($T=35$ °C- 22 °C represents the compaction temperature of 35 °C and shearing temperature of 22 °C).

Specimens consolidated at elevated temperature (35 °C and 50 °C) exhibited more compressive volumetric strains than the specimen at 22 °C. Void ratio (e) at the end of consolidation for RAP specimens at 22 °C, 35 °C, and 50 °C was 0.26, 0.20, and 0.14, respectively. This is a reduction of 23% and 46% relative to the specimen at 22 °C for the tests at 35 °C and 50 °C, respectively. RAP specimens compacted and consolidated at the higher temperatures and then reduced to 22 °C are thus expected to have higher stiffness and shear strength compared to specimens maintained at 22 °C throughout compaction, consolidation, and shear. This is confirmed in Figure 4.17, which is a plot of stress–strain curves (Figure 4.17a) and volume change behavior (Figure 4.17b) for RAP specimens compacted and consolidated at 22 °C, 35 °C, and 50 °C and then sheared at 22 °C.

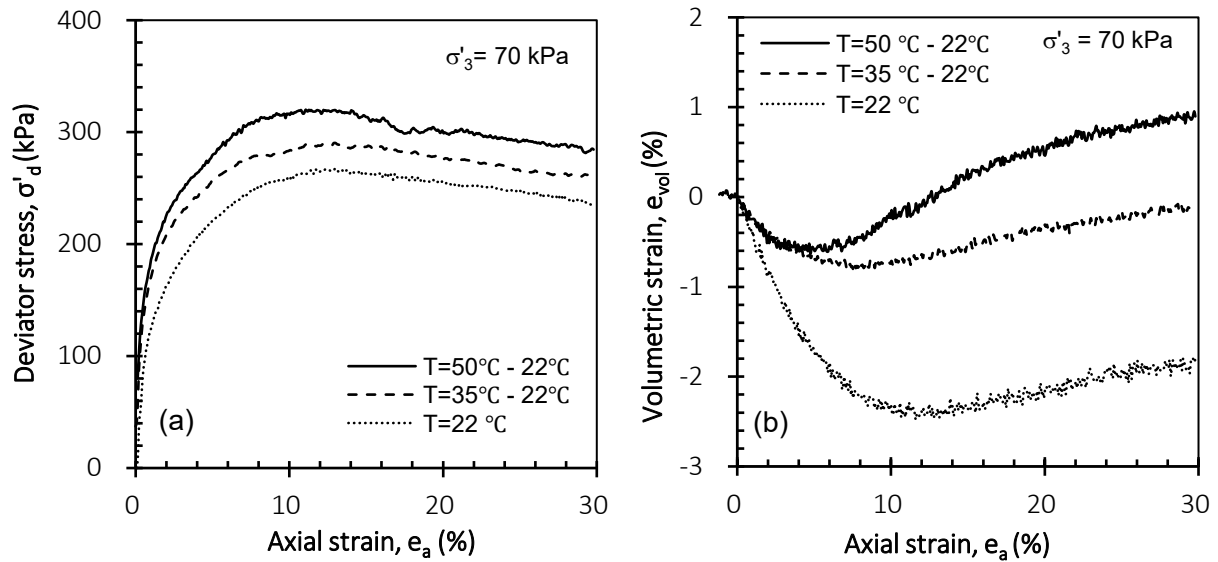


Figure 4.17. Results of CD triaxial compression tests for RAP compacted and consolidated at different temperatures but sheared at 22 °C ($\sigma'_3=70$ kPa for these tests): (a) deviator stress versus axial strain and (b) volumetric strain versus axial strain

Increases in stiffness and strength for the specimens consolidated at elevated temperature are evident. The E_{50} increased from 11,400 kPa for the RAP specimen prepared at 22 °C to 20,050 kPa for the specimen prepared at 35 °C and further increased to 24,600 kPa for the specimen prepared at 50 °C. The σ_{df} increased from 265 kPa for the RAP specimen prepared at 22 °C to 290 kPa for the specimen prepared at 35 °C and further increased to 320 kPa for the specimen prepared at 50 °C. The volume change behavior was transformed from compressive for specimens prepared at 22 °C to dilative for specimens prepared at elevated temperatures (i.e., 35 °C and 50 °C).

4.5.2. Creep Response at Non-Elevated Temperature

Figure 4.18 is a summary of results from deviatoric creep tests for specimens compacted and consolidated at 22 °C.

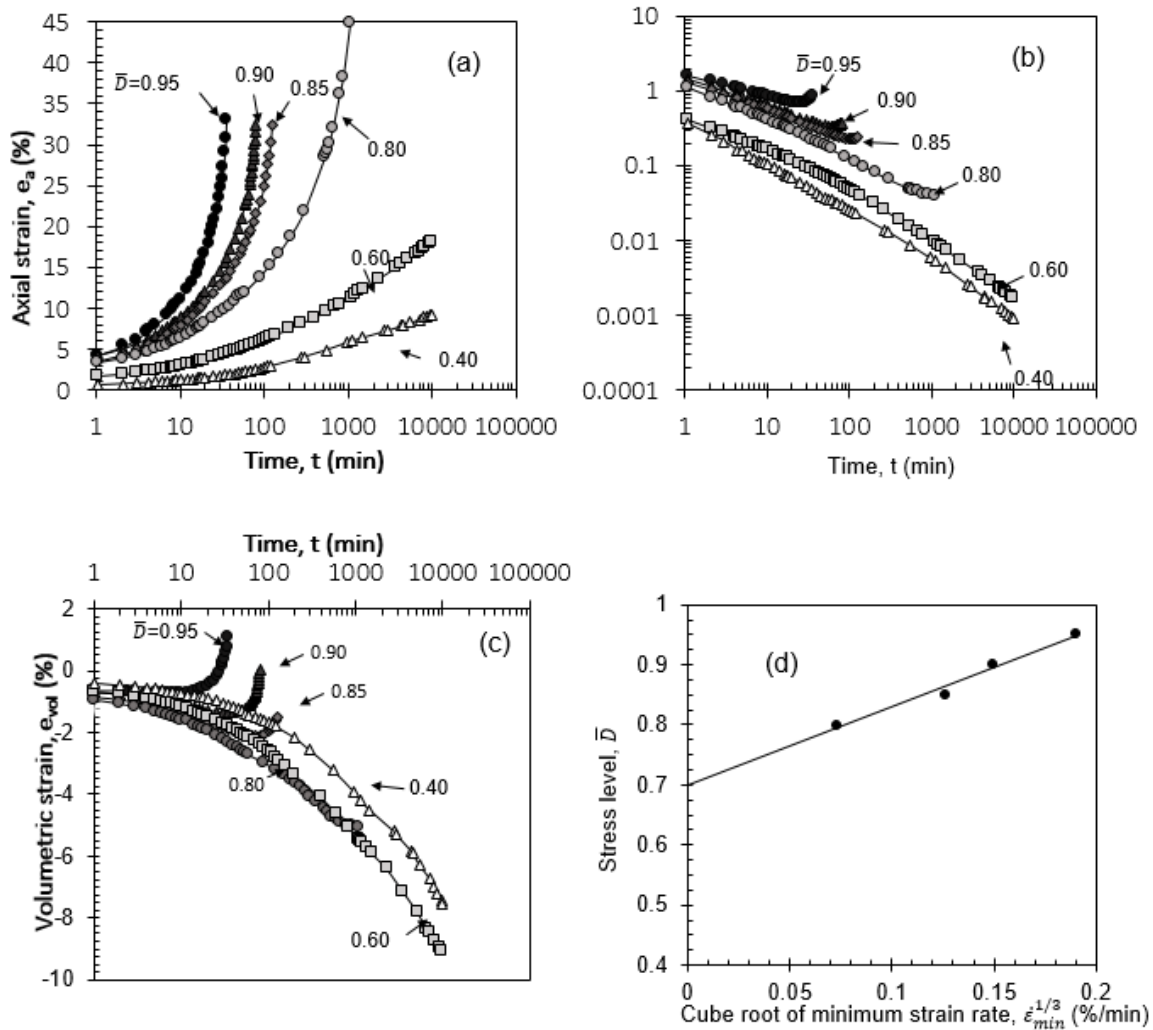


Figure 4.18. Creep test results for RAP at 22 °C and $\sigma_3' = 70$ kPa: (a) axial strain versus time (b) axial strain rate versus time (c) volumetric strain versus time and (d) stress level versus cube root of minimum strain rate.

Figure 4.18(a) is a plot of the evolution in axial strain (ϵ_a) with logarithm of time for creep tests at various deviator stress ratios. Axial strain increased with time for any given \bar{D} , which indicates the creep susceptibility of compacted RAP. At $\bar{D} \geq 0.80$, the specimens failed along clearly evident shear planes. Creep strain increased more rapidly as the stress level increased, which may be attributed to increasing shear strain between the particles due to presence of asphalt binder at the contact surfaces between individual RAP particles.

Figure 4.18(b) is a plot of axial strain rate $\dot{\epsilon}_a$ calculated by differentiation of the data in Figure 4.18(a) versus elapsed time on a log-log scale. Axial strain rate decreased with elapsed time and with decreasing deviator stress ratio. The $\dot{\epsilon}_a - \log t$ curves form a series of parallel lines before creep rupture, and therefore can be predicted using the three-parameter empirical creep model suggested by Singh and Mitchell (1968):

$$\dot{\epsilon}(t) = Ae^{\bar{\alpha}\bar{D}} \left(\frac{t_1}{t}\right)^m \quad (4.1)$$

where A , $\bar{\alpha}$ and m are model parameters, t_1 is an arbitrary reference time, and t is the elapsed time after loading. Parameter $\bar{\alpha}$ is an indicator of the effect of stress intensity on the creep rate and parameter A reflects the order of magnitude of the creep rate.

A plot of $\log \dot{\epsilon}_a$ versus \bar{D} may be used to calculate $\bar{\alpha}$ from the slope and A from the intercept at unit time. The slope of the $\log \dot{\epsilon}_a - \log t$ curve yields the creep rate parameter m that characterizes creep potential of soils. A larger value of m indicates lower creep potential and indicates that the strain rate decreases more rapidly during creep. Materials with low creep potential such as sand exhibit higher m , i.e., between about 0.9 and 1.1 (Murayama et al. 1984; Mejia et al. 1988). Materials with high creep potential such as clay typically have m between about 0.4 and 0.7 (Mitchell and Soga 2005). Average m value for the RAP sample at 22 °C is 0.72, which indicates a relatively high creep potential of the material. The average slope of the $\log \dot{\epsilon}_a - \bar{D}$ curves for the RAP at 22 °C is $\bar{\alpha} = 1.25$, which is within the range of 1.0 to 7.0 reported for many types of soils (Kuhn and Mitchell 1993). An A value of 0.12 %/min for RAP interpreted from the y -intercept of the $\log \dot{\epsilon}_a - \bar{D}$ curve corresponding to $t_1 = 1$ min is higher than the wide range of 2×10^{-8} %/min to 4×10^{-3} %/min reported for soils (Kuhn and Mitchell 1993).

For $\bar{D} \geq 0.80$, the $\log \dot{\epsilon}_a - \log t$ curves on Figure 4.18(b) exhibit a minimum point where $\dot{\epsilon}_a$ starts to increase. This corresponded to the observed specimen failure, and thus the initiation of creep rupture in Figure 4.18(b) is identified when $\dot{\epsilon}_a$ starts to increase with time. As indicated on Figure 4.18(c), corresponding volumetric strain starts to increase with the initiation of creep rupture for RAP specimens at $\bar{D} \geq 0.80$. This is consistent with a change in axial strain rate and creep rupture of the specimen. For $\bar{D} < 0.8$, the plots of axial strain rates versus time in Figure 4.18(b) appear to proceed along parallel lines with no evident increase in strain rate after one week. It is thus reasonable to project that the specimens subject to stress level of $\bar{D} < 0.8$ are unlikely to fail. Volumetric strain for $\bar{D} < 0.8$ consistently decreased with increasing time during the creep test without any sign of dilative behavior.

The deviator stress level below which creep rupture does not occur is termed the upper yield strength, \bar{D}_{uy} (Murayama and Shibata 1958, 1964). Finn and Snead (1973) suggested that the upper yield strength of a material can be estimated from the y -intercept of a linear variation of \bar{D} with the n^{th} root of minimum strain rate ($\dot{\epsilon}_{min}^{1/n}$). The n -value is selected such that a linear relationship between \bar{D} and $\dot{\epsilon}_{min}^{1/n}$ is obtained. Finn and Snead (1973) suggested that the $n=3$ (cubed root) gives a linear relationship between \bar{D} and $\dot{\epsilon}_{min}^{1/3}$. Figure 4.18(d) for the compacted RAP at 22 °C shows that for $n = 3$, there is a linear relationship between \bar{D} and $\dot{\epsilon}_{min}^{1/3}$. Soleimanbeigi et al. (2014) also reported that $n = 3$ renders a linear relationship between \bar{D} and $\dot{\epsilon}_{min}^{1/3}$ for compacted recycled asphalt shingles (RAS) mixed with 75% by weight bottom ash (BA). The \bar{D} intercept in the plot indicates that \bar{D}_{uy} for RAP is 0.70. The \bar{D}_{uy} for the compacted

RAS-BA mixture was 0.80 Soleimanbeigi et al. (2014). The reason can be attributed to smaller contact surfaces containing asphalt binder in the compacted RAS-BA mixture compared with the RAP specimen for which the asphalt binder coats the majority of the particles. The practical implication is that mobilized shear strength for RAP compacted at non-elevated temperatures in beneficial use applications should be less than 70% of the compressive strength (σ_{df}).

4.5.3. Creep Response at Elevated Temperature

Figures 4.19(a)-(c) are results for specimens compacted and consolidated at 22 °C and then subject to deviatoric creep ($\bar{D} = 0.95$) at 22 °C, 35 °C, and 50 °C.

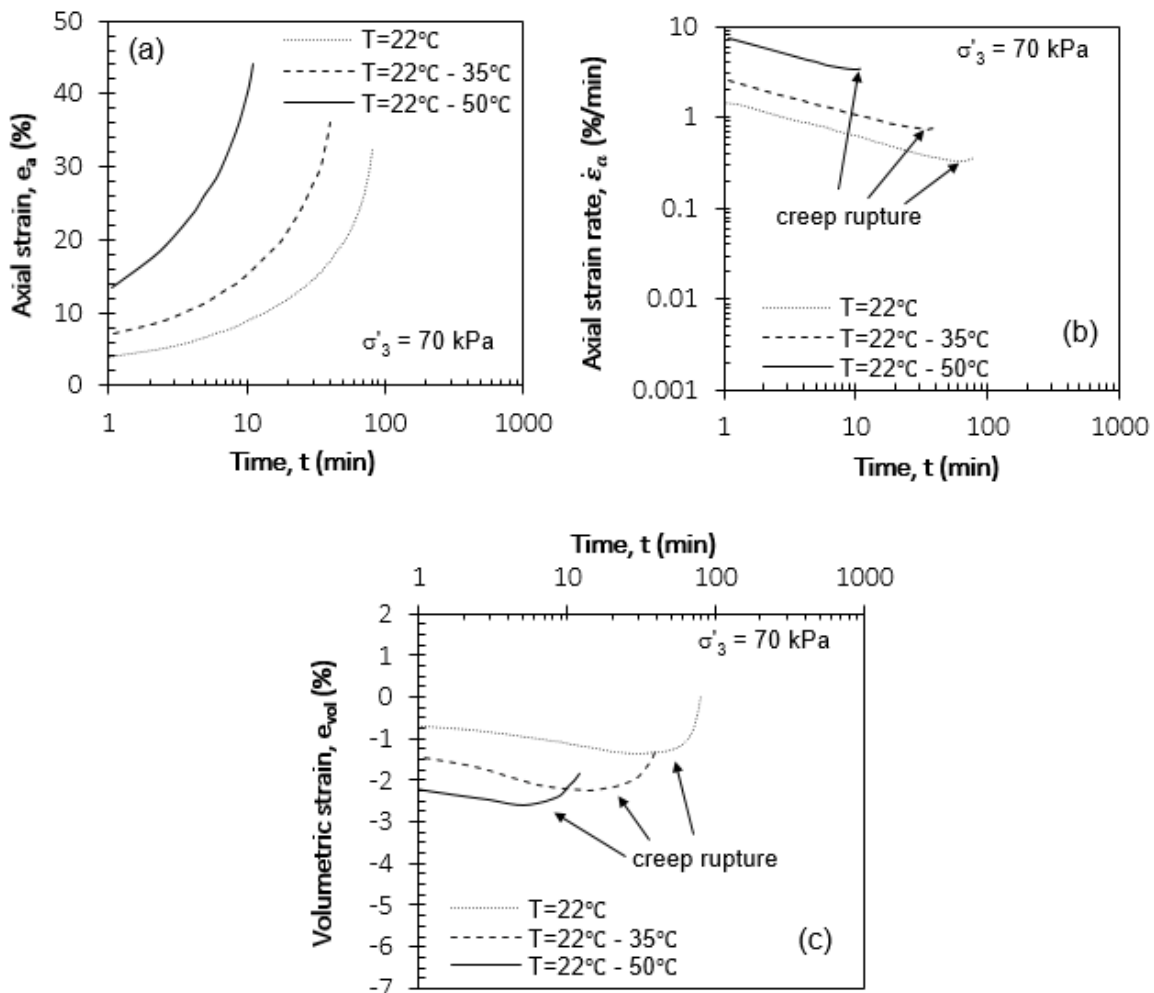


Figure 4.19. (a) Axial strain (b) axial strain rate, and (c) volumetric strain vs. time for RAP compacted and consolidated at 22 °C and subject to creep at different temperatures ($\sigma'_3 = 70$ kPa).

Figure 4.19(a) shows the axial strain versus time for RAP specimens initially compacted and consolidated at 22 °C. Increasing the creep temperature systematically increased axial strain at different times and the cumulative axial strain at the end of each test. The increase in axial strain at higher temperature is attributed to reduction in viscosity of asphalt binder coatings on the RAP particles, which accommodates deformation. Figure 4.19(b) is a log–log plot of corresponding axial strain rate $\dot{\epsilon}_a$ versus elapsed time. Strain rate increased with increasing creep temperature.

At $t=1$ min, strain rate increased from 1.46 %/min to 2.59 %/ min when the temperature increased from 22 °C to 35 °C and further increased to 7.39 %/min when the temperature was increased to 50 °C. Nonetheless, the $\log \dot{\epsilon}_a - \log t$ curves remain parallel lines at elevated temperatures before the initiation of creep rupture. Each $\log \dot{\epsilon}_a - \log t$ curve also exhibits a minimum point where the $\dot{\epsilon}_a$ starts to increase with imminent rupture. As indicated, the increase in temperature also reduced the cumulative time to creep rupture (t_r). Increasing the temperature from 22 °C to 35 °C and to 50 °C reduced t_r from 60 min, to 34 min to 10 min, respectively, thus indicating that elevated temperature does increase the susceptibility of RAP to creep rupture.

These results suggest that after construction of a RAP fill, creep strain rate and rupture susceptibility are expected to increase when the field temperature increases. Figure 4.19(c) is a corresponding plot of volumetric strain with time, where it is apparent that increasing temperature also increased the volumetric strain. At $t=1$ min, ϵ_{vol} increased from -0.69% to -1.44% when the temperature was increased from 22 °C to 35 °C. Increasing the temperature to 50 °C increased the ϵ_{vol} to -2.24% at $t = 1$ min. As illustrated in Figure 4.19(c), the volumetric strain for each specimen during creep test decreases over time until the specimen failure when the volumetric strain starts to increase indicating the dilative behavior of the RAP specimens during shearing.

Figures 4.20(a)-(c) are results from creep tests for RAP specimens compacted and consolidated at different temperatures and subject to creep at 22 °C. As shown in Fig. 4.20(a), axial strain of the RAP specimen compacted at 22 °C increased more rapidly compared to specimens compacted at 35 °C or 50 °C.

Increasing the compaction/consolidation temperature reduced the axial strain and axial strain rate [Fig. 4.20(b)] at any given time. This resulted in a beneficial effect with respect to creep in a manner similar to that for shear strength as described before. Figure 4.20(b) shows that the initial strain rate (at $t=1$ min) decreased from 1.46 %/min to 0.92 %/min when the temperature increased from 22 °C to 35 °C and to 0.38 %/min when the temperature was increased to 50 °C. Increasing the compaction/consolidation temperature from 22 °C to 35 °C, increased the time to creep rupture, t_r , from 24 min to 850 min. Increasing the compaction/consolidation temperature to 50 °C increased t_r to 4630 min. Compaction and consolidation at elevated temperatures also increased the volumetric compressive strain [Figure 4.19(c)], therefore reducing the void space and increasing the shear strength as illustrated in Figure 4.16 and Figure 4.17. The practical implication of this observation is that if an embankment fill or backfill containing RAP is compacted and brought to equilibrium with the operating stresses at relatively high temperature (e.g., construction during summer), then the majority of compression occurs during construction and creep strain rates and rupture susceptibility would be expected to decrease during subsequent seasons.

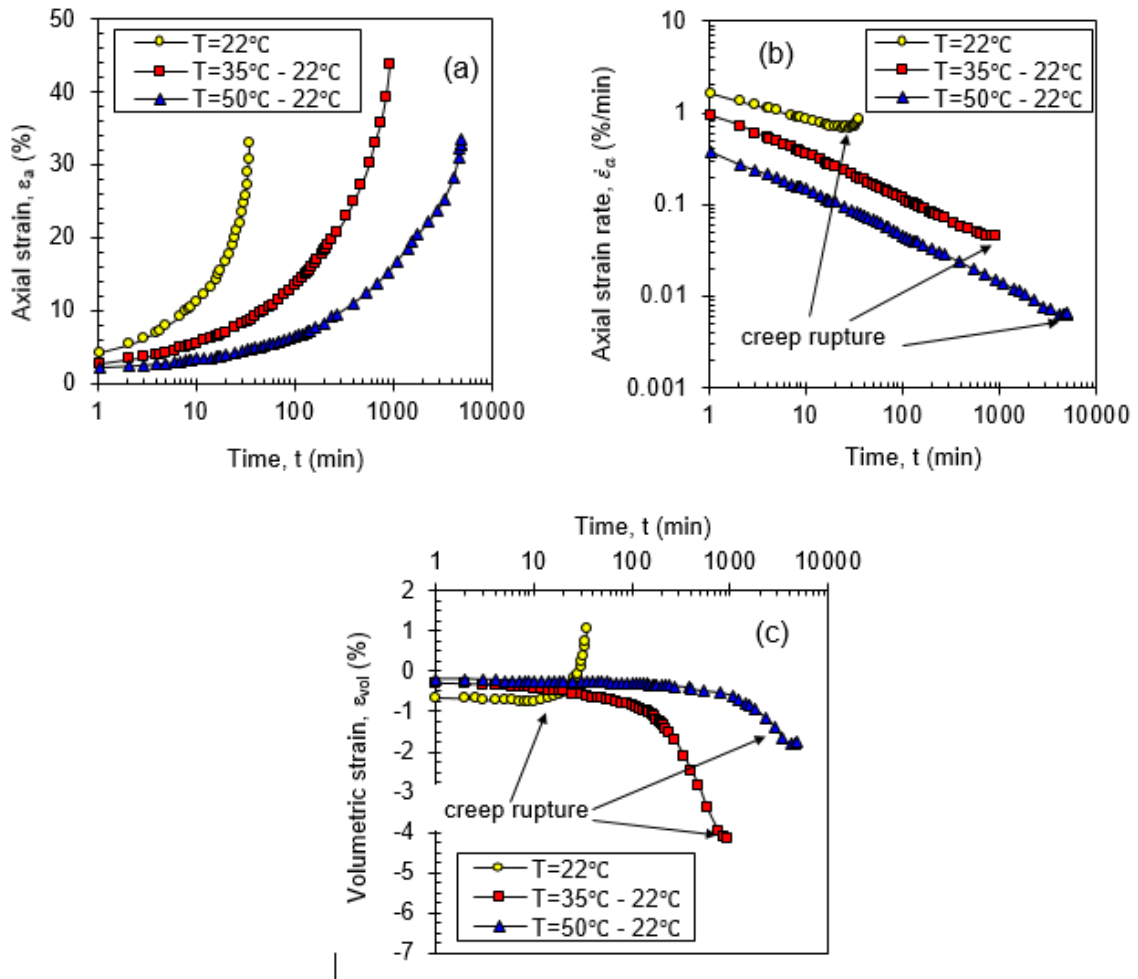


Figure 4.20. (a) Axial strain (b) axial strain rate, and (c) volumetric strain vs. time for RAP compacted and consolidated at different temperatures and subject to creep at 22°C ($\sigma'_3 = 70$ kPa)

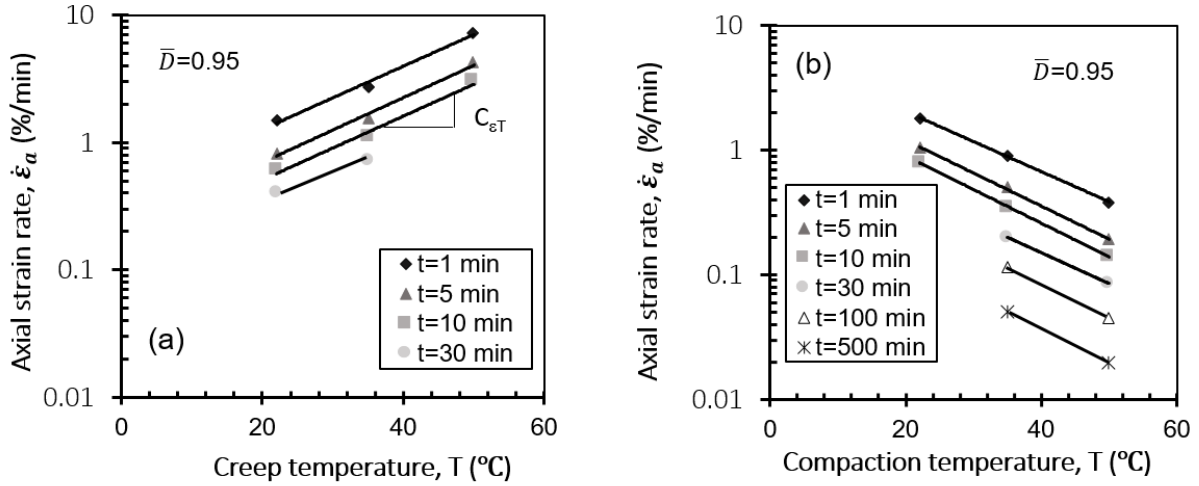


Figure 4.21. Variation of axial strain rate for compacted RAP with (a) creep temperature and (b) compaction temperature.

4.5.4. Coefficients of Thermal Creep

Figure 4.21(a) is a plot of the variation in axial strain rate with creep temperature at different elapsed times during the creep tests. The $\log \dot{\epsilon}_a$ values linearly increase with temperature and have almost identical slopes at different elapsed times. The slope of the $\log \dot{\epsilon}_a - T$ curves is defined as the coefficient of thermal creep ($1/^\circ\text{C}$) and is denoted $C_{\epsilon T}$. The average $C_{\epsilon T}$ for the RAP specimens is $0.058 \text{ } 1/^\circ\text{C}$. The equation for the $\log \dot{\epsilon}_a - T$ curves is thus represented by:

$$\frac{d \ln \dot{\epsilon}(t)}{dT} = C_{\epsilon T} \quad (4.2)$$

Integrating Eq. (4.2) over a finite temperature range leads to the following relation:

$$\dot{\epsilon}(T, t) = \dot{\epsilon}(T_o, t) e^{C_{\epsilon T}(T-T_o)} \quad (4.3)$$

where T_o is a reference temperature. Equation (4.3) indicates that the strain rate of compacted RAP is an exponential function of temperature change. Substitution of Eq. (4.3) into Eq. (4.1) leads to:

$$\dot{\epsilon}(T, t) = A e^{\bar{\alpha} \bar{D}} \left(\frac{t_1}{t}\right)^m e^{C_{\epsilon T}(T-T_o)} \quad (4.4)$$

or

$$\dot{\epsilon}(T, t) = A e^{\bar{\alpha} \bar{D} + C_{\epsilon T}(T-T_o)} \left(\frac{t_1}{t}\right)^m \quad (4.5)$$

where Equation (5) includes the effect of temperature in the Singh and Mitchell (1968) creep model. Soleimanbeigi et al. (2014) obtained a similar equation to account for the effect of temperature on strain rate of recycled asphalt shingles (RAS) mixed with granular materials. The strain rate of RAS mixed with granular materials was also observed to be an exponential function of temperature, although the range of temperature in Soleimanbeigi et al. (2014) was limited to between 7 °C and 35 °C.

Figure 4.21(b) indicates that a linear trend also exists between $\log \dot{\epsilon}_a$ and compaction/consolidation temperature. The average $C_{\epsilon T}$ for this relation is $-0.060 \text{ 1/}^\circ\text{C}$. It is notable that the magnitudes of $C_{\epsilon T}$ for the two different scenarios (i.e. RAP compacted at room temperature and then subject to creep at different temperatures and RAP compacted at different temperatures and then subject to creep at room temperature) are nearly identical, except that for the first scenario, the strain rate increases with temperature and for the second scenario, the strain rate decreases with temperature. The coefficient $C_{\epsilon T}$ is therefore recommended as approximately $-0.06 \text{ 1/}^\circ\text{C}$ to estimate the strain rate of RAP when compacted at an elevated temperature; and as $0.06 \text{ 1/}^\circ\text{C}$ to estimate the strain rate of RAP when compacted at room temperature and creeps at an elevated temperature. Soleimanbeigi et al. (2014) reported $C_{\epsilon T}=0.012 \text{ 1/}^\circ\text{C}$ for RAS-BA specimens which indicates lower sensitivity for strain rate of the RAS-BA specimens at elevated temperatures compared with the compacted RAP. Possible reason is attributed to smaller total contact surface area that contains asphalt binder in the RAS-BA specimens compared to RAP specimens that the majority of the particles are coated with asphalt binder. The obtained $C_{\epsilon T}$ for the compacted RAP corresponds to the shear stress level of $\bar{D}=0.95$. Soleimanbeigi et al. (2014) reported that $C_{\epsilon T}$ for compacted RAS decreases with increasing the stress level. The design factor of safety for slopes is typically low (i.e., 1.3-1.5) compared to that for foundations (i.e., 3.0), therefore the mobilized shear stress levels in the slopes are relatively higher. Since the creep strain of the compacted RAP is more significant at higher shear stress levels, $C_{\epsilon T}=0.060 \text{ 1/}^\circ\text{C}$ corresponding to $\bar{D}=0.95$ is recommended to estimate strain rates at different temperatures.

4.6. Drainage Performance of RCA/Geotextile Systems

Drainage performance tests take a very long-time in the order of 3 to 4 months for each test. Considering the duration of this research project a decision had to be made to evaluate either RCA or RAP drainage performance, as being able to conduct performance tests with both materials at the same time was not practically possible. Based on the detailed previous research completed at the University of Wisconsin and the University of Maryland, it is known that RAP is a hydrophobic material with better drainage capacity compared to RCA (Edil et al. 2012, Aydilek and Mijic 2015). Considering that in the field implementation, the agency will have same gradation requirement regardless of the material, RCA was selected for the evaluation because for the same particle size distribution and same geotextile, it would provide lower performance. Also, the RCA selected for this evaluation was specifically chosen because it had fine sands content very close to 60%, which is the upper boundary for the high quality backfill suggested by Berg et al. (2009). Therefore the results provided in this section are believed to represent a range that may not be the absolute worst scenario but a reasonable range with confidence. All performance evaluations were focused on migration of particles on to both commonly used woven geotextile for reinforcement and commonly used nonwoven geotextile for drainage within typical MSE wall facings and behind and underneath the reinforced zones.

4.6.1. Analyses of Clogging Behavior

The values of K_R for the RCA-geotextile systems exposed to filtration in the laboratory study are given in Table 4.10. A review of the data shows that two geotextiles tested with RCA would be generally considered unclogged based on the criterion that sets a K_R of 3 as the limit, a limit used by previous researchers (Kutay and Aydilek 2005, Koerner 2012). Analysis of the K_R ratios, which are based on the measured hydraulic conductivities at different locations in the soil, shows that they could be slightly higher than 3 in two of the tests with the nonwoven. However, these were obtained at a very high gradient ($i=5$) that would normally not be present in retaining wall backfills. Similarly, one of the tests with the woven geotextile (GRT2) resulted in an unusually high K_R (i.e., 9.6) under a moderate gradient. However in all tests, k_{system} under hydraulic gradients of 1 and 2.5 ranged from 10^{-2} to 10^{-4} cm/s, which is not unusual for backfills that may be used in MSE walls.

Table 4.10. Stabilized permeability ratio and system hydraulic conductivity values of the RCA-geotextile systems at the end of each hydraulic gradient.

Geotextile	Virgin geotextile permittivity, Ψ (s^{-1})	Permittivity ratio, Ψ_R	i=1		i=2.5		i=5	
			K_R	k_{system} (cm/s)	K_R	k_{system} (cm/s)	K_R	k_{system} (cm/s)
GRT1-a (NW)	1.7	NA	1.07	1.1 $\times 10^{-2}$	1.27	3.9 $\times 10^{-3}$	3.2	7 $\times 10^{-4}$
GRT1-b (NW)	1.7	NA	1	5 $\times 10^{-3}$	1.03	4.4 $\times 10^{-3}$	1.52	1.1 $\times 10^{-3}$
GRT1-c (NW)	1.7	0.93	1.49	5.4 $\times 10^{-3}$	1.81	3.0 $\times 10^{-3}$	3.1	9.1 $\times 10^{-4}$
GRT2 (W)	0.4	0.65	1.53	4.6 $\times 10^{-2}$	9.6	2 $\times 10^{-2}$	NA	NA
GRT3 (W)	0.4	0.83	0.91	6.7 $\times 10^{-3}$	1.14	2.5 $\times 10^{-3}$	1.54	1.6 $\times 10^{-3}$
GRT4 (W)	0.4	0.73	1.17	4.6 $\times 10^{-4}$	1.0	1 $\times 10^{-4}$	1.02	6 $\times 10^{-5}$

Notes: K_R = permeability ratio; k_{system} = system permeability; $\Psi_R = \Psi_{exhumed\ geotextile} / \Psi_{virgin\ geotextile}$; NA=Not analyzed

The permittivity ratios (permittivity of the post-GRT geotextile to that of virgin geotextile) for these geotextiles were 0.93 and 0.73 (lowest value of the two tests with no problems), respectively, indicating that the nonwoven and woven geotextiles have experienced only 7 and 27% reduction in their flow capacities, respectively. The permittivity ratio does not give any information about the changes in the system permeability or the compatibility of RCA and geotextile; however, it is a good indicator of the reduction in flow capacity of a geotextile. In theory, this ratio should be equal to one for a geotextile with no reduction in serviceability, indicating no change in flow capacity of the geotextile. In practice, to account for physical and biological clogging, when GRT tests are not conducted, the manufacturer's reported geotextile

permittivity is usually divided by a factor of safety of 2 to 10, which corresponds to a flow reduction of 50 to 90% respectively (Koerner 2012). The data in Table 2 is coming from the performance test where the reduction already occurs and based on the results, in this particular research the average reduction in flow is 7 and 27% for the nonwoven and woven geotextiles, respectively. These percent reductions correspond to mean permittivity ratios of 0.93 and 0.74, and thus mean hydraulic conductivities of 2.2×10^{-1} cm/s and 1.9×10^{-2} cm/s (range 0.019-0.22 cm/s) for the nonwoven and woven geotextiles, respectively. Considering that up to 50 to 90% reduction in permittivity is acceptable in practice, such a drop in permittivity should also be acceptable in filtration applications, as the clogged geotextile still has about 20-220 times higher hydraulic conductivity than that of a clean uniform sand ($K=1 \times 10^{-3}$ cm/s; Coduto et al. 2011).

A clear-cut trend was not observed when the permeability ratios were plotted versus permittivity or $AOS (O_{95})$ of the geotextile in contact with the geomaterial (Figure 4-22). This is somewhat consistent with the findings of Faure et al. (2000), Krug et al. (2000), and Aydilek and Edil (2003) who indicated that a combination of permittivity and pore structure parameters (i.e., porosity and pore size distribution) rather than a single hydraulic property is the main factor affecting the clogging performance of geotextiles. However, it should be emphasized that some of the previous studies analyzed natural soil-geotextile filters, and the observed inconsistency in this research program may also be attributed to the testing of an unusual geomaterial such as RCA.

Figures 4-23 and 4-24 present the temporal characteristics of permeability ratio and system permeability in RCA-geotextile systems for nonwoven and woven geotextiles, respectively. The time required for stabilization of flow under each hydraulic gradient ranged from 500 to 1300 hours. Similarly, Gabr and Akram (1996), Aydilek and Edil (2003), and Kutay and Aydilek (2005) indicated that a 24-hour procedure stated in the ASTM D 5101 is not sufficient, and long-term testing is required. As seen in Figures 3 and 4, for instance, two distinct flow patterns can be observed for RCA tested with nonwoven or woven geotextiles, similar to a behavior described by Gabr and Akram (1996) and Kutay and Aydilek (2005). A blocking/blinding pattern is observed at $i=5$ for the nonwoven geotextile. The hydraulic conductivity decreases slightly from 1.5×10^{-3} cm/s to 9×10^{-4} m/s and is accompanied by an increase in the gradient ratio from 1.7 to 3.1 in GRT1c. Similar behavior was observed for the same nonwoven geotextile in GRT1a. The hydraulic conductivity decreases from 4×10^{-3} cm/s to 8×10^{-4} m/s and is accompanied by an initial increase in the gradient ratio from 1.3 to 4, which stabilizes at 3.2.

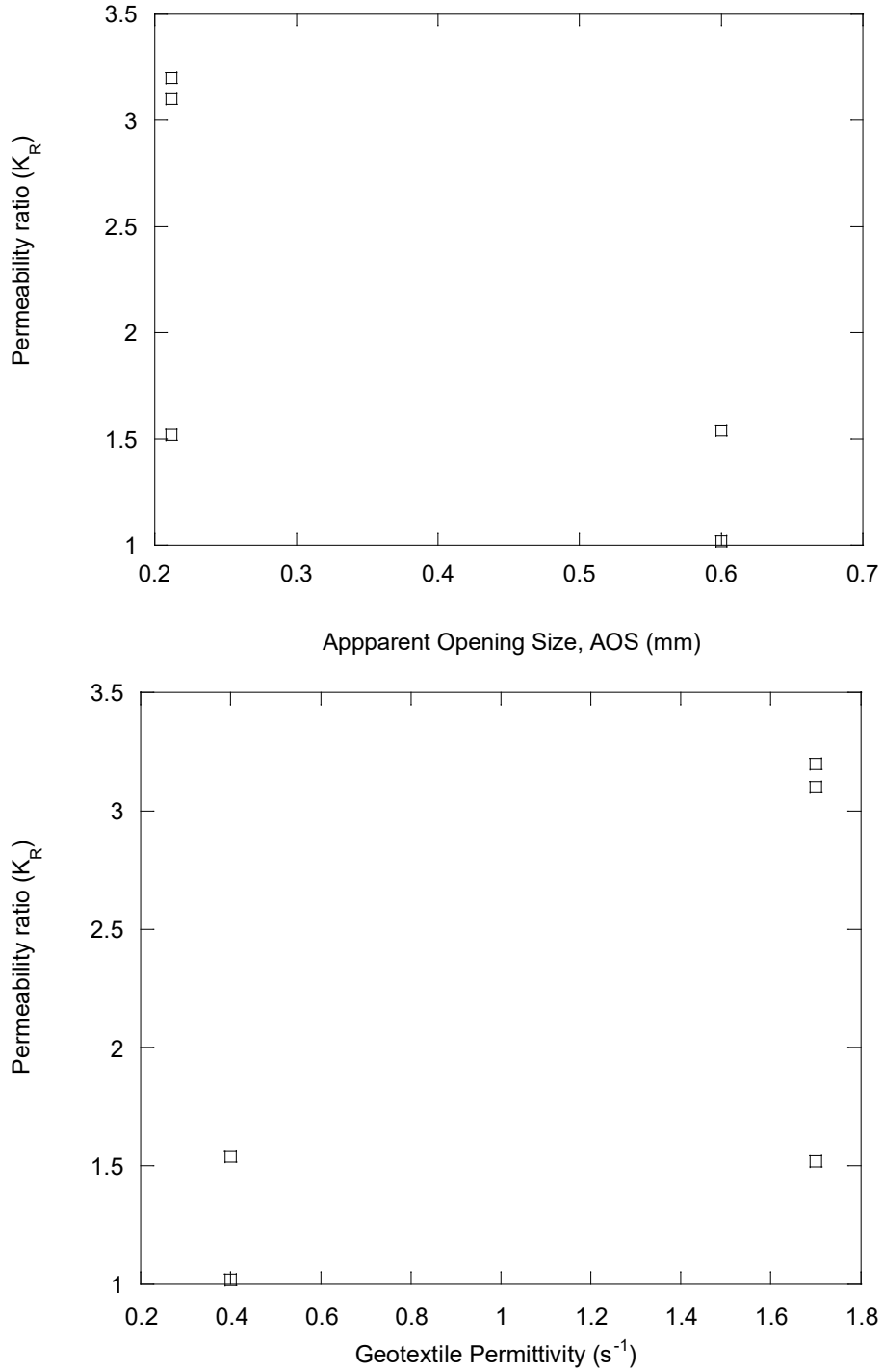


Figure 4.22. The effect of (a) apparent opening size, and (b) geotextile permittivity on calculated permeability ratios

A steady-state pattern is observed for the woven geotextile at $i=1$. A mixed behavior is apparent for the geotextiles at $i=2.5$ and $i=5$, in which occasional peaks in K_R are not necessarily

accompanied by the changes in system permeability. Rollin et al. (1985) has also observed similar flow patterns during long-term filtration tests and classified them into two distinct groups. Each group was defined by the following criteria: (1) normal behavior where soil particles move through geotextile increasing the density of the soil just above the geotextile thus reducing permeability; (2) mixed behavior where piping is followed by a particle blocking formation at the soil geotextile interface.

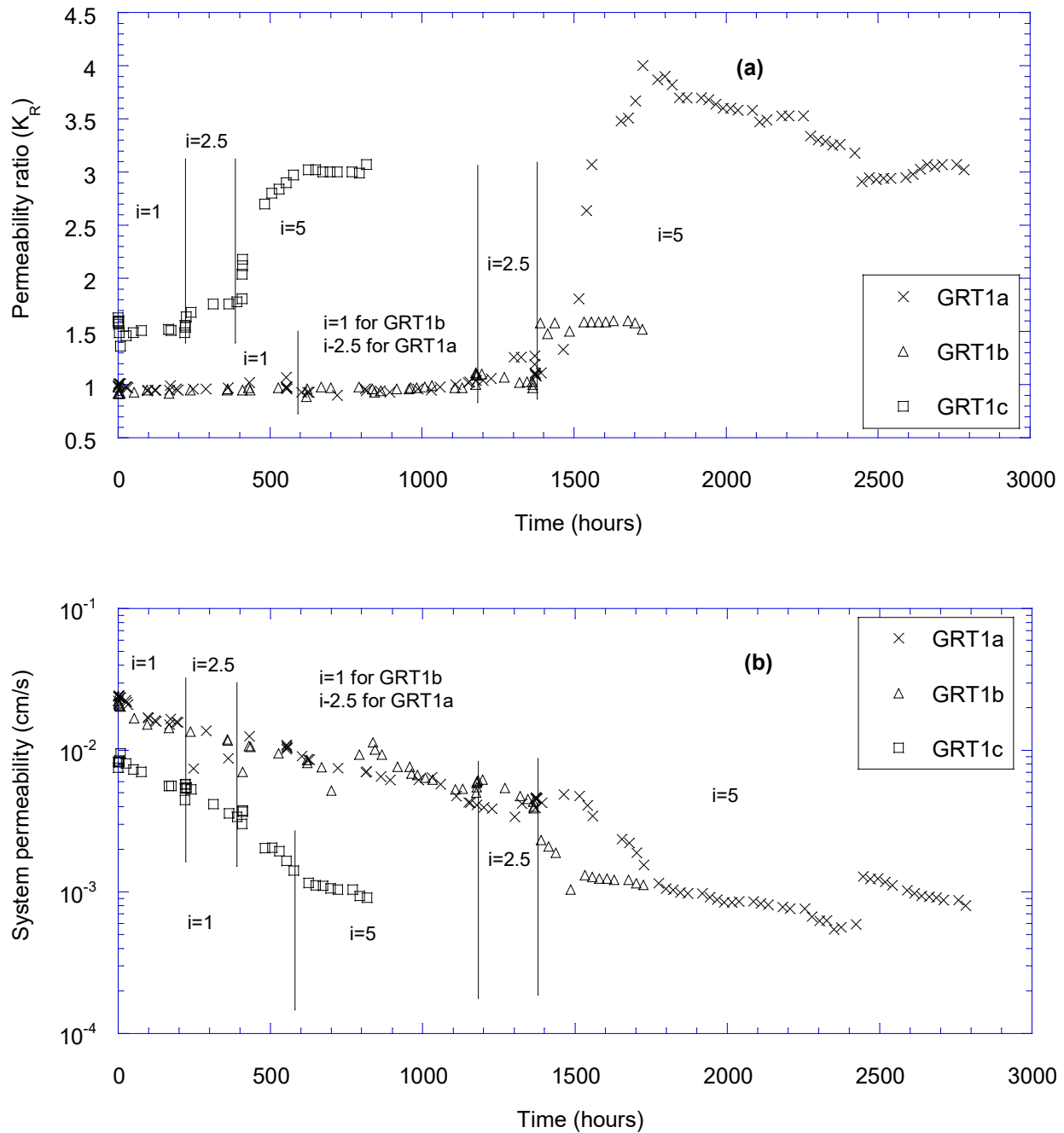


Figure 4.23. Temporal characteristics of (a) permeability ratio and (b) system permeability in RCA- nonwoven geotextile systems.

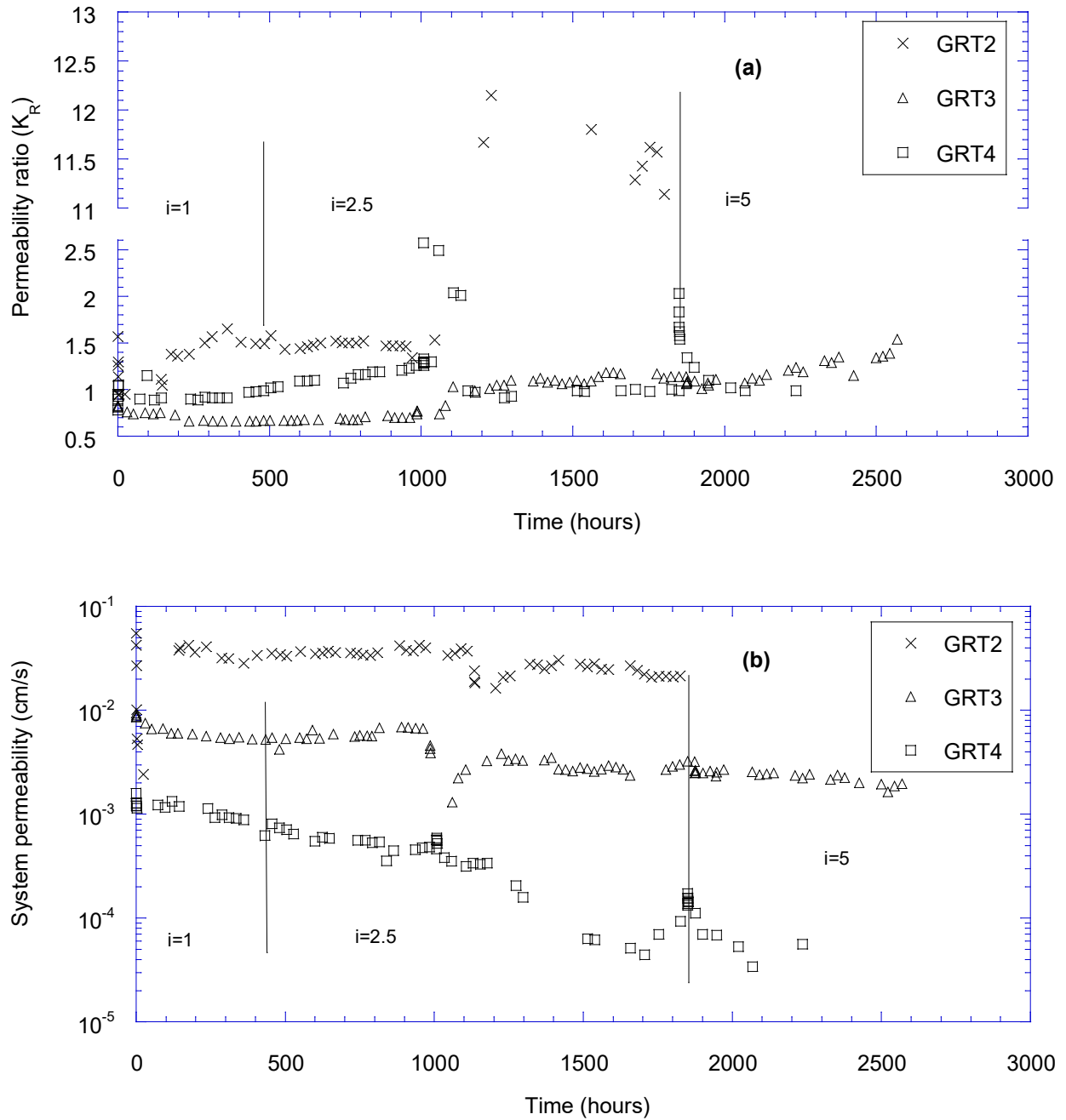


Figure 4.24. Temporal characteristics of (a) permeability ratio and (b) system permeability in RCA- woven geotextile systems.

4.6.2. Effect of Hydraulic Gradient on Clogging

Stabilized values of the permeability ratio and system hydraulic conductivity are plotted versus each applied hydraulic gradient in Figure 4-25. The effect of an increase of the hydraulic gradient seems to be pronounced on the K_R values. There is a gentle, but inconsistent increase in K_R with increasing hydraulic gradient. Similarly, the hydraulic conductivity decreases 2 to 15 times of its initial value when the hydraulic gradient is increased from 1 to 5. As it is seen from the figure, K_R are generally lower than the limit of 3, indicating that the geotextiles do not have a significant effect on the flow regime of the overall system.

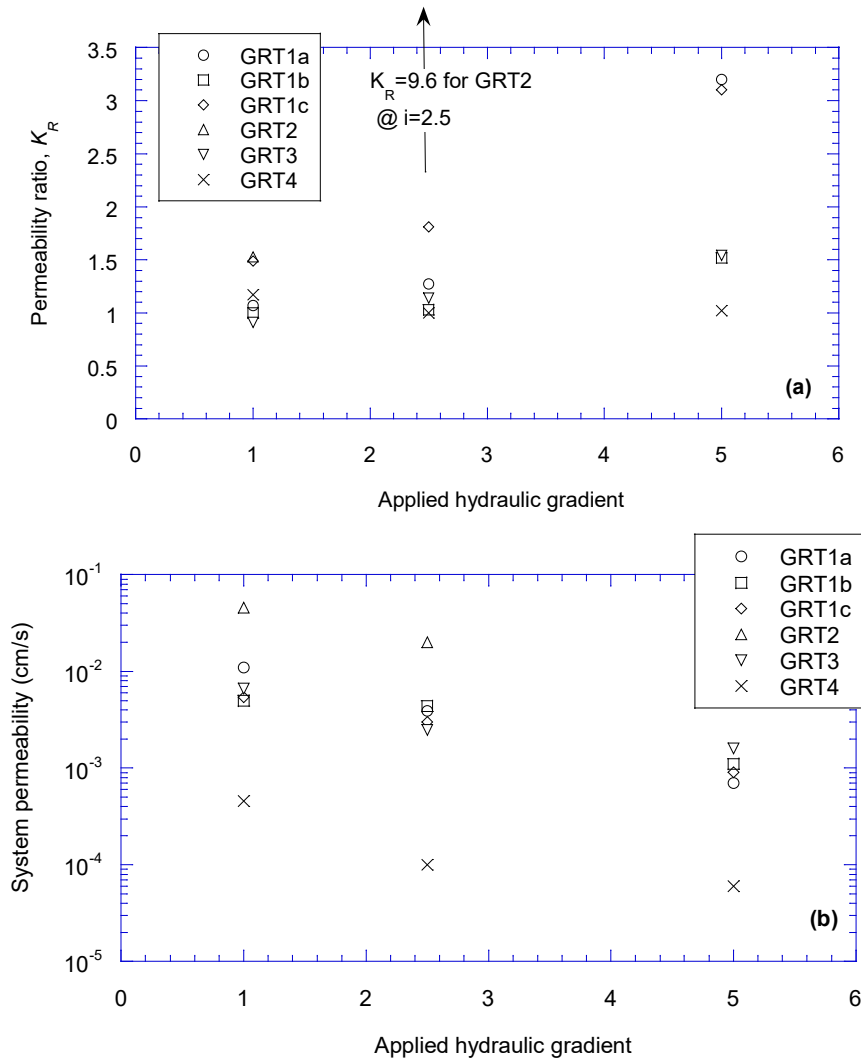


Figure 4.25. The effect of hydraulic gradient on (a) permeability ratio, and (b) system hydraulic conductivity of geotextiles exposed to filtration with RCA

4.6.3. Analyses of Retention Behavior

Gradient ratio tests also provided valuable information about retention performance of the geotextiles, since the material that piped through was continually monitored. The amount of piped soil from the nonwoven and woven geotextiles was about 2.0-2.6 g and 11-33 g, corresponding to piping rates of 111-144 g/m² and 611-1,833 g/m², respectively. This was lower than 2,500 g/m², a value generally used as an internal stability limit for granular and geotextile filters (Lafleur et al. 1989, Bhatia et al. 1998, Aydilek and Edil 2002, Kutay and Aydilek 2005). The agreement was also good with the findings of Gabr and Akram (1996) that the piped amount of material through geotextiles is insignificant. It is believed that the formation of a thin filter cake at the RCA-nonwoven geotextile interface or blocking at the RCA-woven geotextile contributed to the retention performance. Attempts made to measure the thickness of filter cakes indicated that the cake was too thin to measure. However, observations made for woven geotextiles during the filtration tests (Figure 4-23) along with the suggestions of Rollin et al. (1985) might provide additional evidence for the minimal piping associated with blocking.

In order to further investigate the formation of a graded filter zone above the geotextiles, post-gradient ratio test sieve analyses were performed on the RCA samples taken from different depths in the permeameters, and they were compared with the grain size distribution (GSD) of the RCA determined prior to testing. The plots that show the GSDs of the RCA samples collected from different depths inside the permeameter are given in Figures 4.26 and 4.27. GSD of the RCA-geotextile interface (94-100 mm) shifts to the right as compared to the GSD of the virgin material for the woven geotextiles, suggesting that accumulation of soil fines has occurred at the interface. No significant shift in other layers can be observed for the nonwoven geotextile. The shifts at the lower layers (i.e., 75-94 and 94-100 mm) are more pronounced for the woven than the nonwoven geotextile, which has experienced higher piping rates (611-1,833 g/m² versus 111-144 g/m²). These deviations are also supported by the K_R values for these two geotextiles calculated at their final hydraulic gradient ($i=5$; excluding GRT 2) (Table 4-11). The calculated K_R for the nonwoven ranges from 1.52 to 3.2, which indicates that the hydraulic conductivity of the entire system is, on average, two times lower than that of the soil. The ratio for the woven geotextile is 1.02-1.54. It is well known that material accumulation at the interface may prevent piping of excessive fines from the geotextile filter; however, it may also promote the clogging of the geotextile in the long-term by introducing a blinding zone at the soil-geotextile interface (Kutay and Aydilek 2005). These observations support the fact that use of a woven geotextile minimizes the development of fine accumulation at the soil-geotextile interface but may promote material loss, however, at acceptable levels.

Figure 4.28 shows the images of nonwoven geotextiles captured by the optical light microscope. The images clearly show the particle accumulation within the geotextiles. The accumulation is more clearly visible in the cross-sectional images. Figure 4-29 also shows that the surface of the woven geotextile was blocked with particles upon filtration with RCA. Figure 4-30 shows that pore size distribution of the virgin nonwoven geotextile changed significantly during the particle accumulation. Characteristic pore opening sizes (e.g., O_{95} , O_{60} , O_{50} , O_{40} , O_{30} , O_{15} , and O_{10}) of the post-GRT geotextile were decreased in all cases. Modest decrease is observed in pore size distribution of the woven geotextile (Figure 4-31) as the particle accumulation is on the surface (i.e., blocking) rather than intrusion of the particles into pore channels as experienced by the nonwoven. The three characteristic pore sizes typically employed in the existing filter selection

criteria, O_{95} , O_{50} , and O_{30} , decrease by 30-33%, 24-28%, and 22%, respectively. The reduction percentages are 29-31%, 2-5% and 5%, respectively, for the same characteristic pore sizes of the woven geotextile. Despite many of the existing clogging criteria that use the apparent pore size of the geotextile (O_{95}) due to its availability, studies indicate that changes in smaller pore sizes (i.e., $O_{40} - O_{50}$) rather than larger ones (e.g., $O_{95} - O_{95}$) are better indicators of clogging (Bhatia et al. 1996, Aydilek and Edil 2002, Aydilek 2006). These measurements are in parallel with the observations made in the long-term laboratory

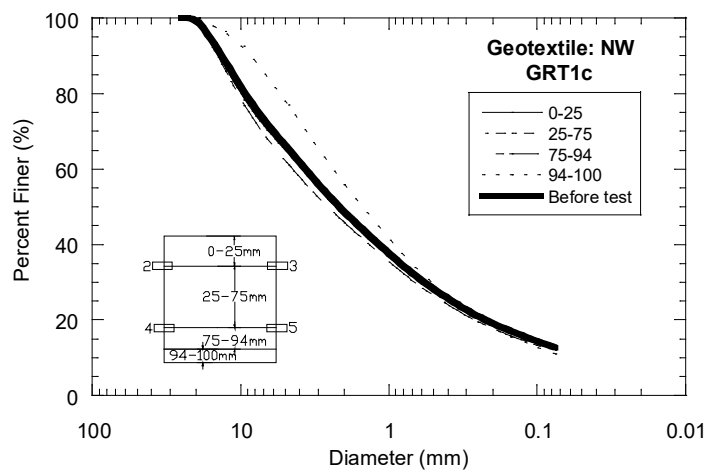
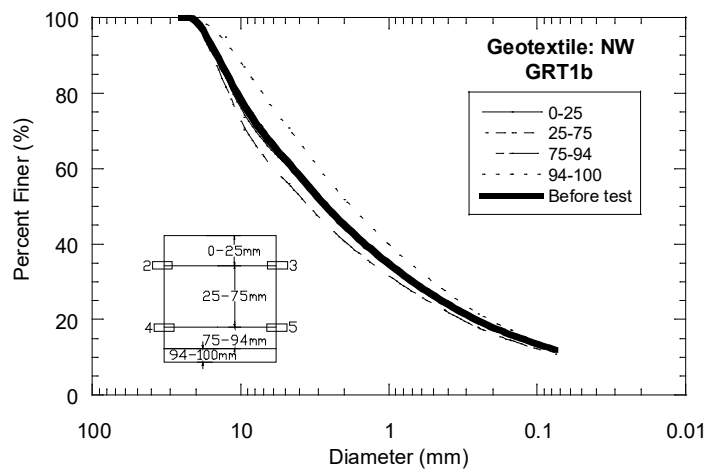
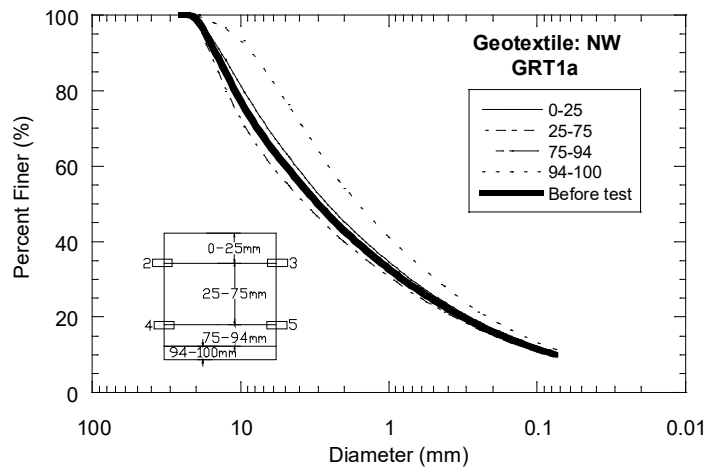


Figure 4.26. Changes in grain size distribution (GSD) of RCA exposed to filtration with nonwoven and woven geotextiles.

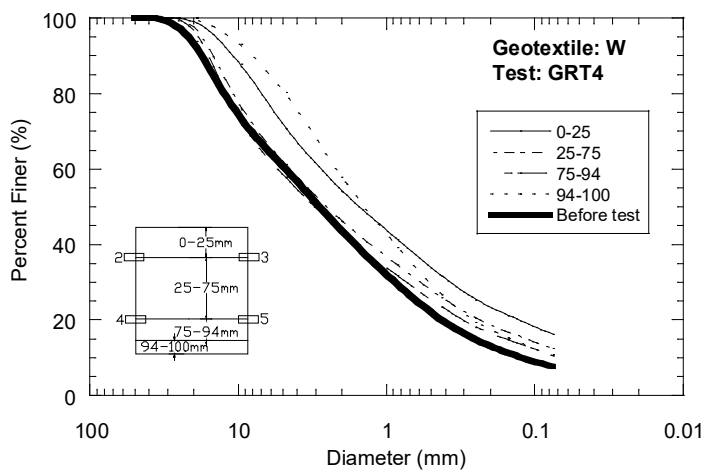
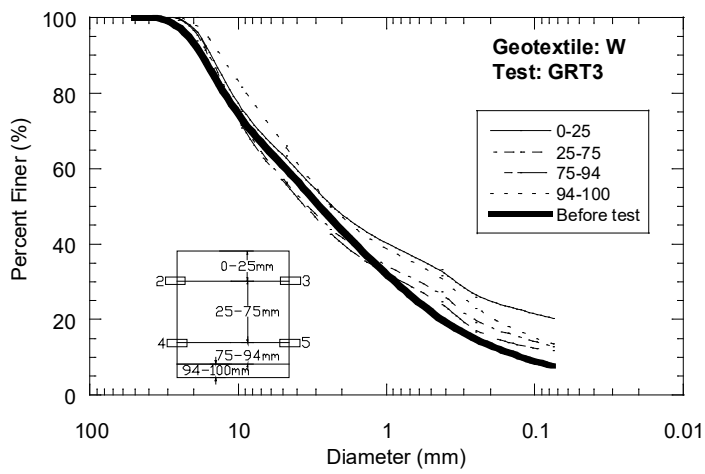
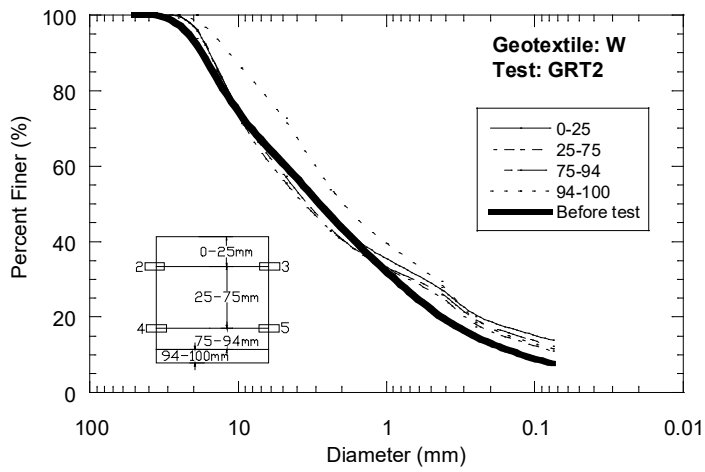
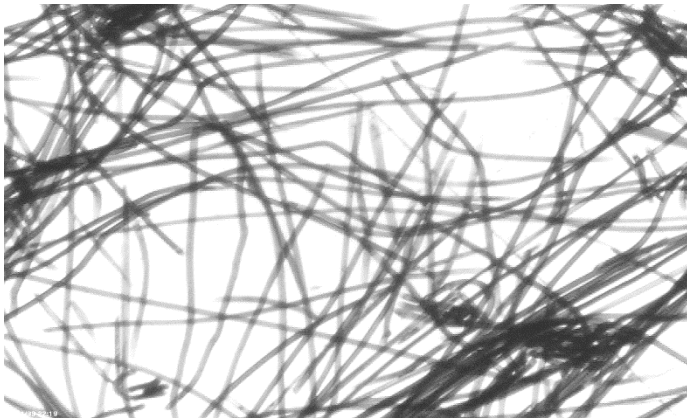
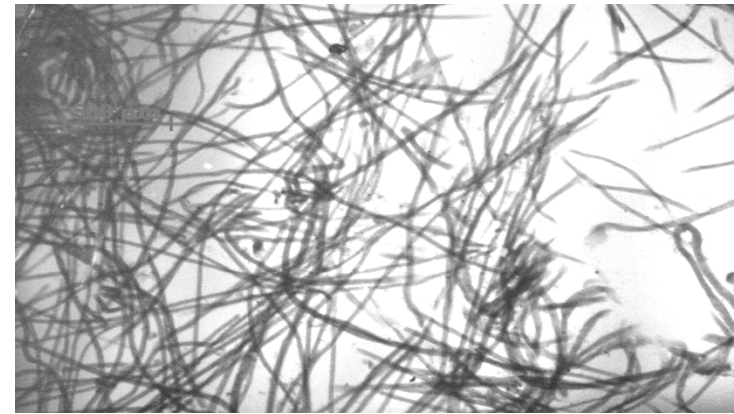


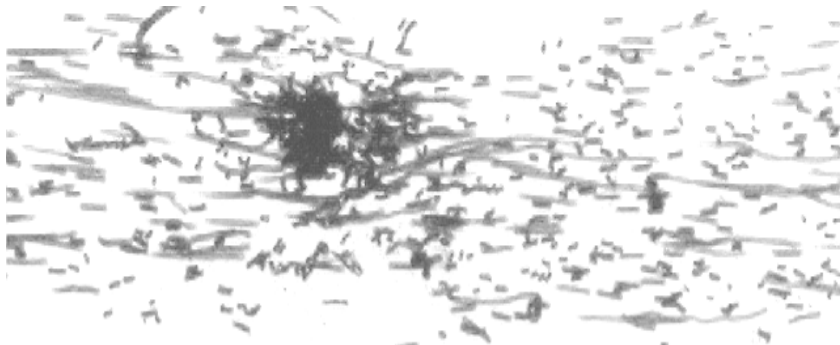
Figure 4.27. Changes in grain size distribution (GSD) of RCA exposed to filtration with woven geotextile.



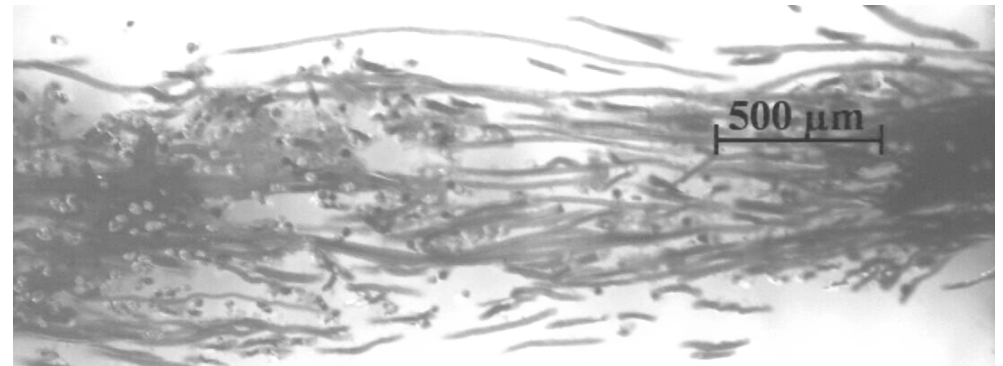
(a)



(c)

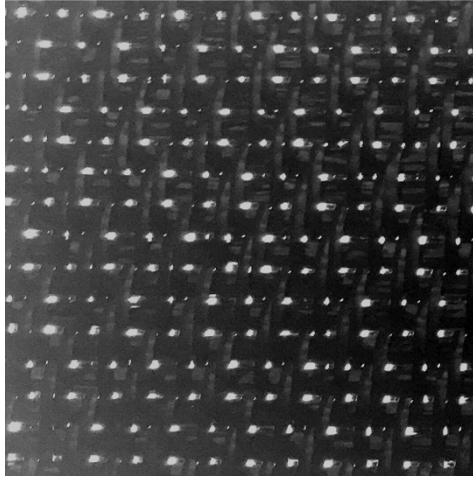


(b)

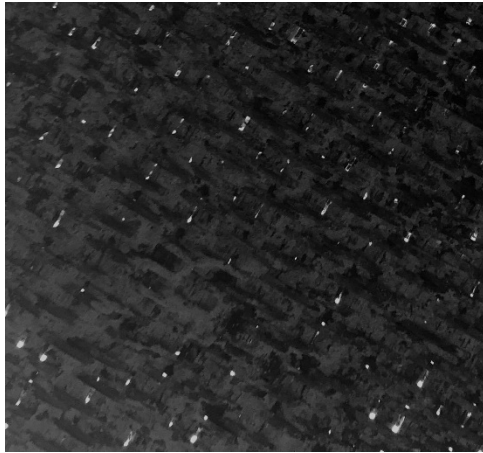


(d)

Figure 4.28. (a) Planar and (b) cross-sectional images of a virgin, and (c) planar and (d) cross-sectional images of post-gradient ratio test specimens of the nonwoven geotextile (Magnification = 2.5X for planar images and 5X for cross-sectional images).



(a)



(b)



(c)

Figure 4.29. Images of woven geotextile: (a) virgin, and from (b) GRT2, and (c) GRT3.

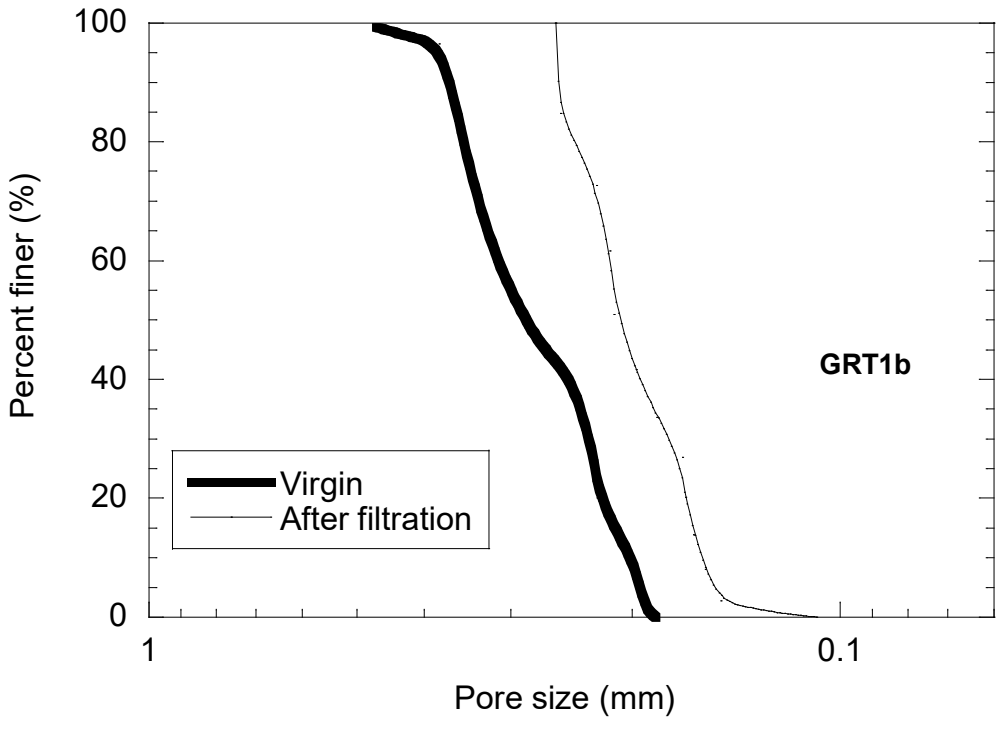
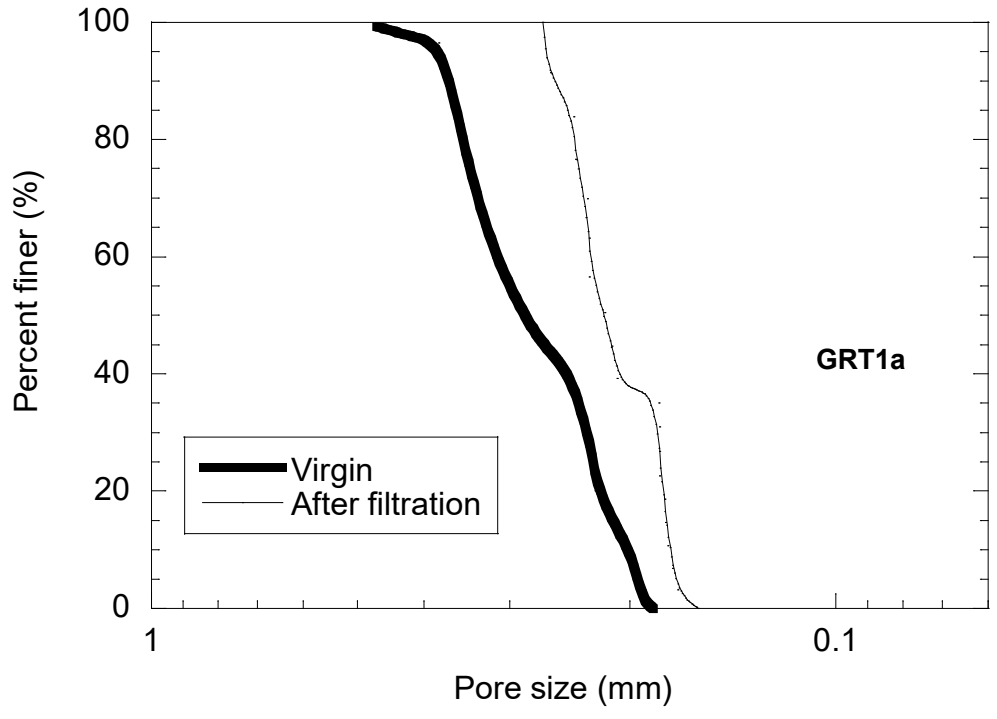


Figure 4.30. Changes in pore size distribution (PSD) of the nonwoven geotextile filtering RCA

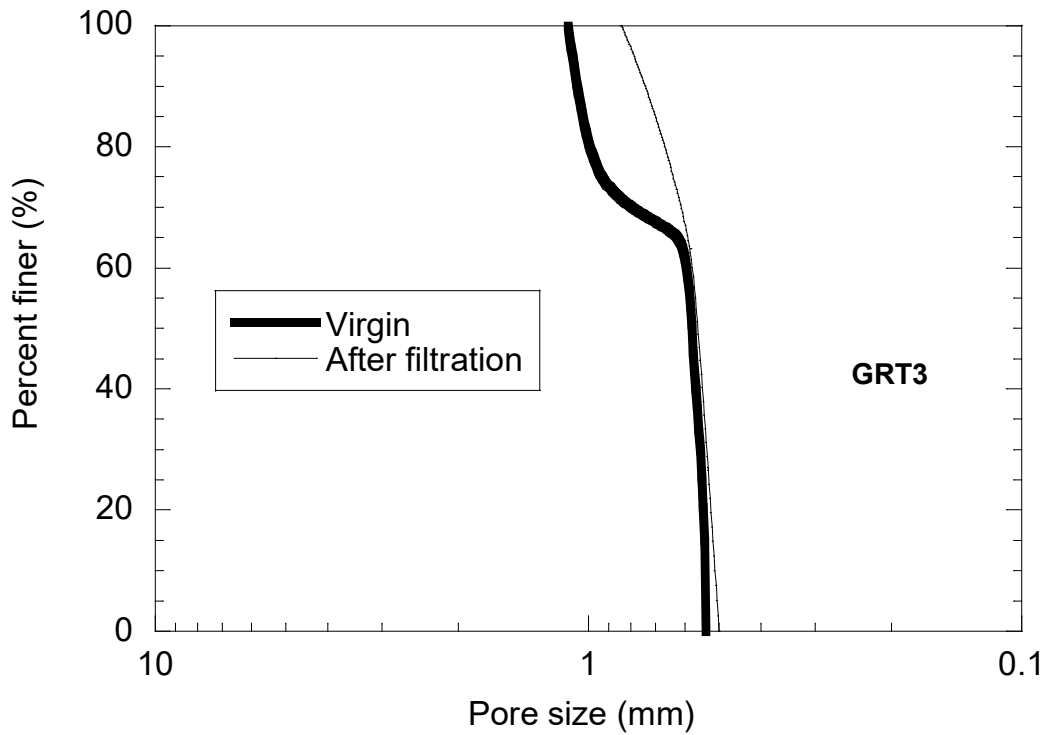
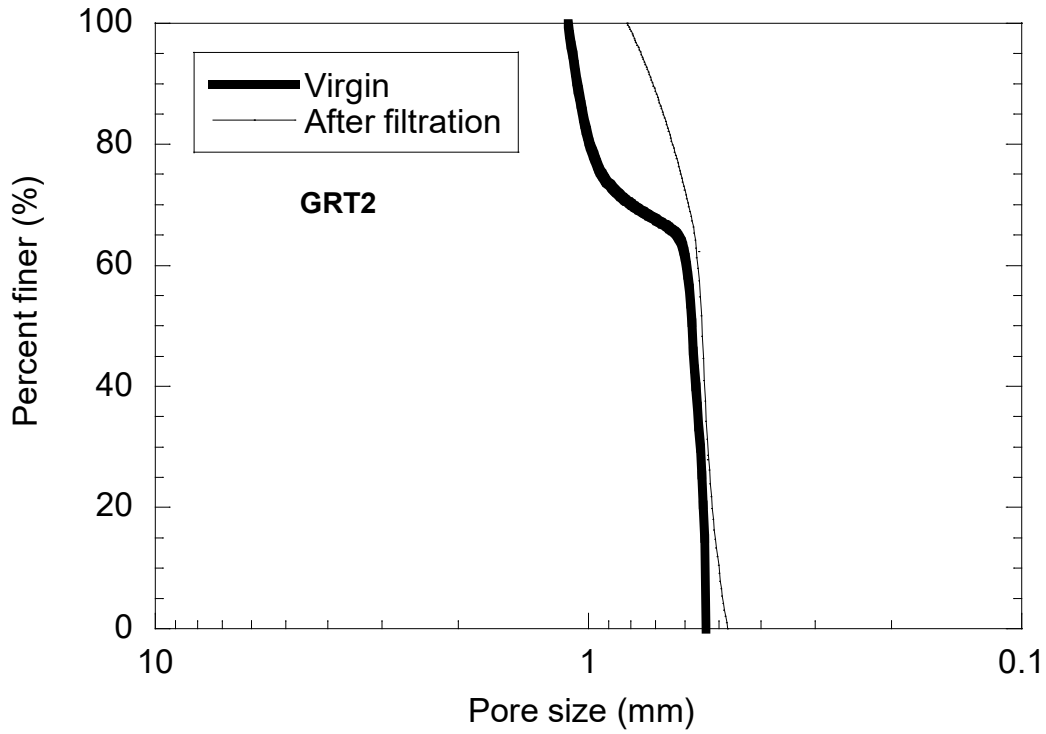


Figure 4.31. Changes in pore size distribution (PSD) of the woven geotextile filtering RCA.

Filtration tests (Table 4-11) that the woven geotextile used in the current study is less likely to experience clogging than the nonwoven when tested with RCA.

5. Conclusions and Recommendations

In this study mechanical and hydraulic properties of RCA and RAP for use in Mechanically Stabilized Earth (MSE) walls were evaluated. For mechanical properties, direct shear tests were conducted to evaluate the interaction properties of RAP and RCA with woven and non-woven geotextiles and uniaxial and biaxial geogrids. Pull-out tests were conducted to evaluate pull-out resistance of woven geotextile and uniaxial geogrids embedded in compacted RAP and RCA. Since RAP particles contain asphalt binder coating, RAP specimens were compacted at elevated temperatures (35 °C-50 °C) to evaluate the effects of compaction temperature on interaction properties of compacted RAP and geosynthetics. Temperature-controlled triaxial compression tests under sustained deviator stresses were also conducted to evaluate shear creep response of compacted RAP at different temperatures.

Results show that compacted RAP and RCA provide competitive pull-out resistance for woven geotextiles and uniaxial geogrids compared to compacted natural granular materials. No slippage was observed and the failure was due to the rupture of geotextile or geogrid. The interface friction angle (δ) of RCA-Woven Geotextile was 26° and that of RCA-Nonwoven Geotextile was 19°. The δ of RCA-Uniaxial Geogrid was 36° and that of RCA-Biaxial Geogrid was 32°. Test results indicate that RCA has competitive interface friction with woven geotextiles, uniaxial and biaxial geogrids used in this study. Results of direct shear tests on compacted RAP at room temperature show that δ for RAP-Woven Geotextile was 25° and that of RAP-Nonwoven Geotextile was 17°. The δ of RAP-Uniaxial Geogrid was 32° and that of RAP-Biaxial Geogrid was 40°. Based on the results, use of non-woven geotextile for MSE wall reinforcement is not recommended. Compaction of RAP at elevated temperatures did not render consistent effects on δ . However, the δ for RAP-Geosynthetics due to compaction at varying temperatures changed in a narrow range. The standard deviation of δ due to compaction temperatures between 22 °C and 50 °C varied from 1.4° for RAP-Woven Geotextile to 3.8° for RAP-Uniaxial Geogrid.

Recycled asphalt pavements have classical creep behavior similar to soils with the axial strain rate log-linearly decreases with time. When compacted at room temperature, the upper yield strength below which the creep rupture is unlikely to occur is estimated to be about 0.70. Compacted RAP used as backfill is susceptible to creep rupture and the maximum applied deviator stress on the compacted RAP should be reduced to 70% of the compressive strength to alleviate the problems related to creep. With increasing temperature, creep strain and strain rate for the compacted RAP increased and the time to rupture decreased. The creep behavior of RAP at elevated temperatures followed the classical creep behavior in that the strain rate log-linearly decreased with time until the initiation of creep rupture when the strain rate started to increase. The volumetric change during creep test became more compressive at elevated temperatures. Shear strength of RAP increased after compaction and consolidation at elevated temperatures. Compaction and consolidation at elevated temperatures also reduced the strain rate and creep susceptibility of the compacted RAP under constant deviator stress. Axial strain rate in log scale linearly varied with compaction or creep temperatures. The slope of the lines termed as

coefficient of thermal creep was independent of the elapsed time. The creep strain rate exponentially varied with temperature. Construction of a structural fill containing RAP is recommended to be undertaken during summer to reduce the creep strain and creep rupture potential and improve performance of the fill. Construction of the structural fill containing RAP during the cold season is not recommended due to expected increase in creep strain at elevated temperatures of the subsequent seasons.

A battery of laboratory long-term gradient ratio tests was conducted to evaluate the filtration performance of the woven geotextile. RCA can be filtered with geotextiles; however, interpretation of the data should be made carefully. The permeability ratio (K_R) derived from long-term filtration tests allows a clearer definition of clogging. A detailed analysis of clogging ratios, changes in geotextile permittivity and pore size, as well as size variations at the interface support the information brought by (K_R) that physical clogging of a woven geotextile by RCA is minimal.

REFERENCES

- ACAA (American Coal Ash Association). (2015). About Coal Ash, What are CCPs ?, Fly Ash. Retrieved July 27th, 2015 from: <http://www.acaa-usa.org/About-Coal-Ash/What-are-CCPs/Fly-Ash>
- Abdelouhab, A., Dias, D., Freitag, N. (2010). Numerical Analysis of the Behavior of Mechanically Stabilized Earth Walls Reinforced with Different Types of Strips. doi:10.1016/j.geotexmem.2010.10.011. Elsevier Ltd.
- Abichou, T., Edil, T., Benson, C. (2004). “*Beneficial Use of Foundry By-Products in Highway Construction*”. Geo Trans 2004. Geotechnical Engineering for Transportation Projects. ASCE 715-722
- Abu-Farsakh, M., Coronel, J., (2006). “*Characterization of Cohesive Soil–Geosynthetic Interaction from Large Direct Shear Test*”. 85th Transportation Research Board Annual Meeting, Washington, D.C
- AFS (American Foundry Society). (n.d.). Introduction to Foundry Sand. Retrieved July 20th, 2015 from: <http://www.afsinc.org/content.cfm?ItemNumber=7075>
- Anderson, K. W., Uhlmeier, J. S., Russell, M. (2009). “*Use of Recycled Concrete Aggregate in PCCPs: Literature Search*”. (June), 35: Washington Department of transportation, Office of Research & Library Services.
- Anderson, P., Gladstone, R., Sankey, J. (2012). “*State of the Practice of MSE Wall Design for Highway Structures*”. *Geotechnical Engineering State of the Art and Practice*, 1–21. doi:10.1061/ 9780784412138.0018
- ARRA (Asphalt Recycling and Reclaiming Association). (2001). *Basic Asphalt Recycling Manual*. (Vol. 1)
- AASHTO (American Association of State Highway and Transportation) (2010). LRFD Bridge Design Specifications, 5th Edition, American Association of State Highway and Transportation Officials, Washington, DC Officials, Washington, DC.
- ASTM, D 1557 (2003). “Standard Test Methods for Laboratory Compaction Characteristics of Soil Using Modified Effort.” American Society for Testing and Materials, West Conshohocken, Pennsylvania, USA.
- ASTM D 4491 (2003). “Test Methods for Water Permeability of Geotextiles by Permittivity”, American Society for Testing and Materials, West Conshohocken, Pennsylvania, USA.
- ASTM, D 4751 (2003). “Test Method for Determining the Apparent Opening Size of a Geotextile”, American Society for Testing and Materials, West Conshohocken, Pennsylvania, USA.

- ASTM D 5101 (2003). "Standard Test Method for Measuring the Soil-Geotextile System Clogging Potential by the Gradient Ratio", American Society for Testing and Materials, West Conshohocken, Pennsylvania, USA.
- Aydilek, A. H. and Edil, T.B., (2002). "Filtration Performance of Woven Geotextiles with Wastewater Treatment Sludge." *Geosynthetics International*, IFAI, Vol. 9, No. 1, pp. 41-69.
- Aydilek, A. H., and Edil, T.B., (2003). "Long-Term Filtration Performance of Nonwoven Geotextile-Sludge Systems", *Geosynthetics International*, IFAI, Vol. 10, No. 4.
- Aydilek, A. and Mijic, Z. (2015). "*Hydraulic and Environmental Behavior of Roadway Millings in Highway Shoulder Applications*". Environmental Geotechnics Report 15-8, University of Maryland, College Park, MD.
- Akram, M. H., Gabr, M. A., (1997). "Filtration of Fly Ash Using Non-Woven Geotextiles; Effect of Sample Preparation Technique and Testing Method", *Geotechnical Testing Journal*, ASTM, Vol. 20, No. 3, pp. 263-271.
- Allen, T., Christopher, B., Elias, V., DiMaggio, J. (2001) "*Development of the Simplified Method for Internal Stability Design of Mechanically Stabilized Earth Walls*". Technical Report, WA-RD 513.1, Washington State Department of transportation.
- Basma, A., Tuncer, E. (1992). "*Evaluation and Control of Collapsible Soils*". *Journal of Geotechnical Engineering*. ASCE 1992.118:1491.-1504.
- Basudhar, P., Vashistha, A., Deb, K., Dey, A. (2006). "*Cost Optimization of Reinforced Earth Walls*". *Sprinter-Science*. doi:10.1007/s10706-007-9143-6
- Bhatia, S.K., Moraille J., and Smith J.L., (1998). "Performance of Granular versus Geotextile Filters in Protecting Cohesionless Soils", *Filtration and Drainage in Geotechnical and Geoenvironmental Engineering*, ASCE, Geotechnical Special Publication 78, L.N. Reddi and M.V.S. Bonala, Eds., pp. 1-29.
- Benson, C., Tinjum, J., Nokkaew, K. (2012). "*Hydraulic Properties of Recycled Asphalt Pavements and Recycled Concrete Aggregate*". *GeoCongress*, ASCE 2012
- Berg, R., Christopher, B., & Samtani, N. (2009). "*Design and Construction of Mechanically Stabilized Earth Walls and Reinforced Soil Slopes–Volume I*". *Federal Highway Administration (FHWA)*.
- Bilgin, O., Mansur, E. (2014). "*Effect of Reinforcement Type on the Design Reinforcement Length of Mechanically Stabilized Earth Walls*". *Elsevier. Engineering Structures* 59 (2014) 663-673

- Bleakley, A., Cosentino, P., Kalajian, E., & Patel, M. (2014). *“Strength and Creep Characteristics of RAP-Sand Blend Backfill in Mechanically Stabilized Earth Walls”*. (July 2013). Transportation Research Board, Transportation Research Record. TRB Annual Meeting. (2014).
- Bose, Bidula. (2012) *“Geo-Engineering Properties of Expansive Soil Stabilized with Fly Ash”*. Electronic journal of Geotechnical Engineering, Volume 17.
- Bruinsma, J., Peterson, K. Snyder, M. (1997). *“Chemical Approach to Formation of Calcite Precipitation from Recycled Concrete Aggregate Base Layers”*. Transportation Research Record 1577, Paper No. 971154, pp 10-17.
- Butler, L., Wets, J., Tighe, S. (2011). *“Quantification of Recycled Concrete Aggregate (RCA) Properties for Usage in Bridges and Pavement: An Ontario Case Study”*. 2011 Annual Conference of the Transportation Association of Canada: Innovative Developments in Sustainable Pavement Session, Edmonton, Alberta.
- Caltrans (California Department of Transportation). (2004). California Department of Transportation, Bridge Design Specifications, Section 5 – Retaining Walls.
- Cancelli, A., Rimoldi, P., Togni, S., (1992). *“Frictional Characteristics of Geogrids by Means of Direct Shear and Pull-out Tests”*. Proceedings of the International Symposium on Earth Reinforcement Practice, Kyushu, vol. 1, pp. 29–34.
- Cazzuffi, D., Picarelli, L., Ricciuti, A., Rimoldi, P., (1993). *“Laboratory investigations on the shear strength of geogrid reinforced soils”*. ASTM Special Technical Publication 1190, 119–137
- Chalermyanont, T., & Benson, C. H. (2004). *“Reliability-Based Design for Internal Stability of Mechanically Stabilized Earth Walls”*. *Journal of Geotechnical and Geoenvironmental Engineering*, 130(February), 163–173. doi:10.1061/(ASCE)1090-0241(2004)130:2(163)
- CDRA (Construction & Demolition Recycling Association) (n.d.). *“Markets for Recycled Concrete Aggregate”*. Retrieved July 30th, 2015 from: <http://www.cdrecycling.org/end-markets>
- CDRA (Construction & Demolition Recycling Association) (n.d.). *“Asphalt Roofing Shingles Recycling: Introduction”*. Retrieved Aug 2nd, 2015 from: <http://www.shinglerecycling.org/content/markets-recycling-asphalt-shingles>
- Cosentino, P. J., Kalajian, E. H., & Ho, R. K. (2001). Final Report - Developing Specifications for Using Recycled Asphalt Pavement as Base, Subbase or General Fill Materials.
- CWC (Clean Washington Center) (n.d.). *“Beneficial Use of Spent Foundry Sand”*. Retrieved Aug 3rd, 2015 from: <http://www.cwc.org/industry/ibp951fs.pdf>

- Das, B. (2007). *Principles of Foundation Engineering* (7th edition, pp. 406 – 436). Stamford, CT: Cengage Learning
- Edil, T.B., Tinjum, J. M., and Benson, C. H. (2012) Final Report - Recycled Unbound Materials, Technical Document, Report No. MN/RC 2012-35, Minnesota Department of Transportation.
- Elias, V., Christopher, B., & Berg, R. (2001). “*Mechanically Stabilized Earth Walls and Reinforced Soil Slopes Design & Construction Guidelines*”. *Construction*, (132042). doi:FHWA-NHI-10-024 & FHWA-NHI-10-025
- Elias, V., Fishman, K., Christopher, B., & Berg, R. (2009). *NHI Courses No. 132042 and 132043 CORROSION / DEGRADATION OF SOIL REINFORCEMENTS FOR. U.S Department of Transportation Federal Highway Administration.*
- EPA (United States Environmental Protection Agency). (n.d.). Retrieved January 22th, 2015, from: <http://www.epa.gov/climate/climatechange/wycd/waste/downloads/concrete-chapter10-28-10.pdf>
- Fannin, R.J., Vaid, Y.P., and Shi, Y.C., (1994). “Filtration Behavior of Nonwoven Geotextiles”, *Canadian Geotechnical Journal*, Vol.31, pp. 555-563.
- Faure Y.H., Kehila, Y., Olivier F., and Paillez, S., (2000). “Behavior of Nonwoven Geotextiles for Filtrating Particles in Suspension”, *Filters and Drainage in Geotechnical and Geoenvironmental Engineering*, W. Wolski and J. Mlynarek, eds., Balkema, Rotterdam, The Netherlands, pp. 59-66.
- FHWA (Federal Highway Administration Agency). (1997). “*User Guideline for Waste and Byproduct Materials in Pavement Construction*”. Report. Publication number: FHWA-RD-97-148. Retrieved July 28th 2015 from: <http://www.fhwa.dot.gov/publications/research/infrastructure/structures/97148/fs1.cfm>
- FHWA (Federal Highway Administration Agency). (2004a). “*Transportation Applications of Recycled Concrete Aggregate*”. FHWA State of the Practice National Review. U.S. Department of Transportation Federal Highway Administration.
- FHWA (Federal Highway Administration Agency). (2004b). “*Fly Ash Finds Multiple Uses in Highway Construction*”. *Technical Report*. U.S. Department of Transportation Federal Highway Administration. FHWA-IF-04-004
- FHWA (Federal Highway Administration Agency). (2004c). “*Foundry Sand Facts for Civil Engineers*”. *FOCUS*, Accelerating Infrastructure Innovations. U.S. Department of Transportation Federal Highway Administration. FHWA-HRT-04-024

- Fowler, J., Bagby, R., and Trainer, E., (1996). "Dewatering Sewage Sludge with Geotextile Tubes" Proceedings of the 49th Canadian Geotechnical Conference, St. John's, New Foundland, Canada, 30 p.
- Gabr, M. A., and Akram, M. H., (1996). "Clogging and Piping Criteria for Geotextile Filters for Fly Ash", Proceedings of the 3rd International Symposium on Environmental Technology, San Diego, California, USA, pp. 836-847
- Gautreau, G., Abu-Farsakh, M, Zhang, Z. (2009). "*Bottom Ash Test and Evaluation*". *Technical Assistance Report #: 08-3TA, Louisiana Transportation Research Center.*
- Goodhue, M., Edil, T., Benson, C. (2001). "*Interaction of Foundry Sands with Geosynthetics*". *Journal of Geotechnical and Geoenvironmental Engineering / April 2001, 353-362*
- Giroud, J.P., (1996). "Granular Filters and Geotextile Filters." Proceedings of Geofilters '96, Montreal, QB, Canada, pp. 565-680.
- Giroud, J.P., Delmas, P., and Artières, O., (1998). "Theoretical Basis for the Development of a Two-Layer Geotextile Filter" Proceedings of the Sixth International Conference on Geosynthetics, Atlanta, Georgia, USA, pp. 1037-1044.
- Griffiths, C., Krstulovich, J. (2002). "*Utilization of Recycled Materials in Illinois Highway Construction*". Illinois Department of Transportation. Bureau of Materials and Physical Research, Report No. 142. Springfield, Illinois.
- Gutt, W., Nixon, P. (1979). "*Use of Waste Materials I the Construction Industry*". Analysis of the RILEM Symposium by Correspondence. BORDAS-DUNOD 0025-5432/1979/255
- Holtz, R., Christopher, B., Berg, R. (1998). "*Geosynthetic Design and Construction Guideline*". Participant notebook. Pdf. Publication no. FHWA HI-95-038. Course no. 13213. National Highway Institute.
- Huang, W. (1990). "*The Use of Bottom Ash in Highway Embankments, Subgrades and Subbases*". *Joint Highway Research Project, Final Report, FHWA/IN/JHRP-90/4*
- Juan, M., Gutierrez, P. (2009). "*Study on the Influence of Attached Mortar Content on the Properties of Recycled Concrete Aggregate*". *Construction and Building materials. Elsevier 23(2009) 872-877.*
- Kim, H., Lee, H. (2014) "*Coal Bottom Ash in Field of Civil Engineering: A Review of Advanced Applications and Environmental Considerations*". *KSCE Journal of Civil Engineering. Springer. doi:10.1007/s12205-015-0282-7*
- Koerner, R. (1994). *Designing with Geosynthetics* (3rd edition.). Prentice-Hall. Englewood Cliffs, NJ

- Koerner, R. (2000). *“Emerging and Future Developments of Selected Geosynthetic Applications.”* Journal of Geotechnical and Geoenvironmental Engineering, ASCE 126(4), 293-306
- Koerner, R. (2005). *Designing with Geosynthetics* (5th edition.). Prentice-Hall. Englewood Cliffs, NJ
- Koerner, R. (2009). *“An Overview of Geogrids”*. Jubilee Symposium on Polymer Geogrid Reinforcement. London, United Kingdom.
- Krug, M., Heyer, D., and Floss, R., (2000). “Filtration Effectiveness of Geotextiles in Cover Sealing Systems of Landfills”, *Filters and Drainage in Geotechnical and Geoenvironmental Engineering*, W. Wolski and J. Mlynarek, eds., Balkema, Rotterdam, The Netherlands, pp. 271-278.
- Kumar, B., Sharma, R. (2004). Journal of Geotechnical and Geoenvironmental Engineering, ASCE / July 2004, 764-767, doi:10.1061/(ASCE) 1090-0241 (2004) 130:7(764)
- Kuo, S., Mahgoub, H., Naef, A. (2002). *“Investigation of Recycled Concrete Made with Limestone Aggregate for a Base Course in Flexible Pavement”*. Transportation Research Record 1787. Paper No. 02-3098, 99-108.
- Kutay, M.E. and Aydilek, A.H., (2003). “Hydraulic Performance Of Geotextile Containers Confining Waste Materials”, Environmental Geotechnics Report, 03-02, University of Maryland, College Park, USA, 130 p.
- Lafleur, J., Mlynarek, J., and Rollin, A.L., (1989). “Filtration of Broadly Graded Cohesionless Soils”, Journal of Geotechnical Engineering, ASCE, Vol. 115, No. 12, pp. 1747-1768.
- Liu, C., Ho, Y., Huang, J. (2009). *“Large Scale Direct Shear Test of Soil/PET-yarn Geogrid Interface”*. Geotextiles and Geomembranes, Elsevier, doi:10.1016/j.geotexmem.2008.03.002
- Mallick, S., Zhai, H., Adanur, S., Elton, D. (1996). *"Pull-out and direct shear testing of geosynthetic reinforcement: state-of-the-art report."* Transportation Research Record, Vol. 1534, 80-90.
- Maxwell, S., Kim, W., Edil, T. B., & Benson, C. H. (2005). Effectiveness of Geosynthetics in Stabilizing Soft Subgrades. Report no. 0092-45-15.
- Muethel, R. (1989). *“Calcium Carbonate Precipitate from Crushed Concrete”*. Research Laboratory Section, Materials and Technology Division, Research Project 87 TI-1276, Research Report No. R-1297, Michigan Transportation Commission,
- Muethel, R. W. Calcium Carbonate Precipitate from Crushed Concrete. Michigan Department of Transportation, Lansing, March 1989.

- NAPA (National Asphalt Pavement Association). (2014). Annual Asphalt Pavement Industry Survey on Recycled Materials and Warm-Mix Asphalt Usage: 2009-2013.
- NAS (National Academy of Science). (2006). Managing Coal Combustion Residues in Mines, “Coal Combustion Residues” 27-38. <http://www.nap.edu/catalog/11592.html>
- Nejad, M., Small, J. (2005). “*Pull-out Behavior of Geogrids*”. Iranian Journal of Science & Technology, Transaction B, Engineering, Vol. 29, No. B3. Shiraz University.
- NYDOT (New York State Department of Transportation). (2007) “Mechanically Stabilized Earth System Inspection Manual.” Geotechnical Engineering Manual-GEM-16, Revision #2, Geotechnical Engineering Bureau, EB 07-039
- ODNR (Ohio Department of Natural Resources) (n.d.) “Riprap revetments”. ODRN division of soil and water resources. Retrieved August 2nd, 2015 from: http://www.dnr.state.oh.us/water/pubs/fs_st/stfs16/tabid/4171/Default.aspx
- Partridge, B., Fox, P., Alleman, J., Mast, D. (1999). *Field Demonstration of Highway Embankment Using Waste Foundry Sand*. Transportation Research Record 1670. Paper No. 99-0612
- Rathje, E., Rauch, A., Trejo, D., Folliard, K., Viyanant, C., Esfellar, M., Jain, A., Ogalla, M. (2006). *Evaluation of Crushed Concrete and Recycled Asphalt Pavement as Backfill for Mechanically Stabilized Earth Walls*. CTR Technical Report 0-4177-3.
- Rollin, A. L., Broughton, R. S., and Bolduc, G., (1985). “Synthetic Envelopment Materials for Subsurface Drainage Tubes”, paper presented at CPTA annual meeting, 1985, Fort Lauderdale, FL.
- RMRC (Recycled Material Resource Center). (2008). User guideline for byproducts and secondary use materials in pavement construction: Coal bottom ash/ boiler slag. Retrieved Aug 31st, 2015 from: <http://rmrc.wisc.edu/ug-mat-coal-bottom-ashboiler-slag/>
- RMRC (Recycled Material Resource Center). (2015). Retrieved October 1st, 2015, from <http://rmrc.wisc.edu/ug-mat-reclaimed-concrete-material/>
- Sarsby, R. (1985). “*The Influence of Aperture Size/Particle Size in the Efficiency of Grid Reinforcement*”. Proceedings of the 2nd Canadian Symposium on Geotextiles and Geomembranes. Geotechnical Society of Edmonton, pp 7-12. Edmonton, Canada.
- Seals, K., Moulton, K., Ruth, E. (1972). Bottom Ash: An Engineering Material. *Journal of Soil Mechanics*. Foundations. Div., Volume: 8, Issue: 4, Pages: 311-325, TN:2621229.
- Sengoz, B., Topal, A. (2004). *Use of Asphalt Roof Shingle in HMA*. Construction and Building Material 19, 337-346. doi:10.1016/j.conbuildmat.2004.08.005

- Soleimanbeigi, A. Edil, T., Benson, C. (2011). “*Recycled Asphalt Shingles with Granular Byproducts as Structural Fills*”. Student Project Report, University of Wisconsin System Solid Waste Research Program.
- Soleimanbeigi, A.(2012). *Geotechnical Evaluation of Recycled Asphalt Shingles as Structural Fill*. (Doctoral Dissertation). University of Wisconsin-Madison.
- Soleimanbeigi, A., Edil, T. (2015). Compressibility of Recycled Materials for Use As Highway Embankment Fill. *ASCE*, 1–14. doi:10.1061/(ASCE)GT.1943-5606.0001285.
- Stuedlein, A. W., Bailey, M., Lindquist, D., Sankey, J., & Neely, W. J. (2010). Design and Performance of a 46-m-High MSE Wall. *Journal of Geotechnical and Geoenvironmental Engineering*, 136(June), 786–796. doi:10.1061/(ASCE)GT.1943-5606.0000294
- Tatlisoz, N., Edil, T. B., & Benson, C. H. (1998). Interaction between Reinforcing Geosynthetics and Soil-Tire Chip Mixtures. *Journal of Geotechnical and Geoenvironmental Engineering*, 124(November), 1109–1119. doi:10.1061/(ASCE)1090-0241(1998)124:11(1109)
- Tatsuoka, F., Aquil, U., & Uchimura, T. (2005). GSP 138 Site Characterization and Modeling. *GeoFrontiers 2005 Site Characterization and Modeling*, pp. 1–10.
- Thomas, Michael. (2007). “*Optimizing the Use of Fly Ash*”. Portland Cement Association, Volume 5420. Skokie. IL.
- Thrace-LINQ (2012). Product Data Sheet, Geotextile GTF-570. Retrieved September 22nd, 2015 from: http://www.thracelinq.com/datasheets/Thrace-LINQ_DataSheet-GTF570.pdf
- Townsend, T., Powell, J., and Xu, C. (2007). “*Environmental issues associated with asphalt shingle recycling*”. Construction Materials Recycling Association, US EPA Innovations Workgroup.
- WisDOT (Wisconsin Department of Transportation). (2015). Wisconsin Department of Transportation, Bridge Manual, Chapter 14 – Retaining Walls.
- Warner, J., Edil, T. (2010). *Evaluation of Recycled Asphalt Shingles for Beneficial Reuse in Road Construction*. RMRC, University of Wisconsin-Madison.
- WBCSD (World Business Council for Sustainable Development). (n.d.). Retrieved January 16th, 2015, from <http://www.wbcscement.org/pdf/CSI-RecyclingConcrete-FullReport.pdf>
- Xie, Y., & Leshchinsky, B. (2015). Geotextiles and Geomembranes MSE walls as bridge abutments : Optimal reinforcement density. *Geotextiles and Geomembranes*, 43(2), 128–138. doi:10.1016/j.geotexmem.2015.01.002

Yohchia, C. (1997). Practical Analysis and Design of Mechanically-Stabilized Earth Walls – I. Design Philosophies and Procedures. *Engineering Structures* 22(2000) 793-808. Elsevier Sciences ltda.

Yoon, S., Balunaini, U., Yildirim, I., Prezzi, M., Siddiki, N. (2009). “*Construction of an Embankment with Fly and Bottom Ash Mixture: Field Performance Study*”. *Journal of Materials in Civil Engineering*. ASCE. June 2009. doi:10.1061/_ASCE_0899-1561_2009_21:6_271_